Doctor thesis

Study on formation and optoelectronic property of $Ge_{1-x}Sn_x$ based group-IV semiconductor heterostructures

$Ge_{1-x}Sn_x$ 系 IV 族半導体ヘテロ構造の形成と光電子物性に関する研究

Shiyu Zhang

張 師宇

2023

Department of Materials Physics,

Graduate School of Engineering, Nagoya University

Contents

Chapter 1 Introduction

1.1 Background of this study

1.1.1 Requirement of ULSI system for future information society

The daily function of our modern society needs the support of the billion's microelectronic devices. As the fundamental building block of the microelectronics, semiconductor devices have been studied and developed in many years and is now being used in a variety of application fields.[1)] For example, the well-used smart mobile systems such as smart phones, tablets and laptops, the medical care wearable- and implantable devices, and environment monitoring devices. **Figure 1.1** shows the number of smartphones sold to end users worldwide from 2007 to 2021. About 1.5 billion units sold in the year 2021 compared to the 122 million units in 2007[2)] (year of smartphone first introduction), showing a strong increase of portable device market in the decades and

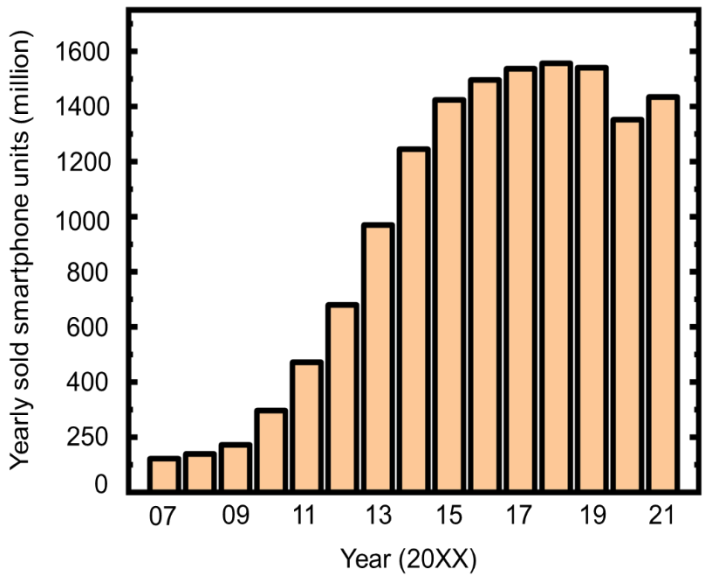

Figure 1.1 Number of smartphones sold to end users worldwide from 2007 to 2021.[2)]

subsequent big potential in the future. Additionally, the internet of things (IoT) technology, in which the concept of smart portable devices are expanded into more variety such as mobile cars and house appliances are also progressing in a fast pace. Eventually, all these advanced techniques require better performance micro electrical components to support their function, this leads to the demand of faster-processing speed and lower-power-consumption ultra-large-scale-integration (ULSI) components.[3)]

The need for the high performance and low-cost ULSI has always been a challenge for the semiconductor industry in the past decades. Generally, higher transistor integration density leads to higher performance and cost-efficiency chip products. Therefore, main objective of the industry is to increase the integration density of transistors on chips. In the past years, using scaling technology to shrink the size of an individual transistor has been proved effective.[4)] **Figure 1.2** shows the data of the transistor density and the corresponded feature size of the major product from the year of 1981 to 2020.[5)] It can be seen that by reducing the feature size from 3 μm to the latest 7 nm, the transistor density

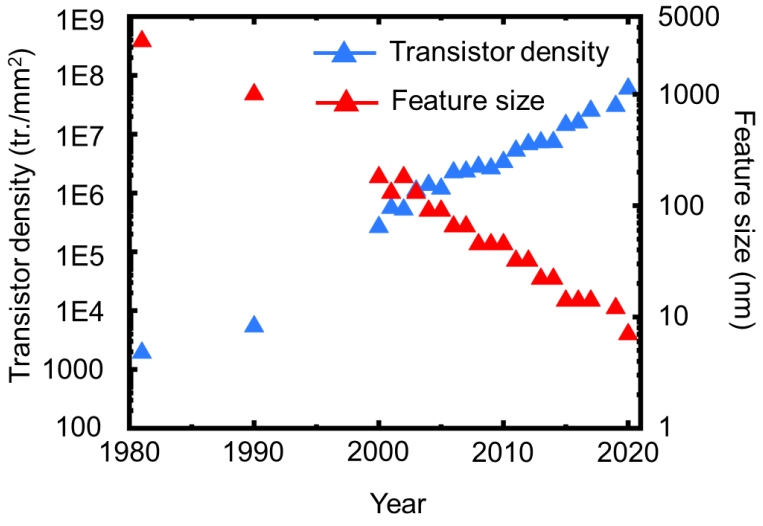

Figure 1.2 Transistor density and the corresponding feature size of the major product from 1981 to 2020.[5)]

has been increased dramatically to the 59 million r./mm^2. The increasing of the transistor density has provided us more advanced electronic devices with higher performance and better energy efficiency such as next-generation tablets and smart wearable devices, and they also helped to shape the lifestyle of the modern people with more possibilities.

1.1.2 Introducing of optical interconnect on Si platform ULSI

Initially, in scaling law, with a scaling factor of k, when the size of a transistor shrinks $1/k$, the operation current and voltage together with the electrical capacity of the transistor becomes $1/k$. Therefore, the consumption power during transition operation turns into $1/k^2$, and the circuit delay will also be $1/k$. This explains why scaling process is essential to the high performance and cost-efficiency ULSI chips. However, as the feature size of transistors scaled into deep nanometer field, new challenges such as the physical limitation of process, short-channel[6)] and tunnel effect[7)] appears.

Among them, the limitation of metal interconnect is critical. As metal interconnect is the key component used for signal propagation and power conducting, the shrink of metal interconnect will increase its electrical resistance, leads to higher power consumption as well as the RC delay.[8,9)] It has been reported that the metal interconnect has influenced the communication speed of the global ULSI system since the feature size entered the 250 nm field.[10)] Additionally, the wafer size has the trend of increasing in the recent year,[11)] which means the use of long-distance interconnect is predictable, and the power consumption of metal interconnect will be more severe. All in all, the limitation of metal interconnect will be a major problem in the future progress of ULSI technology, and the solution to solve this issue is an important task.

As a potential solution to this problem, optical interconnect has been proposed and

has attracted lots of attention in the recent years.[12–15] In this concept, communication signals are no longer conducted by electrical current through metal wire but are transported in the form of the light wave. Therefore, the issue of power dissipation and scaling down of transistor size are expected to be solved, and even better performance including larger communication data amount and faster signal processing speed are possible due to the nature of optical communication mechanism. Here, **Figure 1.3** shows the concept graph of the optical interconnect on Si platform in the ULSI system. To ensure the function of the optical interconnect, several components such as modulator, light source, waveguide, and detector are required to integrate on the Si platform.

Therefore, high affinity with Si is the first priority for these components, and the all-group-IV material optical interconnect structure is promising to the requirement. Recently, related research on the group-IV material optical interconnect structure has been carried out by many groups. There're reports on the waveguide based on Si,[16] Ge[17] and SiO_2[18] materials. And the detector based on Si and Ge has also been reported.[19–21] In addition, by introducing Sn into Ge matrix to form $Ge_{1-x}Sn_x$ alloy-based detector, the better sensitivity has been achieved comparing to that based on Ge, and by increasing the content of Sn to 9%, the detection range of light wave of $Ge_{1-x}Sn_x$ detector can be

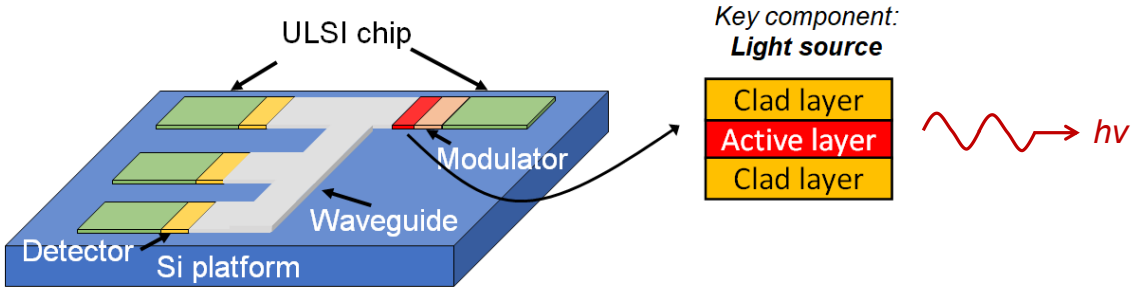

Figure 1.3 The concept of optical interconnect integrated on Si platform and the cross-section structure of the semiconductor laser light source.

expanded to around 2.5 um.[22] Among the components of the optical interconnect concept, the most important key part is the light source, in which the desired light is emitted from the active layer sandwiched by the clad layers, as shown in the right side of **Figure 1.3**. In the next section, the details of the group-IV material light source with be introduced.

1.1.3 The development of group-IV material light source for Si platform integration optical interconnect

Nowadays, the research on the major components of optical interconnect structure such as the detector and waveguide has already granted many progressions except for the light source. This is because that the Si platform integration optical interconnect has two restricted key requirements for the material. First, the high light emission efficiency and second, the high Si affinity. Initially, the group-III−V compound semiconductors such as GaN/AlN, InGaN/AlN, GaInNAs/GaAs and InAs/GaAs,[23–25] were considered for because of their direct transition bandgap nature is beneficial for the enhancement of the light emission efficiency. However, the direct formation of group-III−V semiconductor on Si substrate has many affinity problems, for example, the generation of high threading dislocation density and the contamination as dopant in Si wafer. Although some groups have focused on the wafer bonding techniques to avoid these issues and has already demonstrated the excellent performance of III−V compound lasers on Si.[26,27] The bonding technique consists of a series complex process and is likely to result in the increased manufacture costs.

From the perspective of integration on Si substrate, the group-IV semiconductor is promising because of their high affinity with Si. However, the well-used group-IV semiconductor like Si and Ge have the disadvantage of the indirect transition bandgap.

Here, **Figure 1.4** shows the energy band structure of (a) Si and (b) Ge.[28] It can be seen that the highest valence band energy position of both Si and Ge are located at the Γ point, while the lowest energy position at conduction band for Si and Ge are located at the X and L points, respectively. As a result of the unmatched maximum and minimum energy position at valence band and conduction band, both Si and Ge have the low radiative recombination efficiency.

Some research groups have reported that the strained Ge could realize the direct bandgap structure by strain engineering.[29,30] This technique introduces biaxial tensile strain onto the Ge to shift the energy position of conduction band at the Γ point ($E_{C,\Gamma}$) to the lower position than that of the L point ($E_{C,L}$), so the direct transition structure can be made. However, to do so, a very large tensile strain at 1.7% is inevitable,[29] and the introducing of such large strain will generate dislocations among the crystal structure of Ge matrix, leading to a poor crystallinity that is negative for the radiative recombination process.

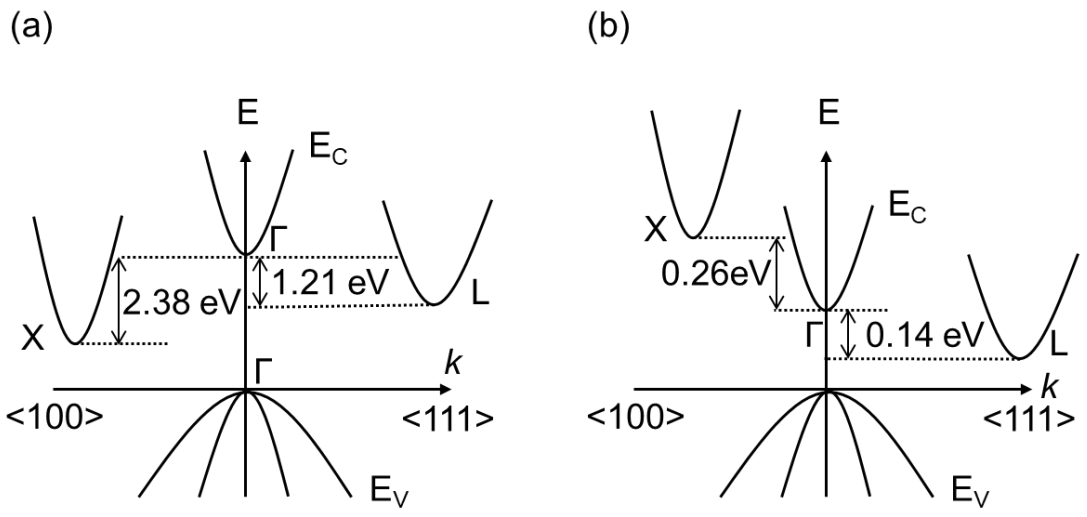

Figure 1.4 The energy band structure of (a) Si and (b) Ge.

Recently, the Si-compatible group-IV $Ge_{1-x}Sn_x$ semiconductor alloy has received many interests as a promising candidate for realizing direct bandgap transition light source. The typical $Ge_{1-x}Sn_x$ binary structure is formed by incorporating Sn into Ge matrix. As shown in **Figure 1.4,** Ge has an indirect transition nature where its direct bandgap $E_{g\Gamma}$ at Γ point is about 0.14 eV larger than its indirect bandgap E_{gL} at L point, increasing the Sn content will reduce the energy difference between the Γ- and L- points. The indirect-direct crossover takes places when the Sn content reaches 7% in strain-free condition. In practical pseudomorphic growth condition, strain deformation impacts the energy band structure and epitaxial grown $Ge_{1-x}Sn_x$ needs 17% Sn content to reach the indirect-direct crossover point.[31),32)] **Figure 1.5** shows the process of aforementioned direct transition of $Ge_{1-x}Sn_x$, and summary of advantage and disadvantage of different material candidates for the optical interconnect light source are listed in **Table 1.1**.

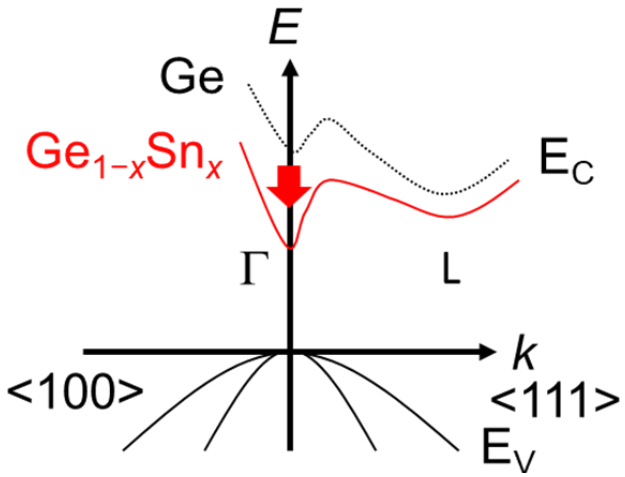

Figure 1.5 The direct transition of $Ge_{1-x}Sn_x$ by increasing Sn content.

Table 1.1 Energy band transition type and Si substrate affinity of candidate materials for the light source component.

Light emission material	Group-III−V semiconductor	Elemental Group-IV semiconductor (Si, Ge)	Group-IV alloy (GeSn)
Direct bandgap (High emission efficiency)	○	×	▲
Si platform affinity	×	○	○

1.1.4 Towards room temperature operation $Ge_{1-x}Sn_x$ light emission structure

To discuss the appropriate structure design for light emission application, group-III−V semiconductors cases are good references as they are already well-studied and used in many fields. First, according to the previous report, room temperature lasing from group-III−V lasers have been realized by forming heterostructure.[33] And the lasing threshold condition such as injection current density can be reduced by forming appropriate heterostructure and quantum well design.[34] Therefore, the design of preferable heterostructure is key to the semiconductor lasers.

Back to group-IV semiconductor lasers, the first lasing of $Ge_{1-x}Sn_x$ grown on a virtual Ge substrate with Sn content at 12.6% optically pumped at 90 K was reported in 2015.[35] To improve the performance of $Ge_{1-x}Sn_x$ laser, mainly to increase the lasing temperature, several methods have been proposed by many research groups, defect management, strain relaxation engineering and microdisk cavity design have been proved effective.[36),37] By using the composition graded $Ge_{1-x}Sn_x$ layers and a ridge wave guide structure, the leasing temperature has been increased to 180 K.[37] Furthermore, the introducing of microdisk structure is also effective to improve emission efficiency, leading to the raising of the lasing temperature up to 270 K.[38] However, room temperature (RT) lasing report is still lacking. Although a report in 2022 has demonstrated the lasing of a $Ge_{1-x}Sn_x$ microdisk at 305 K, which is mainly contributed by high Sn incorporation at active layer and the optimized pedestal architecture in microdisk structure.[39] The overly high lasing threshold (3.27 MW/cm^2) is still an issue of the practical application. In addition, the aforementioned reports are mostly based on optically pumped lasers, and to meet the requirement of light source components in ULSI system, electrically pumped lasers are

needed. Therefore, the application of group-IV based lasers are still in a long distance.

Based on the reports of group-IV and III-V compound semiconductor lasers, effective carrier confinement structure is essential to improve the lasing temperature and reducing pumping threshold.[40–42] In order to realize a RT operation $Ge_{1-x}Sn_x$ light source, type-I energy band alignment with a sufficient energy band offset is the key. **Figure 1.6** shows the concept of the heterostructure that satisfy this requirement. Forming type-I energy band alignment requires the clad layer has larger bandgap than the active layer, and to ensure the carrier confinement at RT, both energy band offset at valence and conduction bands should at least larger than 26 meV, which is the kinetic energy of electron and holes at RT (= k_BT @RT).

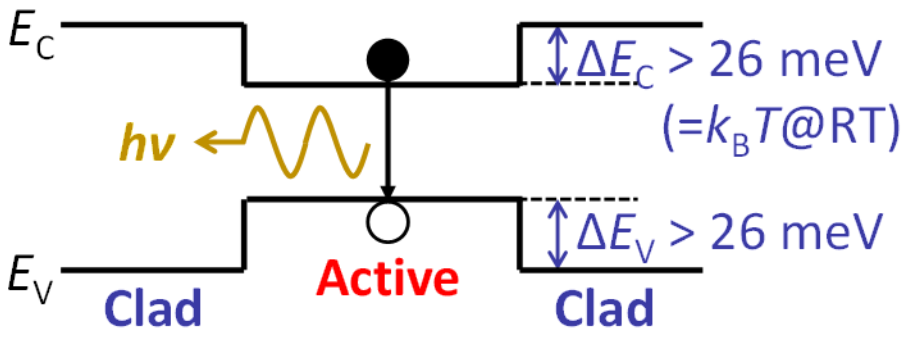

Figure 1.6 The concept of a carrier confinement heterostructure.

Recently, the band-offset-tunable $Ge_{1-x}Sn_x/Si_yGe_{1-x-y}Sn_x$ heterostructure has been considered a promising candidate to meet this requirement.[43–45] As $Si_yGe_{1-x-y}Sn_x$ has the ability to adjust energy band structure and lattice constant simultaneously by controlling its Si/Sn composition ratio, it is possible to achieve the large energy band offset at the lattice matched $Ge_{1-x}Sn_x/Si_yGe_{1-x-y}Sn_x$ interface. Here, **Table 1.2** shows the summary of $Ge_{1-x}Sn_x/Si_yGe_{1-x-y}Sn_x$ heterostructures reported by several research groups in terms of

their epitaxial method, elemental composition in $Ge_{1-x}Sn_x$ and $Si_yGe_{1-x-y}Sn_x$ layers , and energy offset values at valence band (ΔE_V) and conduction band (ΔE_C).[46–49] For some reports, multiple structures are discussed. It is notable that all energy band alignment in these reported structures are in the form of type-I heterostructure. It can be seen that the energy band offset at the conduction band ΔE_C and valence band ΔE_V are increased by increasing the Si content in $Si_yGe_{1-x-y}Sn_x$ layers, and therefore stronger carrier confinement can be established. Thus, high Si content in $Si_yGe_{1-x-y}Sn_x$ layer is important to improve the carrier confinement effect.

It is worth mention that currently most of the reports on $Ge_{1-x}Sn_x/Si_yGe_{1-x-y}Sn_x$ heterostructures are based on the chemical vapor deposition (CVD) epitaxial method. As CVD epitaxial method is the fundamental manufacture technology in the semiconductor industry, studying the property of CVD grown $Ge_{1-x}Sn_x/Si_yGe_{1-x-y}Sn_x$ heterostructure has an important practical significance. However, due to the low solid solubility of Sn in Ge (1%) and Si (0.1%),[50,51] and a strong tendency for surface segregation of Sn atoms in $Ge_{1-x}Sn_x$ and $Si_yGe_{1-x-y}Sn_x$ matrix. Growth of high Sn and Si composition crystalline quality $Ge_{1-x}Sn_x/Si_yGe_{1-x-y}Sn_x$ heterostructure requires low growth temperature to ensure

Table 1.2 Summary of epitaxial method, elemental contents, and energy band alignment information of multiple $Ge_{1-x}Sn_x/Si_yGe_{1-x-y}Sn_x$ heterostructures reported by different groups[46-49].

Reference	Epitaxy method	Structure type	GeSn Sn content (%)	SiGeSn Si/Sn contents (%)	$\Delta E_{C,L}$ (meV)	$\Delta E_{C,\Gamma}$ (meV)	ΔE_V (meV)
A	CVD	DHS	14.5	4.5/14.0 (top) 5.5/11.5(bottom)	119 (top) 99 (bottom)	191 (top) 98 (bottom)	-
	CVD	MQW	13.3	4.8/13.0	45	79	-
	CVD	MQW	13.3	5.2/13.4	22	71	-
B	CVD	MQW	8.6	10.5/10.9	35	183	49
C	MBE	MQW	7.3	10.0/5.0	105	193	103
	MBE	MQW	8.5	10.0/5.0	112	205	120
D	MBE	DHS	9.0	23.0/11.0	78	424	146

the non-equilibrium condition.[31] On the other hand, due to the limitation of CVD technology, in which the crystal quality, composition and growth rate is heavily depended by growth temperature. It is difficult to lower the growth temperature of $Ge_{1-x}Sn_x$ and $Si_yGe_{1-x-y}Sn_x$ layers while maintaining high Si composition. For most CVD cases, the growth temperature of the $Ge_{1-x}Sn_x/Si_yGe_{1-x-y}Sn_x$ heterostructures are around 350 °C,[46,47] in which the epitaxially grown $Si_yGe_{1-x-y}Sn_x$ layers have the Si content around ~10%.

Meanwhile, another method, the molecular beam epitaxy (MBE) technique is also a well-used tool for the epitaxial growth of $Ge_{1-x}Sn_x$ and $Si_yGe_{1-x-y}Sn_x$ materials.[31,48,49,52] Unlike the CVD technique, MBE method is the non-equilibrium epitaxial growth method which can support lower growth temperature for the $Ge_{1-x}Sn_x/Si_yGe_{1-x-y}Sn_x$ heterostructures. The low growth temperature condition is not only beneficial for the high Si content formation of $Si_yGe_{1-x-y}Sn_x$ layer but is also helpful to suppress the segregation of Sn atoms in the $Ge_{1-x}Sn_x/Si_yGe_{1-x-y}Sn_x$ structure, leading to the better crystallinity that can increase the emission efficiency. The reference D in **Table 1.2**, is from a report of Nakatsuka group on the MBE grown $Ge_{1-x}Sn_x/Si_yGe_{1-x-y}Sn_x$ heterostructures,[49] in which the growth temperatures of $Ge_{1-x}Sn_x$ and $Si_yGe_{1-x-y}Sn_x$ layers were 150 and 200 °C, respectively. As a result, Si content in the $Si_yGe_{1-x-y}Sn_x$ layers has been improved to 23%, and up to 424 meV energy band offset at conduction band ($\Delta E_{C,\Gamma}$) has also been achieved. Leading to a 12 times enhancement of PL efficiency comparing to the $Ge_{1-x}Sn_x$/Ge heterostructure.

From the aforementioned background, MBE technique has a great potential on realizing higher Si content $Ge_{1-x}Sn_x/Si_yGe_{1-x-y}Sn_x$ heterostructure and increasing the larger energy band offset to ensure strong carrier confine effect for the $Ge_{1-x}Sn_x$ layer. However, reports on the MBE grown $Ge_{1-x}Sn_x/Si_yGe_{1-x-y}Sn_x$ heterostructures especially the MQW

formation related cases are still lacking. On the other hand, the $Ge_{1-x}Sn_x/Si_yGe_{1-x-y}Sn_x$ MQW structure's property and mechanism has been widely discussed upon the CVD cases, and most reports agree that MQW formation has better performance on the light emission efficiency compared to the normal heterostructures. Therefore, in order to achieve optoelectronic application based on group-IV semiconductor materials, it is also important to discover the possibility and property of MBE grown high Si content $Ge_{1-x}Sn_x/Si_yGe_{1-x-y}Sn_x$ MQW formation.

1.2 Purpose of this study

Currently, the biggest challenge of optoelectronics application of $Ge_{1-x}Sn_x$ is the insufficient of its light emission efficiency at RT. As we discussed in the previous section, appropriate heterostructure with large energy band offsets to establish sufficient carrier confinement effect is essential to improve emission efficiency of $Ge_{1-x}Sn_x$ at RT. Therefore, the main objective of this study is to develop the reliable technique that can provide the high light emission efficiency heterostructure formation and characterize their physical properties to expand the understanding of the mechanism of the emission property of the $Ge_{1-x}Sn_x/Si_yGe_{1-x-y}Sn_x$ heterostructures.

To establish the sufficient carrier confinement for the $Ge_{1-x}Sn_x/Si_yGe_{1-x-y}Sn_x$ structure, high Si content in $Si_yGe_{1-x-y}Sn_x$ layers are needed to increase the energy band offset. In this study, the MBE method has been used to achieve the epitaxial growth of high crystallinity $Ge_{1-x}Sn_x/Si_yGe_{1-x-y}Sn_x$ multi quantum well (MQW) structure with a high Si content in the $Si_yGe_{1-x-y}Sn_x$ layer. Low growth temperature condition will be challenged to suppress the Sn segregation and to ensure high crystal quality. The rather simple formation of $Ge_{1-x}Sn_x/Si_yGe_{1-x-y}Sn_x$ single quantum well will be firstly examined upon the

impact of growth temperature in terms of the crystallinity and photoluminescence (PL) performance. Then, the $Ge_{1-x}Sn_x/Si_yGe_{1-x-y}Sn_x$ double quantum well formation will be subsequently investigated and discussed.

The direct energy band transition process of $Ge_{1-x}Sn_x$ will be next discussed. The heavy Sb n-type doping method will be used to increase the electron population in the conduction band. Pseudo-direct energy bandgap transition n^+-$Ge_{1-x}Sn_x$ has been achieved by increasing doping concentration up to 10^{20} cm^{-3}. Appropriate heterostructure formation to improve the PL performance of the n^+-$Ge_{1-x}Sn_x$ will be discussed. Detailed investigation on their PL mechanism and the impact of the energy band alignment will be also carried out.

1.3 Outline of this study

In chapter 2, the epitaxial growth and the property characterization method of the samples will be described. In chapter 3, the formation of low growth temperature $Ge_{1-x}Sn_x/Si_yGe_{1-x-y}Sn_x$ single- and double quantum wells will be demonstrated. Details such as their crystallinity, PL performance, energy band alignment as well as the impact of post annealing process will be discussed. In chapter 4, the pseudo-direct energy bandgap transition technique for the n^+-$Ge_{1-x}Sn_x$ will be described. And finally, the chapter 5 will give a summary of this study together with the future guidelines for the group-IV semiconductor optoelectronics.

Part of this research report is based on the journal papers and conference presentations by the author himself during his doctoral program.[53,54)]

References

1) C. Jacoboni and P. Lugli, in *The Monte Carlo Method for Semiconductor Device Simulation*, eds. C. Jacoboni and P. Lugli (Springer, Vienna, 1989) p. 162.
2) International Roadmap for Devices and Systems (IRDS^{TM}) 2022 Edition - IEEE IRDS^{TM}, https://irds.ieee.org/editions/2022, (accessed 17 December 2022).
3) K. Shibayama, in *International Symposium on VLSI Technology, Systems and Applications,* (1989) p. 7.
4) R. H. Dennard, F. H. Gaensslen, H.-N. Yu, V. L. Rideout, E. Bassous and A. R. LeBlanc, IEEE Journal of Solid-State Circuits **9** (5), 256 (1974).
5) "Transistor count", *Wikipedia*, last updated December 17th, 2022. https://en.wikipedia.org/wiki/Transistor_count
6) Q. Xie, J. Xu and Y. Taur, IEEE Transactions on Electron Devices **59** (6), 1569 (2012).
7) J. Wang, M. Lundstrom, in *International Electron Devices Meeting (IEDM)* (2002) p. 707.
8) 公麿吉川, 応用物理 **68** (11), 1215 (1999).
9) Igor L. Markov, Nature **512**, 145 (2014).
10) 谷口　研二, 鳥海　明, 財満　鎭明, 大場　隆之, 河﨑　尚夫, プロセスインテグレーション, 丸善出版 (2010).
11) M. Marks, Z. Hassan and K. Y. Cheong, Critical Reviews in Solid State and Materials Sciences **40** (50), 1 (2015).
12) D. Thomson, A. Zilkie, J. E. Bowers, T. Komljenovic, G. T. Reed, L. Vivien, D. Marris-Morini, E. Cassan, L. Virot, J.-M. Fédéli, J.-M. Hartmann, J. H. Schmid, D.-X. Xu, F. Boeuf, P. O'Brien, G. Z. Mashanovich and M. Nedeljkovic, J. Opt. **18** (7),

073003 (2016).

13) Y. Arakawa, T. Nakamura, Y. Urino and T. Fujita, IEEE Communications Magazine **51** (3), 72 (2013).

14) R. Soref, D. Buca and S.-Q. Yu, Optics & Photonics News, OPN **27** (1), 32 (2016).

15) M. Haurylau, G. Chen, H. Chen, J. Zhang, N. A. Nelson, D. H. Albonesi, E. G. Friedman and P. M. Fauchet, IEEE Journal of Selected Topics in Quantum Electronics **12** (6), 1699 (2006).

16) Y. Zhou, S. Chakravarty, Chi-jui. Chung, X. Xu, and R. T. Chen, Photon. Res. **6** (4), 254 (2018).

17) K. Oda, T. Okumura, J. Kasai, S. Kako, S. Iwamoto and Y. Arakawa, Jpn. J. Appl. Phys. **55** (4S), 04EH06 (2016).

18) A. Politi, M. J. Cryan, J. G. Rarity, S. Yu and J. L. O'Brien, Science **320** (5876), 646 (2008).

19) L. Liao, D. Samara-Rubio, M. Morse, A. Liu, D. Hodge, D. Rubin, U. D. Keil and T. Franck, Opt. Express, OE **13** (8), 3129 (2005).

20) H. C. Nguyen, S. Hashimoto, M. Shinkawa and T. Baba, Opt. Express, OE **20** (20), 22465 (2012).

21) J. Miche, J. Liu, L. C. Kimerling, Nature photonics, **4**, 527 (2010).

22) H. Tran, C. G. Littlejohns, D. J. Thomson, T. Pham, A. Ghetmiri, A. Mosleh, J. Margetis, J. Tolle, G. Z. Mashanovich, W. Du, B. Li, M. Mortazavi and S.-Q. Yu, Front. Mater, **6** (278), (2019).

23) J. Sellés, V. Crepel, I. Roland, M. El Kurdi, X. Checoury, P. Boucaud, M. Mexis, M. Leroux, B. Damilano, S. Rennesson, F. Semond, B. Gayral, C. Brimont and T. Guillet,

Appl. Phys. Lett. **109** (23), 231101 (2016).

24) H. Liu, T. Wang, Q. Jiang, R. Hogg, F. Tutu, F. Pozzi and A. Seeds, Nature Photonics, **5**, 416 (2011).

25) K. Ohira, K. Kobayashi, N. Iizuka, H. Yoshida, M. Ezaki, H. Uemura, A. Kojima, K. Nakamura, H. Furuyama and H. Shibata, Opt. Express, OE **18** (15), 15440 (2010).

26) S.-W. Seo, S.-Y. Cho and N. M. Jokerst, Opt. Lett., OL **32** (5), 548 (2007).

27) S.-Y. Cho, S. Palit, D. Xu, G. Tsvid, N. Jokerst, L. Mawst and T. Kuech, in *LEOS 2007 - IEEE Lasers and Electro-Optics Society Annual Meeting Conference Proceedings* (IEEE, Lake Buena Vista, FL, USA, 2007) p. 829.

28) O. Madelung Semiconductors Data Handbook, Springer, (2004).

29) R. Chen, H. Lin, Y. Huo, C. Hitzman, T. I. Kamins and J. S. Harris, Appl. Phys. Lett. **99** (18), 181125 (2011).

30) D. S. Sukhdeo, D. Nam, J.-H. Kang, M. L. Brongersma and K. C. Saraswat, Photon. Res., PRJ **2** (3), A8 (2014).

31) S. Zaima, O. Nakatsuka, N. Taoka, M. Kurosawa, W. Takeuchi and M. Sakashita, Science and Technology of Advanced Materials **16** (4), 043502 (2015).

32) J. Mathews, R. T. Beeler, J. Tolle, C. Xu, R. Roucka, J. Kouvetakis and J. Menéndez, Appl. Phys. Lett. **97** (22), 221912 (2010).

33) I. Hayashi, M. B. Panish, P. W. Foy and S. Sumski, Appl. Phys. Lett. **17** (3), 109 (1970).

34) Z. Alferov, IEEE Journal of Selected Topics in Quantum Electronics **6** (6), 832 (2000).

35) S. Wirths, R. Geiger, N. von den Driesch, G. Mussler, T. Stoica, S. Mantl, Z. Ikonic, M. Luysberg, S. Chiussi, J. M. Hartmann, H. Sigg, J. Faist, D. Buca and D. Grützmacher, Nature Photon **9** (2), 88 (2015).

36) A. Elbaz, D. Buca, N. von den Driesch, K. Pantzas, G. Patriarche, N. Zerounian, E. Herth, X. Checoury, S. Sauvage, I. Sagnes, A. Foti, R. Ossikovski, J.-M. Hartmann, F. Boeuf, Z. Ikonic, P. Boucaud, D. Grützmacher and M. El Kurdi, Nat. Photonics **14** (6), 375 (2020).

37) V. Reboud, A. Gassenq, N. Pauc, J. Aubin, L. Milord, Q. M. Thai, M. Bertrand, K. Guilloy, D. Rouchon, J. Rothman, T. Zabel, F. Armand Pilon, H. Sigg, A. Chelnokov, J. M. Hartmann and V. Calvo, Appl. Phys. Lett. **111** (9), 092101 (2017).

38) Y. Zhou, W. Dou, W. Du, S. Ojo, H. Tran, S. A. Ghetmiri, J. Liu, G. Sun, R. Soref, J. Margetis, J. Tolle, B. Li, Z. Chen, M. Mortazavi and S.-Q. Yu, ACS Photonics **6** (6), 1434 (2019).

39) J. Chrétien, Q. M. Thai, M. Frauenrath, L. Casiez, A. Chelnokov, V. Reboud, J. M. Hartmann, M. El Kurdi, N. Pauc and V. Calvo, Appl. Phys. Lett. **120** (5), 051107 (2022).

40) S. Mokkapati and C. Jagadish, Materials Today **12** (4), 22 (2009).

41) K. Kishino, A. Kikuchi, Y. Kaneko and I. Nomura, Appl. Phys. Lett. **58** (17), 1822 (1991).

42) Y. Miao, G. Wang, Z. Kong, B. Xu, X. Zhao, X. Luo, H. Lin, Y. Dong, B. Lu, L. Dong, J. Zhou, J. Liu and H. H. Radamson, Nanomaterials **11** (10), 2556 (2021).

43) R. Ranjan and M. K. Das, Opt Quant Electron **48** (3), 201 (2016).

44) G. Sun, R. A. Soref and H. H. Cheng, Opt. Express, OE **18** (19), 19957 (2010).

45) G. Chang, S. Chang and S. L. Chuang, IEEE Journal of Quantum Electronics **46** (12), 1813 (2010).

46) D. Stange, N. von den Driesch, T. Zabel, F. Armand-Pilon, D. Rainko, B. Marzban, P. Zaumseil, J.-M. Hartmann, Z. Ikonic, G. Capellini, S. Mantl, H. Sigg, J. Witzens, D.

Grützmacher and D. Buca, ACS Photonics **5** (11), 4628 (2018).

47) D. Stange, N. von den Driesch, D. Rainko, S. Roesgaard, I. Povstugar, J.-M. Hartmann, T. Stoica, Z. Ikonic, S. Mantl, D. Grützmacher and D. Buca, Optica, OPTICA **4** (2), 185 (2017).

48) L. Peng, X. Li, J. Zheng, X. Liu, M. Li, Z. Liu, C. Xue, Y. Zuo and B. Cheng, Journal of Luminescence **228**, 117539 (2020).

49) M. Fukuda, D. Rainko, M. Sakashita, M. Kurosawa, D. Buca, O. Nakatsuka and S. Zaima, Semicond. Sci. Technol. **33** (12), 124018 (2018).

50) X. Ma, T. Yoshikawa and K. Morita, Science of Advanced Materials **6** (8), 1697 (2014).

51) R. W. Olesinski and G. J. Abbaschian, Bulletin of Alloy Phase Diagrams **5** (3), 265 (1984).

52) M. Fukuda, D. Rainko, M. Sakashita, M. Kurosawa, D. Buca, O. Nakatsuka and S. Zaima, Jpn. J. Appl. Phys. **58** (SI), SIIB23 (2019).

53) S. Zhang, M. Fukuda, J. Jeon, M. Sakashita, S. Shibayama and O. Nakatsuka, Jpn. J. Appl. Phys. **61** (SA), SA1004 (2021).

54) S. Zhang, S. Shibayama and O. Nakatsuka, Semicond. Sci. Technol. **38** (1), 015018 (2022).

Chapter 2 Sample preparation and characterization method

2.1 Sample preparation

2.1.1 Substrate surface cleaning recipe

All samples shown in this paper are mainly epitaxial grown on the Ga doped p-Ge (001) wafer (substrate). The substrate cleaning process contains chemical cleaning and thermal treatment two parts. Detailed recipe of the cleaning process are listed in **Figure 2.1**. The substrate was firstly rinsed in the deionized water (DIW) for 10 minutes, then dipped into the 20% ammonia solution (NH_4OH : H_2O = 1 : 4) for 5 minutes at RT to remove the contamination particles and heavy metal contaminations, followed by a 10-minute rinse in DIW to wash away the residual chemicals. The dip in ammonia solution will inevitably generate oxide layer on the wafer surface, to etch the oxide layer, the wafer was next dipped in dilute sulfuric acid solution (H_2SO_4 : H_2O = 1 : 7) for 2 minutes to remove oxide layer as well as any metal and/or carbon contaminations.

After chemical cleaning, the substrate was then immediately loaded into the MBE load-lock chamber to prepare for transferring to the deposition chamber. Until the vacuum pressure of the load-lock chamber has reached the ~10^{-7} Torr (~ 1.3 × 10^{-5} Pa) level the substrate was then transferred into the deposition chamber in which the vacuum pressure has always been maintained around ~10^{-9} Torr (~ 1.3 × 10^{-7} Pa) to ensure the purity of the deposition process.

Before the epitaxial growth process, the substrate was thermally cleaned by degassing at 430 °C for 30 minutes, to remove the oxide layer that might be formed during the

sample transfer process and to form the stable (2 × 1) surface reconstruction condition for subsequent epitaxial layers grown on the substrate.

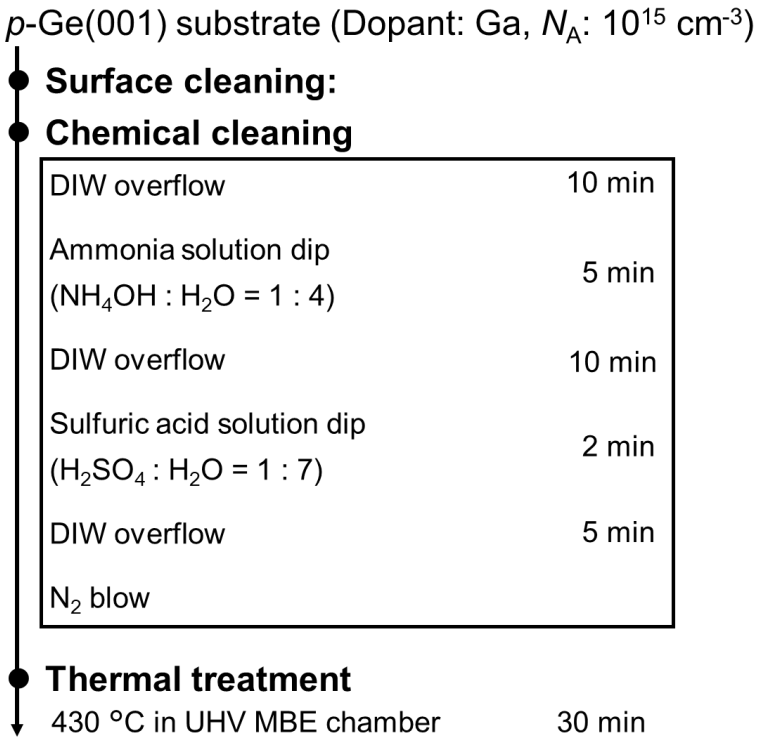

Figure 2.1 *p*-Ge (001) substrate cleaning process recipe.

2.1.2 Molecular beam epitaxy (MBE) growth for sample preparation

In this study, the $Ge_{1-x}Sn_x/Si_yGe_{1-x-y}Sn_x$ heterostructures and the pseudo-direct transition n^+-$Ge_{1-x}Sn_x$ were grown by the MBE system (ULVAC UHV-CH-3N). The MBE technique is a method of physical vapor deposition on a substrate by heating the elemental sources to evaporate molecular beam and incident on the substrate surface to perform epitaxial growth. The schematic concept of the MBE system used in this study is shown in **Figure 2.2**.

The epitaxial growth of MBE demands ultra-high vacuum environment, so multiple vacuum pumps including dry pump, turbo molecular pump and cryopump have been used

to maintain vacuum pressure of deposition chamber under ~10^{-9} Torr (~ 1.3 × 10^{-7} Pa) during the growth. The load-lock chamber, as the "preparation room" before transferring substrate into deposition chamber, is also vacuumized by an oil rotary pump and a turbo molecular pump.

An infrared radiant heater is located above the substrate location. With the use of a liquid nitrogen shroud, the thermal treatment of substrate can be carried out simultaneously while keeping high vacuum environment in deposition chamber.

The evaporation of Ge and Sn elements were carried out by the Knudsen-cell (K-cell) unit. They are made by high purity boron nitride and are connected to the bottom side of the MBE deposition chamber. The pure Ge and Sn substances were loaded in the individual K-cell units and were heated to around 900 ~ 1200 °C to be sublimated and deposited on the substrate surface to form epitaxial $Ge_{1-x}Sn_x$ thin films. As for the epitaxial growth of $Si_yGe_{1-x-y}Sn_x$ films, since they require the deposition of Si element, an electron gun (E-gun) has been used to evaporate Si element, the deposition rate of Si element was controlled by the emission current and the incident angle of electron beam on Si source. Deposition rate of Ge and Si were monitored by a crystal oscillation type deposition sensor (ULVAC, CRTM-6000). Additionally, it is worth mention that the pseudo-direct transition n^+-$Ge_{1-x}Sn_x$ in this study is in-situ doped by Sb during the epitaxial growth of $Ge_{1-x}Sn_x$. The deposition of Sb was performed using a K-cell,[1)] just as the same as Ge and Sn.

A RHEED equipment is installed inside the MBE deposition chamber, allowing the observation of the substrate surface condition as well as the crystal structure of grown epitaxial layers during the deposition process.

The advantages of the MBE system including the ability to control the uniform

thickness of each layer at the atomic level during the growth of heterostructure formation, as well as the ability to form steep hetero-interfaces through the control of different types of shutters (substrate, K-cell and E-gun). These advantages are important in the formation of heterostructures for light emitting device applications.

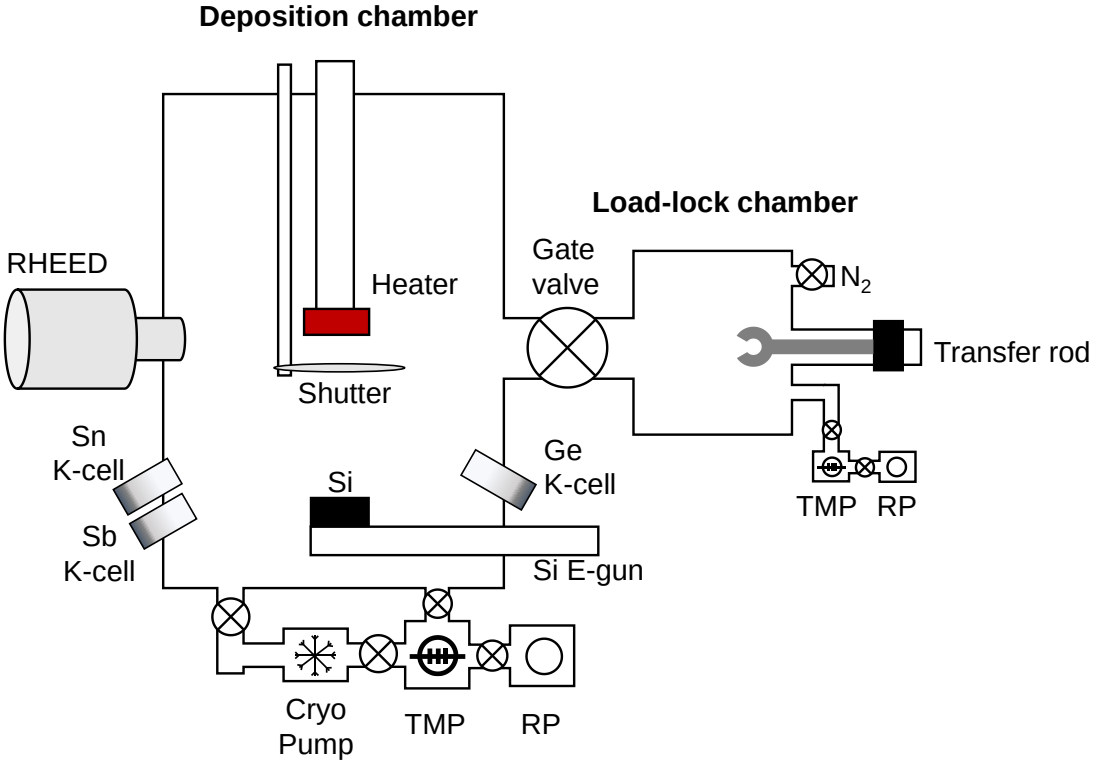

Figure 2.2 The schematic concept of MBE system in this study.

2.2 Sample characterization

2.2.1 Reflection high energy electron diffraction (RHEED)

In this study, the reflection high energy electron diffraction (RHEED) equipment has been installed on the MBE system to observe the surface condition of the *p*-Ge (001) substrate to confirm whether the surface cleaning process is well completed. Additionally, RHEED are also used to verify the growth condition such as the epitaxial growth, strain relaxation and surface flatness for all the samples, including the $Ge_{1-x}Sn_x/Si_yGe_{1-x-y}Sn_x$

heterostructures and the n^+-$Ge_{1-x}Sn_x$ grown in the MBE system. The schematic diagram of the RHEED working principle are shown in **Figure 2.3**. During the operation of RHEED system, the electrons are generated from an electron gun in the deposition chamber and are emitted onto the sample surface at a very small incident angle. The diffraction patterns will be generated by the interference of electromagnetic waves formed by the reflected electrons on the sample surface. Then the diffraction patterns are projected to the observation fluorescent screen. The different types of diffraction pattern are corresponded to the specific surface atom conditions of the sample. By analyzing the shape of the diffraction patterns, the sample surface condition can be understood. Introducing the use of RHEED system during the epitaxial growth process is very helpful to manage the growth parameter in real time, leading to a better epitaxial crystal quality of the heterostructures.

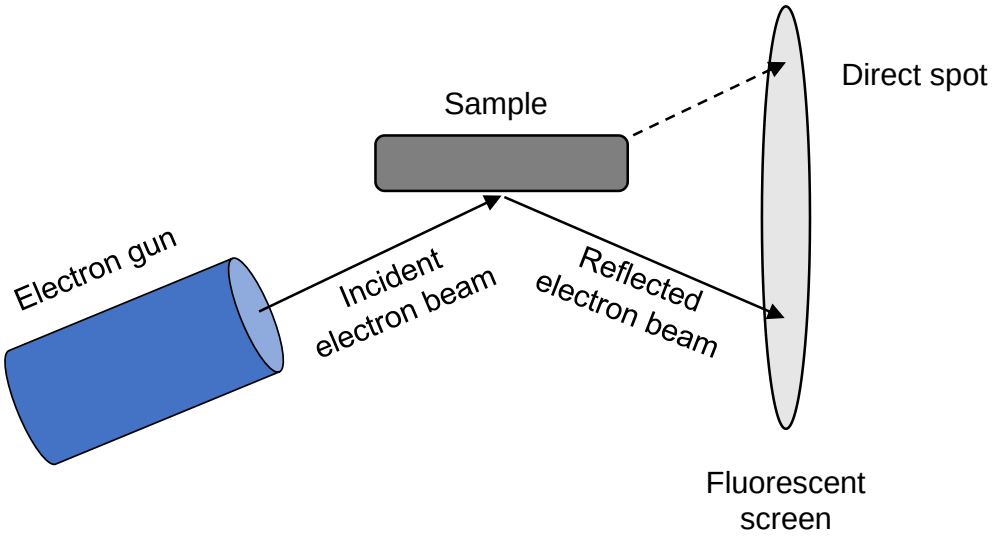

Figure 2.3 The schematic of RHEED.

2.2.2 X-ray diffraction (XRD)

In this study, to investigate the crystal quality, elemental composition as well as strain of the epitaxial $Ge_{1-x}Sn_x/Si_yGe_{1-x-y}Sn_x$ heterostructures and the pseudo-direct transition n^+-

$Ge_{1-x}Sn_x$ thin films, the X-ray diffraction 2θ/ω measurement and two-dimensional reciprocal space mapping (2DRSM) were used. **Figure 2.4** shows the schematic diagram of the XRD equipment (Phillips, X'pert PRO MRD: Material Research Diffractometer). A Cu target was used as the X-ray source, and a high voltage (45 kV) was applied between the filament (filament current: 40 mA) and Cu to generate the characteristic X-rays (Cu Kα1, λ=0.15456 nm). The X-rays were then collected by the X-ray mirror and emitted inside a monochromator which was composed of four-single Ge crystal to obtain a monochromatic light. The monochromatic light was irradiated onto the sample, scattered,

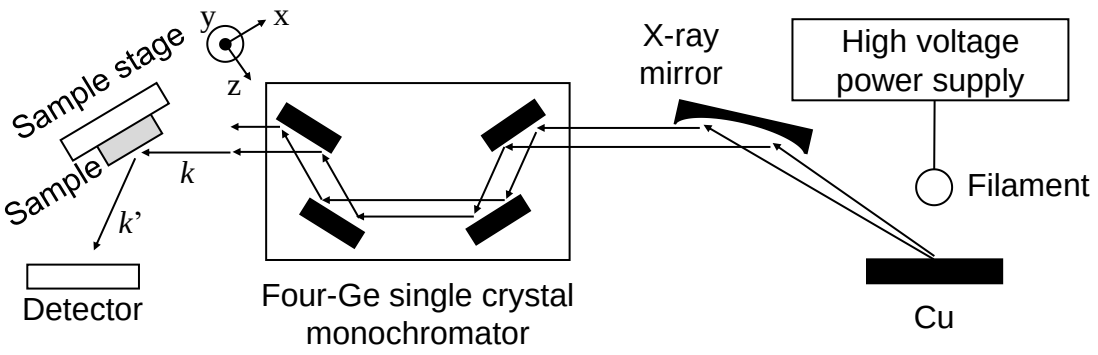

Figure 2.4 the schematic diagram of the XRD equipment.

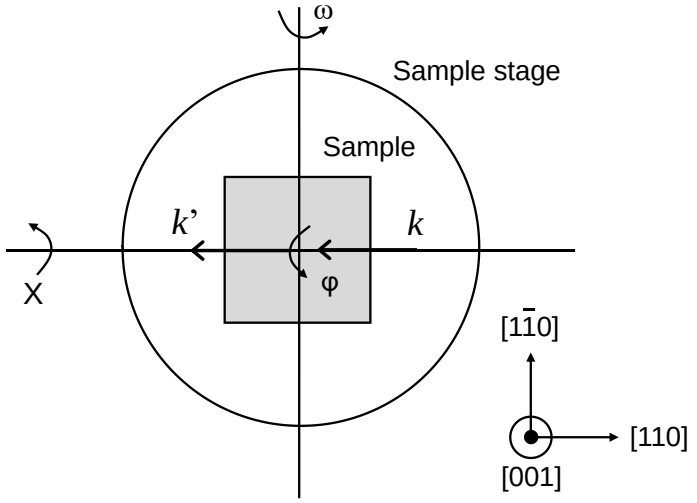

Figure 2.5 The upper view of the sample stage including its rotation axis.

and detected by the detector. Here, incident wave vector is labeled as *k* and the scattered wave vector is labeled as *k*'.

The upper view of the sample stage including its rotation axis is shown in **Figure 2.5**. In the 2θ/ω measurement, the incident angle ω and the reflection angle θ of the X-ray are set to the same value. During the measurement, the angles are varied from a specific range and the corresponded diffraction X-ray intensities are measured. When the angular position of the incident and reflection X-ray are corresponded to the Bragg reflection condition of the sample in terms of its lattice constant and orientation, the intensity of diffraction X-ray will increase dramatically and a "diffraction peak" can be observed from the measurement result. For a complex epitaxial heterostructure sample, it usually contains multiple crystal structures, and several diffraction peaks can be observed from the 2θ/ω measurement. By carefully analyze the detailed parameters of these diffraction peaks, the information of the sample's crystal structure such as lattice constant, strain and elemental composition can be obtained. In this study, the 2θ/ω and ω rocking curve

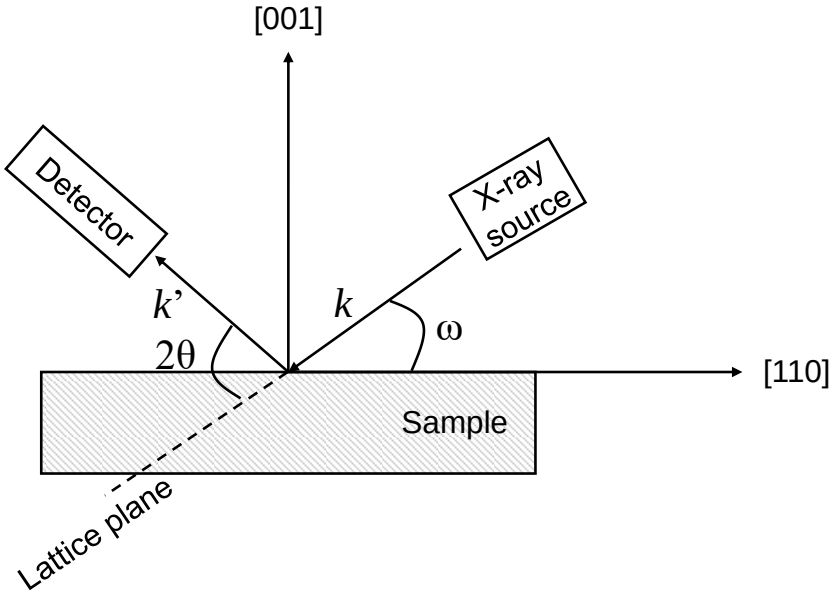

Figure 2.6 The measurement of XRD-2DRSM in real space.

measurement has been performed around the 004 Bragg reflection point of the Ge(001) substrate to investigate the crystallinity, relatively defect densities as well as elemental composition of the prepared epitaxial heterostructures.

The XRD-2DRSM measurement has been also used in this study. **Figure 2.6** shows the measurement principle of XRD-2DRSM in real space. All prepared samples in this study are epitaxially grown on the *p*-Ge(001) substrate, to measure the Ge004 along with the epitaxial layers' diffraction peaks, the incident wave vector *k* along the [110] axis is used. The ω is the internal angle between the (004) plane and the incident wave vector *k*, and 2θ is the internal angle between the incident *k* and reflection *k*' wave vectors.

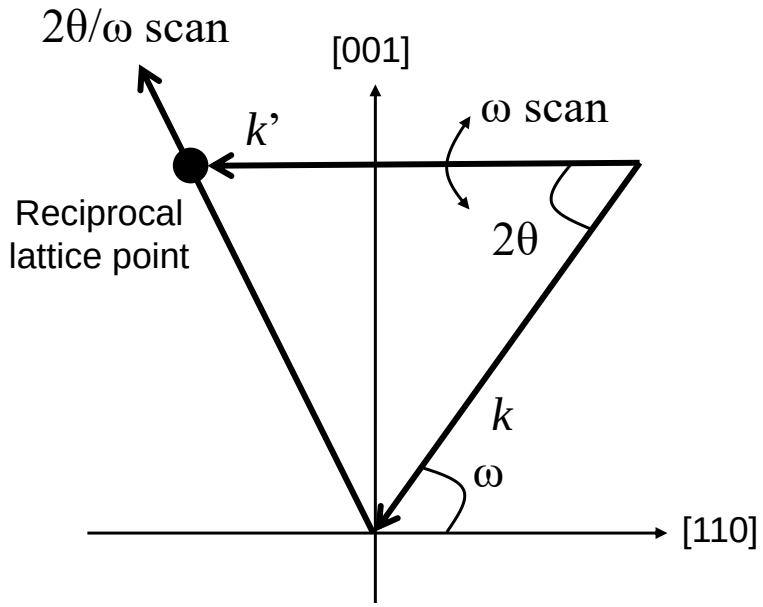

Figure 2.7 The measurement of XRD-2DRSM in reciprocal space.

The corresponding XRD-2DRSM measurement in reciprocal space is shown in **Figure 2.7**. By varying the angular position of 2θ and ω simultaneously, it is possible to map the diffraction peaks around the $\overline{2}\overline{2}4$ reciprocal lattice point in the reciprocal space. The reciprocal lattice space coordinates (Q_x, Q_y) are defined by the angular position of 2θ,

ω, and the wavelength λ of the X-ray. The Q_x and Q_y definition equations are listed below:

$$Q_x = \frac{1}{\lambda}\{cos\,\omega - cos(2\theta - \omega)\}, \quad (2.1)$$

$$Q_y = \frac{1}{\lambda}\{sin\,\omega + sin(2\theta - \omega)\}. \quad (2.2)$$

Additionally, the substitutional Sn content in $Ge_{1-x}Sn_x$ causes the linear shift of the diffraction peak position between the $Ge\overline{2}\overline{2}4$ and the $Sn\overline{2}\overline{2}4$ lattice point. The lattice constant of the $Ge_{1-x}Sn_x$ can be estimated by assuming elastic deformation by using the Vegard's law,

$$a_{GeSn}(x) = a_{Ge}(1 - x) + a_{Sn}x. \quad (2.3)$$

Here, a_{GeSn} is the lattice constant of the $Ge_{1-x}Sn_x$, and the a_{Ge} and a_{Sn} are the lattice constants of bulk Ge (0.56579 nm) and α-Sn (0.64892 nm), respectively.[2] x is the substitutional Sn content in $Ge_{1-x}Sn_x$. Note that the calculation of **Equation (2.3)** is assumed in the strain-free condition. In practical situation, where the $Ge_{1-x}Sn_x$ is pseudomorphically grown on the Ge [001] orientation, the lattice constant of $Ge_{1-x}Sn_x$ along the [001] direction is expressed in **Equation (2.4)** by introducing the Poisson ration of $Ge_{1-x}Sn_x$ (ν_{GeSn})[3] as:

$$a_{GeSn[001]} = \frac{1 + \nu_{GeSn}}{1 - \nu_{GeSn}} a_{GeSn} - \frac{2\nu_{GeSn}}{1 - \nu_{GeSn}} a_{Ge}. \quad (2.4)$$

Here, the Poisson ration of $Ge_{1-x}Sn_x$ ν_{GeSn} is given by a linear **equation (2.5)**:

$$\nu_{GeSn}(x) = \nu_{Ge}(1 - x) + \nu_{Sn}x. \quad (2.5)$$

Similarly, v_{Ge} and v_{Sn} are the Poisson ration of bulk Ge (0.273) and α-Sn (0.356),[4] and x is the substitutional Sn content in $Ge_{1-x}Sn_x$.

2.2.3 Estimation of composition and strain of $Si_yGe_{1-x-y}Sn_x$ epitaxial layers

Unlike the $Ge_{1-x}Sn_x$ in which its lattice constant can be determined from only Sn composition and strain. The $Si_yGe_{1-x-y}Sn_x$ is a ternary alloy, and its lattice constant is determined by three variables: the Si and Sn composition and strain. Therefore, the way to calculate its elemental composition and strain is different from the $Ge_{1-x}Sn_x$ and cannot be estimated from the XRD-2DRSM alone. In this study, the elemental composition as well as strain of the epitaxial $Si_yGe_{1-x-y}Sn_x$ was calculated by combining the XRD-2DRSM with Raman spectroscopy. This method is proposed by V. R. D'Costa.[4] The detailed calculation is described as the following parts.

Firstly, the $Si_yGe_{1-x-y}Sn_x$ strain (ε) was estimated from the XRD-2DRSM result. And then the $Si_yGe_{1-x-y}Sn_x$ diffraction peak is assumed into the $Ge_{1-A}Sn_A$ diffraction peak that has the same reciprocal lattice space coordinates Q_x and Q_y (which means that the assumed $Ge_{1-x}Sn_x$ has the same strained lattice constant with $Si_yGe_{1-x-y}Sn_x$). The Sn composition A of the $Ge_{1-A}Sn_A$ diffraction peak can be calculated from the Q_x and Q_y coordinates. Since the fully strain-relaxed $Ge_{1-A}Sn_A$ should have the equal lattice constant with the same fully strain-relaxed $Si_yGe_{1-x-y}Sn_x$, the following equation can be written as **Equation (2.6)**,

$$\begin{aligned} a_{Si}y + a_{Ge}(1-x-y)a_{Sn}x + b_{GeSn}(1-x-y)x \\ + b_{SiGe}(1-x-y)y + b_{SiSn}xy \\ = a_{Ge}\,(1-A) + a_{Sn}A + b_{GeSn}(1-A)A \end{aligned} \tag{2.6}$$

Here, a_{Ge}, a_{Si} and a_{Sn} are the lattice constant of bulk Ge, Si, and α-Sn. b_{SiGe}, b_{SiSn} and b_{GeSn} are the bowing parameters of the lattice constants, these parameters are extracted from references and are listed in **Table 2.1**.[4–7] The Si composition x in $Si_yGe_{1-x-y}Sn_x$ can be then expressed as **Equation (2.7)**,

$$x = \frac{-Y \pm \sqrt{Y^2 - 4XZ}}{2X} \tag{2.7}$$

The X, Y and Z are the simplified parameters for the easiness of calculation, and the original forms are expressed as follows,

$$X = b_{SiGe} \tag{2.8}$$

$$Y = a_{Ge} - a_{Si} - b_{SiGe} + y(b_{GeSn} + b_{SiGe} - b_{SiSn}) \tag{2.9}$$

$$Z = (a_{Sn} - a_{Ge} + b_{GeSn})(A - y) - (A^2 - y^2)b_{GeSn} \tag{2.10}$$

Combing **Equation (2.7)~(2.10)**, the x can be expressed by using y as the only variable. And from the Raman spectroscopy measurement, the Ge-Ge binding's peak wave vector position ω_{Ge-Ge} can be written as

$$\omega_{Ge-Ge} = \omega_0^{Ge} - xa_{Ge-Ge}^{SiGe} - ya_{Ge-Ge}^{GeSn} + b_{Ge-Ge}\varepsilon \tag{2.11}$$

Using the aforementioned equations, the Si and Sn composition of epitaxial $Si_yGe_{1-x-y}Sn_x$ in this can be accurately estimated.

Table 2.1 Summary of calculation parameters used in section 2.2.3.[4-7)]

a_{Si} (nm)	0.543
a_{Ge} (nm)	0.566
a_{Sn} (nm)	0.649
b_{GeSn} (nm)	0.0041
b_{SiGe} (nm)	-0.0026
b_{SiSn} (nm)	0
$\omega_0^{Ge\text{-}Ge}$ (1/cm)	301
a^{SiGe} (1/cm)	17.1
a^{GeSn} (1/cm)	94
$b_{Ge\text{-}Ge}$(1/cm)	-415

2.2.4 The theory calculation of energy bandgap alignment for heterostructure interfaces

In this study, we used C. G. Van de Walle's model solid approximation[8)] to calculate the band alignment of the prepared samples. This method has already been widely used by several groups to perform theory band structure prediction for group-IV semiconductors like $Si_yGe_{1-x-y}Sn_x$, $Ge_{1-x}Sn_x$ and Si_yGe_{1-y}.[9–11)] We took $Ge_{1-x}Sn_x$ as example and used linear interpolation technique to obtain parameters of $Ge_{1-x}Sn_x$ from bulk Ge and Sn. The average of three valence band edge at the Γ point was calculated considering the deformation potential and spin-off effect, a strained valence band of $Ge_{1-x}Sn_x$ is given by:

$$E_v(Ge_{1-x}Sn_x) = E_{v,av,strain}(Ge_{1-x}Sn_x) + \frac{1}{3}\Delta_{SO}(Ge_{1-x}Sn_x) \qquad (2.12)$$

here, $E_v(Ge_{1-x}Sn_x)$ and $\Delta_{SO}(Ge_{1-x}Sn_x)$ are the average valence band edge under a strain condition and spin orbit splitting energy of $Ge_{1-x}Sn_x$, respectively.

The strained average valence band was calculated by adding the deformation potential into the strain-free average valence band, as our samples grown along Ge(001) axis, the 2-axis strain along surface ε_{xx} and ε_{yy} are the same, and the calculation is given by:

$$E_{v,av,strain}(Ge_{1-x}Sn_x) = E_{v,av}(Ge_{1-x}Sn_x) + ((1-x)a_{v,Ge} + xa_{v,Sn})(\varepsilon_{xx} + \varepsilon_{yy} + \varepsilon_{zz}) \quad (2.13)$$

where $E_{v,av}(Ge_{1-x}Sn_x)$ is the strain-free average valence band, $a_{v,Ge}$ and $a_{v,Sn}$ are the hydrostatic deformation potential for valence band of bulk Ge and Sn, respectively. ε_{xx} , ε_{yy} and ε_{zz} are the strain along x, y, and z axis, respectively.

The bandgap at a specific energy valley is given by:

$$E_g(Ge_{1-x}Sn_x) = (1-x)E_{g,Ge} + xE_{g,Sn} - x(1-x)b_{GeSn} \quad (2.14)$$

here, $E_{g,Ge}$ and $E_{g,Sn}$ are the bandgap of bulk Ge and α-Sn, respectively, b_{GeSn} is the bowing parameter of $Ge_{1-x}Sn_x$, calculation parameters for L and Γ valley are listed in **Table 2.2**.

The strain-free conduction band at a specific energy valley of $Ge_{1-x}Sn_x$ is given by:

$$E_c(Ge_{1-x}Sn_x) = E_v(Ge_{1-x}Sn_x) + E_g(Ge_{1-x}Sn_x) \quad (2.15)$$

Table 2.2 Band parameters at L and Γ valley used in the band alignment calculation, extracted form ref. [9-11].

	L valley	Γ valley
$E_{v,av,Ge}$ (eV)	-	0
$E_{v,av,Sn}$ (eV)	-	0.69
$E_{g,Ge}$ (eV)	0.66	0.795
$E_{g,Sn}$ (eV)	0.09	-0.413
b_{GeSn} (eV)	1.23	1.94
$\Delta_{SO,Ge}$ (eV)	-	0.295
$\Delta_{SO,Sn}$ (eV)	-	0.8
$a_{v,Ge}$ (eV)	-	1.24
$a_{v,Sn}$ (eV)	-	1.58
$a_{c,Ge}$ (eV)	-1.54	-8.24
$a_{c,Sn}$ (eV)	-2.14	-6

As strain will also cause deformation on conduction band, a deformation potential was added to obtain strained conduction band:

$$E_{c,strain}(Ge_{1-x}Sn_x) = E_{c,av}(Ge_{1-x}Sn_x) + ((1-x)a_{c,Ge} + xa_{c,Sn})(\varepsilon_{xx} + \varepsilon_{yy} + \varepsilon_{zz}) \quad (2.16)$$

where $E_{c,av}(Ge_{1-x}Sn_x)$ is the strain-free conduction band edge, $a_{c,Ge}$ and $a_{c,Sn}$ are the hydrostatic deformation potential for conduction band of bulk Ge and α-Sn, respectively.

At last, the bandgap under strain which is defined as the difference between the edge of valence band and conduction band is obtained:

$$E_{g,strain}(Ge_{1-x}Sn_x) = E_{c,strain}(Ge_{1-x}Sn_x) - E_v(Ge_{1-x}Sn_x) \quad (2.17)$$

The calculation result for $Ge_{0.94}Sn_{0.06}$ and $Ge_{0.91}Sn_{0.09}$ are listed in **Table 2.3** as an example:

Table 2.3 Band alignment calculation result for $Ge_{0.94}Sn_{0.06}$ and $Ge_{0.91}Sn_{0.09}$.

	$Ge_{0.94}Sn_{0.06}$	$Ge_{0.91}Sn_{0.09}$
$E_{v,av}$ (eV)	0.041	0.062
$E_{v,av,strain}$ (eV)	0.028	0.041
E_v (eV)	0.136	0.155
$E_{g,L}$ (eV)	0.556	0.508
$E_{g,\Gamma}$ (eV)	0.613	0.527
$E_{c,L}$ (eV)	0.693	0.663
$E_{c,\Gamma}$ (eV)	0.749	0.682
$E_{c,L,strain}$ (eV)	0.710	0.689
$E_{c,\Gamma,strain}$ (eV)	0.838	0.813
$E_{g,L,strain}$ (eV)	0.574	0.534
$E_{g,\Gamma,strain}$ (eV)	0.702	0.658

2.2.5 The Photoluminescence (PL) Spectroscopy measurement

2.2.5.1 The PL measurement system

In this study, the photoluminescence spectroscopy (PL) measurement was used to evaluate the light emission property of the prepared samples. In the PL measurement, the electrons at the valence band of the samples are excited by light irradiation to produce electron-hole pairs, and the subsequently occurred recombination of the electron-hole pairs will lead to the emission of the luminescence that corresponded to the energy band

properties of samples. Here, **Figure 2.8** shows the measurement principle of the PL measurement system in this study. An yttrium aluminum-garnet laser (YAG laser, wavelength: 532 nm) was used as the excitation light source with the adjustable pumping power, and an InAs photovoltaic detector (Hamamatsu Photonics, P7163) was used as the detector. The slits, hale-wave plate, prism, chopper as well as mirrors were used to block the unnecessary reflection light in the optical path and minor laser component from the YAG laser. A long pass filter was set at the entrance of the spectrometer to prevent any light wave lower than 1400 nm passing. The measurement temperature of samples were controlled by a cryostat (Montana Instruments, Cryostation) ranged from 3 to 350 K and can be monitored on the backside at the sample stage.

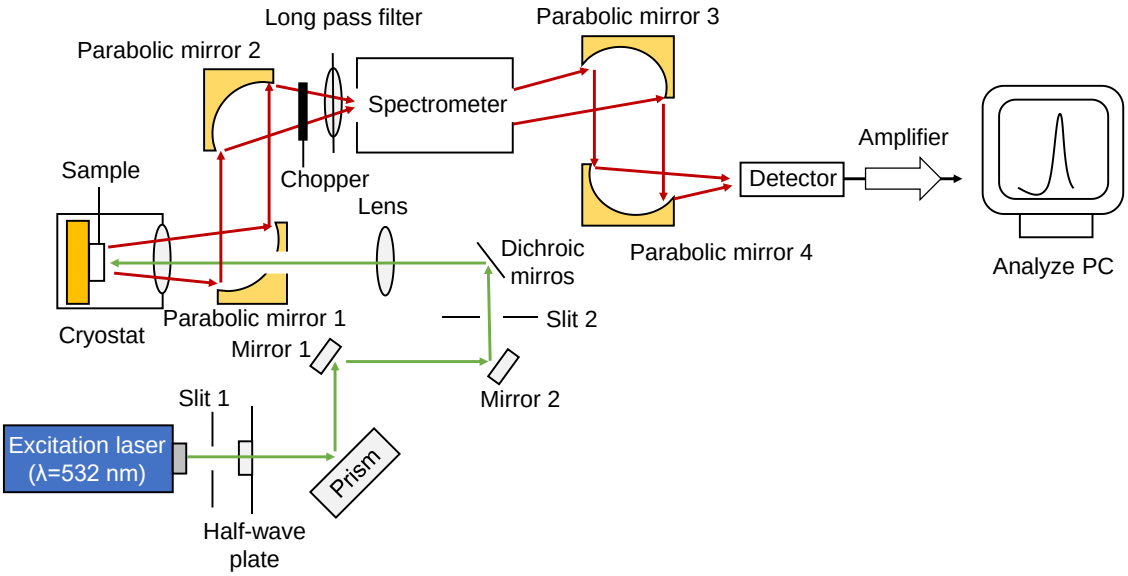

Figure 2.8 The simplified diagram of the PL measurement system.

2.2.5.2 The plot and sensitivity calibration of PL measurement

In the PL measurement experiment, the sensitive and calibration of the measured signals are very important. **Figure 2.9 (a)** shows the PL spectra measurement result of a standard infrared light source (Newport, Oriel 6580), blue line is the one measured by our PL measurement system (range: 0.41-0.77 eV) and orange line is the standard PL spectra provided by its producer. We normalized two spectra and compared their normalized intensity. We found out that the normalized intensity of the standard spectra was in a trend of decrease, while our measurement result had a different line profile that contained a more complex trend. This suggests that (i) the original PL intensity of the standard infrared light source is in a decrease within energy range of 0.41-0.77 eV and (ii) our PL measurement system has different sensitivity for different photon energy that cause a different trend.

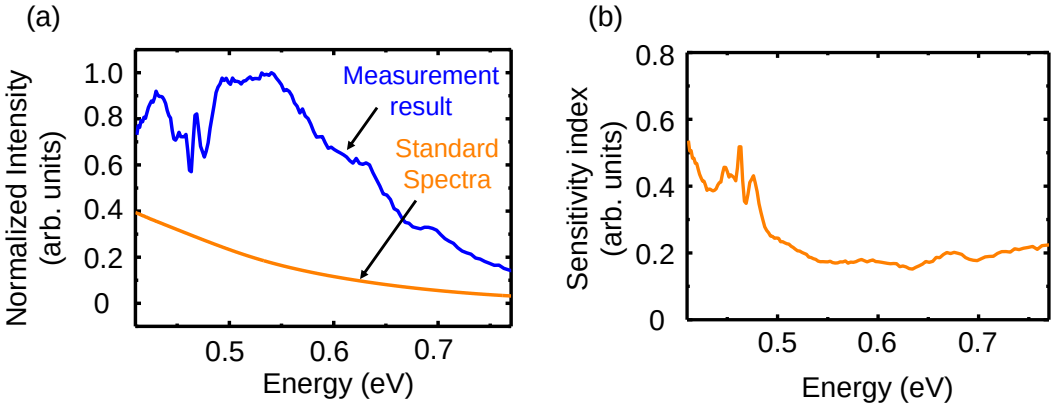

Figure 2.9 (a) PL spectra comparison of a standard infrared light source between its standard spectra and our PL measurement result. (b) Sensitivity index calculated for each energy point.

Therefore, a calibration for sensitivity is required for our PL measurement system, we calculated the sensitivity index which is defined by:

$$SI_n = \frac{R_{SIR,n}}{R_{MIR,n}} \tag{2.18}$$

where n stands for a specific energy point, $R_{SIR,n}$ is the normalized intensity of standard spectra, $R_{MIR,n}$ the is normalized intensity of measurement result. The calculation result of the sensitivity index is plotted in **Figure 2.9 (b)**.

We then used the sensitivity index to calibrate our sample's raw PL measurement result. The calibration is carried out by:

$$R_n = R_{raw,n} \times SI_n \tag{2.18}$$

where n stands for a specific energy point, R_n is the calibrated PL intensity, $R_{raw,n}$ is the PL intensity of raw data.

Figures 2.10 (a) and **(b)** show the raw PL spectra and calibrated PL spectra for one of our prepared samples, an 80-nm-thick n^+-$Ge_{0.935}Sn_{0.65}$ layer with a doping concentration of 10^{20} cm^{-3}. Note that all the PL spectra result showed in this study are all calibrated by the calibration process in this section.

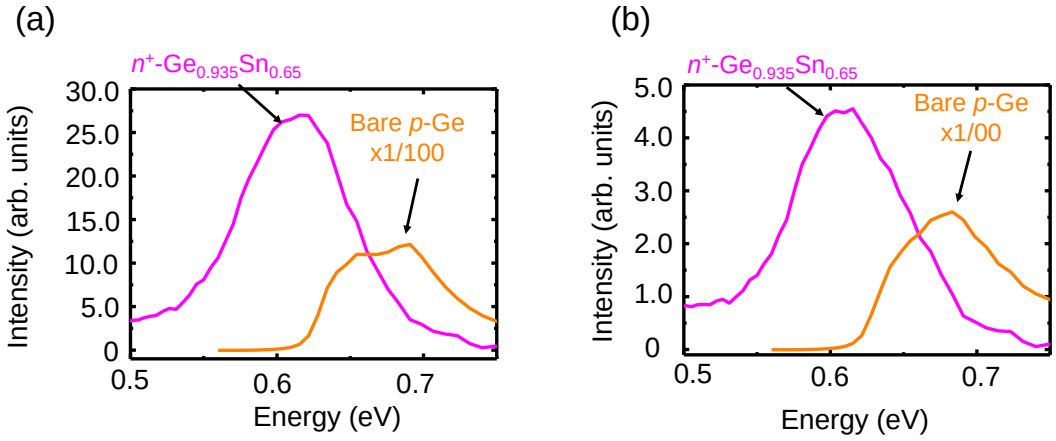

Figure 2.10 (a) Raw PL measurement result and (b) PL spectra calibrated using sensitivity index of n^+-$Ge_{0.935}Sn_{0.65}$ and a bare p-Ge.

References

1) J. Jeon, T. Asano, Y. Shimura, W. Takeuchi, M. Kurosawa, M. Sakashita, O. Nakatsuka and S. Zaima, Jpn. J. Appl. Phys. **55** (4S), 04EB13 (2016).

2) O. Madelung Semiconductors Data Handbook, Springer, (2004).

3) J. M. Hartmann, B. Gallas, J. Zhang and J. J. Harris, Semicond. Sci. Technol. **15** (4), 370 (2000).

4) V. R. D'Costa, C. S. Cook, A. G. Birdwell, C. L. Littler, M. Canonico, S. Zollner, J. Kouvetakis and J. Menéndez, Phys. Rev. B **73** (12), 125207 (2006).

5) H. K. Shin, D. J. Lockwood, C. Lacelle and P. J. Poole, Journal of Applied Physics **88** (11), 6423 (2000).

6) D. De Salvador, M. Petrovich, M. Berti, F. Romanato, E. Napolitani, A. Drigo, J. Stangl, S. Zerlauth, M. Mühlberger, F. Schäffler, G. Bauer and P. Kelires, Physical Review B **61**, 13005 (2000).

7) Y. Nagae, M. Kurosawa, S. Shibayama, M. Araidai, M. Sakashita, O. Nakatsuka, K. Shiraishi and S. Zaima, Jpn. J. Appl. Phys. **55** (8S2), 08PE04 (2016).

8) C. G. Van de Walle, Phys. Rev. B **39** (3), 1871 (1989).

9) R. Ranjan and M. K. Das, Opt Quant Electron **48** (3), 201 (2016).

10) G. Sun, R. A. Soref and H. H. Cheng, Opt. Express, OE **18** (19), 19957 (2010).

11) G. Chang, S. Chang and S. L. Chuang, IEEE Journal of Quantum Electronics **46** (12), 1813 (2010).

Chapter 3 Formation of the $Ge_{1-x}Sn_x$/high-Si-content-$Si_yGe_{1-x-y}Sn_x$ double-quantum wells and characterization of their luminescence performance

3.1 Overview

As we discussed in the background, the group-IV light source is the key component to realize the Si platform integrated optical interconnect. The binary $Ge_{1-x}Sn_x$ alloy semiconductor is a promising light emission material for this concept. Until now, the ideal room temperature lasing from the $Ge_{1-x}Sn_x$ has not been achieved yet. The appropriate structure formations, such as the micro-disk structure and the multi-quantum well structure is essential to increase the lasing temperature threshold. And the establishment of effective carrier confinement for $Ge_{1-x}Sn_x$ is also benefit for the enhancement of luminescence performance as well as RT lasing.

Our purpose in this study is to examine the formation of the $Ge_{1-x}Sn_x$/high-Si-content-$Si_yGe_{1-x-y}Sn_x$ double-QWs using low-temperature MBE method and to characterize their optoelectronic properties so we can provide more knowledge for the realizing of the $Ge_{1-x}Sn_x/Si_yGe_{1-x-y}Sn_x$ MQWs semiconductor laser devices for the optical interconnect structure. There're already several reports have been published that suggest the $Ge_{1-x}Sn_x$ epitaxial layer grown by low-temperature MBE method could achieve the superior crystallinity.[1),2)] However, the impact of the growth temperature of $Si_yGe_{1-x-y}Sn_x$ layer on the crystalline and optoelectronic properties has not been systematically clarified yet. Therefore, in this chapter, we firstly discussed the impact of growth temperature on the

$Ge_{1-x}Sn_x$/high-Si-content-$Si_yGe_{1-x-y}Sn_x$ single-QW. Based on the finding of this discussion, we challenged the formation of $Ge_{1-x}Sn_x$/high-Si-content-$Si_yGe_{1-x-y}Sn_x$ double-QWs grown at a low temperature of 100 °C. Furthermore, we discussed the thermal stability from the perspective of the practical device fabrication process, we investigated the thermal stability of the $Ge_{1-x}Sn_x$/high-Si-content-$Si_yGe_{1-x-y}Sn_x$ single- and double-QWs against the hydrogen and nitrogen annealing. The impact of annealing temperature on the crystalline and PL performance of the single- and double-QWs were also discussed.

The part of this chapter included results and discussions from our previously published paper.[3)]

3.2 Experimental procedure

The substrate cleaning and epitaxial growth of the samples are written in the **section 2.1.1 and 2.1.2**. Here, the $Ge_{1-x}Sn_x$/$Si_yGe_{1-x-y}Sn_x$ single- and double-QWs were prepared. Firstly, we examined the formation of the $Si_yGe_{1-x-y}Sn_x$/$Ge_{1-x}Sn_x$/$Si_yGe_{1-x-y}Sn_x$ double heterostructure (DHS). In this chapter, the DHS is called as the single-QW for the better comparison with the double-QWs samples. The thicknesses of $Si_yGe_{1-x-y}Sn_x$ and $Ge_{1-x}Sn_x$ layers were 30 and 15 nm, respectively. In order to realize the lattice matched $Si_yGe_{1-x-y}Sn_x$ layer on Ge with its Si content higher than 20%, the Si and Sn contents of $Si_yGe_{1-x-y}Sn_x$ were designed to be ~26% and 8%, respectively. Also, the Sn content of $Ge_{1-x}Sn_x$ layer was designed to be ~6% for the easiness of the pseudomorphic growth. Since the first objective in this study is to discuss the impact of growth temperature of $Si_yGe_{1-x-y}Sn_x$ layers T_{SiGeSn}, on the crystalline and luminescence performance of the $Ge_{1-x}Sn_x$/$Si_yGe_{1-x-y}Sn_x$ single-QW. The T_{SiGeSn} was adjusted from 100–200 °C, whereas

the growth temperature of $Ge_{1-x}Sn_x$ was fixed at 150 °C as is same for our previous reports.[2,4)]

Next, the epitaxial growth of $Si_yGe_{1-x-y}Sn_x/Ge_{1-x}Sn_x/Si_yGe_{1-x-y}Sn_x$ double-QWs samples were carried out. The thickness of each layer of the doble-QWs was designed to be the same value, 15 nm for the simplicity. In terms for the growth temperature of the double-QWs, $T_{g,DQW}$, all layers were grown under the fixed temperature. We prepared two double-QWs samples with their $T_{g,DQW}$ fixed at 100 and 140 °C, respectively. The Si and Sn contents of $Si_yGe_{1-x-y}Sn_x$ in both double-QWs samples were designed to be ~26% and 8%, respectively. The Sn content of $Ge_{1-x}Sn_x$ was designed to be ~ 9%. **Table 3.1** lists the prepared single- and double-QWs samples detailed information including the sample structure, element contents, thickness, and growth temperatures of each layer.

To investigate the thermal stability of the as-grown single- and double-QWs sample, we performed the post deposition annealing (PDA) at 200–500 °C for 5 min in H_2 and N_2 atmosphere and discussed their PDA effects.

The details of the crystalline characterization method and PL measurement principle are written in chapter 2. Notably, the 532 nm excitation laser used for the PL measurement in this chapter was fixed at the power of 1.5 W.

Table 3.1 Summary of sample structure, element contents, thickness, and growth temperatures of each layer in the prepared $Ge_{1-x}Sn_x/Si_yGe_{1-x-y}Sn_x$ single- and double-QWs samples.

Sample ID	Sample structure	$Ge_{1-x}Sn_x$ layer				$Si_yGe_{1-x-y}Sn_x$ layer				
		Contents (%)		Thickness (nm)	T_{GeSn} (°C)	Contents (%)			Thickness (nm)	T_{SiGeSn} (°C)
		Ge	Sn			Si	Ge	Sn		
SQW-1	$Si_yGe_{1-x-y}Sn_x/Ge_{1-x}Sn_x/Si_yGe_{1-x-y}Sn_x$	94	6	15	150	26	66	8	30	100
SQW-2		94	6	15	150	26	66	8	30	150
SQW-3		94	6	15	150	26	66	8	30	200
DQW-1	$Si_yGe_{1-x-y}Sn_x/Ge_{1-x}Sn_x/Si_yGe_{1-x-y}Sn_x/$ $Ge_{1-x}Sn_x/Si_yGe_{1-x-y}Sn_x$	91	9	15	100	26	66	8	15	100
DQW-2		91	9	15	140	26	66	8	15	140

3.3 Results and discussion

3.3.1 Impact of growth temperature of $Si_yGe_{1-x-y}Sn_x$ layer on crystalline and PL properties of $Ge_{1-x}Sn_x/Si_yGe_{1-x-y}Sn_x$ single-QW structure

First of all, the impact of T_{SiGeSn} on the crystalline and PL properties of the $Ge_{1-x}Sn_x/Si_yGe_{1-x-y}Sn_x$ single-QW has been discussed. **Figures 3.1 (a)-(f)** show the XRD-2DRSM and AFM results of single-QW samples SQW-1 to SQW-3 in terms of the different T_{SiGeSn}; (a,d) SQW-1 (T_{SiGeSn} = 100 °C), (b,e) SQW-2 (T_{SiGeSn} = 150 °C), and (c,f) SQW-3 (T_{SiGeSn} = 200 °C), respectively. XRD-2DRSM were measured around the Ge $\overline{2}\overline{2}4$ reciprocal lattice point. All diffraction peaks related to the epitaxial layers in the three XRD-2DRSM results have the same reciprocal space Q_x value to the Ge substrate, indicating that all epitaxial layers of the single-QW samples SQW-1 to SQW-3 are pseudomorphically grown on the Ge(001) substrate regardless of their crystallinity. Therefore, in the range of T_{SiGeSn} from 100-200 °C, the epitaxial growth of pseudomorphic $Ge_{1-x}Sn_x/Si_yGe_{1-x-y}Sn_x$ single-QW is achievable.

Next, we continue to discuss the impact of T_{SiGeSn} on the crystalline of the $Ge_{1-x}Sn_x/Si_yGe_{1-x-y}Sn_x$ single-QW formation. In **Figure 3.1 (a)**, we observed the overlap of diffraction peaks of $Si_yGe_{1-x-y}Sn_x$ and Ge layers, suggesting that the $Si_yGe_{1-x-y}Sn_x$ layer is grown with the lattice-matching condition of desired contents. We combined the Raman analysis in addition to the XRD-2DRSM result and estimated $Si_yGe_{1-x-y}Sn_x$ layer's Si and Sn contents to 24% and 6%, respectively. On the other hand, we also observed the diffraction peak of the $Ge_{1-x}Sn_x$ layer, which is distant from the Ge and the overlapped $Si_yGe_{1-x-y}Sn_x$ peaks. The Sn content in the $Ge_{1-x}Sn_x$ layer was estimated to 6.5% from the

peak position with assuming the Vegard's law. Additionally, we can clearly observe thickness fringes around the epitaxial $Ge_{0.935}Sn_{0.065}$ and $Si_{0.24}Ge_{0.70}Sn_{0.06}$ peaks, indicating that uniform and steep interfaces between the epitaxial layers are formed. From the observation of **Figure 3.1 (a)**, we can conclude that SQW-1 has a superior crystallinity, and its surface flatness has also been verified form the AFM observation as shown in **Figure 3.1 (d)**, a flat surface with the root mean square (RMS) roughness of only 0.40 nm has been confirmed, which is even comparable to the bare Ge substrate.

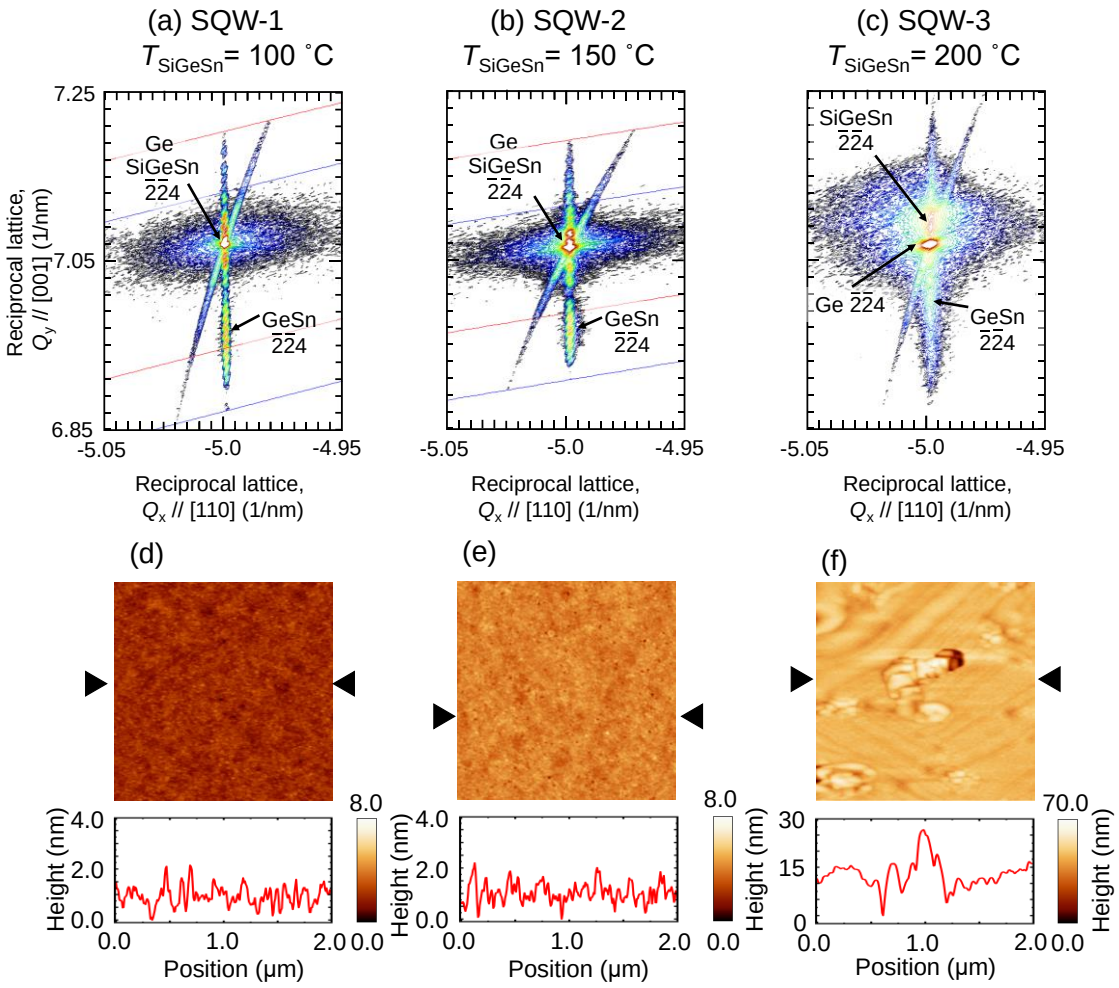

Figure 3.1 XRD-2DRSM results and AFM images with corresponding line profile of the single-QW samples (a, d) SQW-1 (T_{SiGeSn}=100 °C), (b, e) SQW-2 (T_{SiGeSn}=150 °C), and (c, f) SQW-3 (T_{SiGeSn}=200 °C).

For sample SQW-2 with T_{SiGeSn} of 150 °C, the XRD-2DRSM result is shown in **Figure 3.1 (b)**, the overlap of $Si_yGe_{1-x-y}Sn_x$ and Ge, as well as the individual $Ge_{1-x}Sn_x$ diffraction peaks were also observed. The estimated element contents of the $Si_yGe_{1-x-y}Sn_x$ and $Ge_{1-x}Sn_x$ layers were the same with sample SQW-1. We also observed the thickness fringes around the $Ge_{0.935}Sn_{0.065}$ and $Si_{0.24}Ge_{0.70}Sn_{0.06}$ epitaxial diffraction peaks, so the similar uniform and steep interfaces around epitaxial layers should also be formed in sample SQW-2. However, the $Ge_{1-x}Sn_x$ peak and related thickness fringes of SQW-2 are slightly broadened on the Q_x axis, while SQW-1 exhibits a much sharper $Ge_{1-x}Sn_x$ diffraction peak. This Inferring a crystallinity degradation of SQW-2, which is likely caused by the T_{SiGeSn} at 150 °C, and the superior crystallinity of epitaxial layers can be obtained by a lower growth temperature at T_{SiGeSn} of 100 °C in SQW-1. The surface morphology of sample SQW-2 are shown in **Figure 3.1 (e)**, and a relative flat surface with RMS roughness at 0.40 nm was observed. Although the AFM image has a brighter color in contrast to the sample SQW-1, we didn't observe further influence of the T_{SiGeSn} at 150 °C to the single-QW sample's surface morphology.

In contrast to sample SQW-1 and SQW-2, the sample SQW-3 with a higher T_{SiGeSn} of 200 °C showed a significant crystallinity degradation as shown in the XRD-2DRSM result of **Figure 3.1(c)**; the shift of the diffraction peak position for the $Si_yGe_{1-x-y}Sn_x$ layer from that of Ge, the clearly seen peak broadening on both Q_x and Q_y axis, and the absent of the thickness fringes. A poor crystallinity of SQW-3 can be concluded from this evidence. Moreover, in the AFM image of SQW-3, as shown in **Figure 3.1 (f)**, the surface roughening (RMS roughness: 4.74 nm) with the products of agglomeration can be clearly observed. Considering that $Ge_{1-x}Sn_x$ diffraction peak's position of SQW-3 has also shifted from that of SQW-1 and SQW-2, it is likely that the Sn precipitation occurred in sample

SQW-3. This suggests that the T_{SiGeSn} of 200 °C is overly inappropriate for the $Ge_{1-x}Sn_x/Si_yGe_{1-x-y}Sn_x$ single-QW structure, resulting in the degraded poor crystallinity. Therefore, based on the discussion of **Figure 3.1 (a)~(f)**, the growth temperature of $Si_{0.24}Ge_{0.70}Sn_{0.06}$ epitaxial layer should be lower than 150 °C to suppress the Sn segregation and to realize high crystalline.

Next, we investigate the influence of T_{SiGeSn} on single-QW sample's luminescence properties, the PL measurement were carried out for this purpose. **Figure 3.2 (a)** shows PL spectra measured at RT for the single-QW samples SQW-1, SQW-2 and SQW-3 with T_{SiGeSn} of 100, 150, and 200 °C, respectively. Among three PL spectra profiles, the sample with lower T_{SiGeSn} showed a higher PL intensity. This suggests that the superior crystallinity of the $Ge_{1-x}Sn_x/Si_yGe_{1-x-y}Sn_x$ single-QW leads to an inherently efficient of the PL performance. This positive effect of high crystallinity on the PL efficiency agrees well with our previous reports.[7] For the spectra of sample SQW-1 and SQW-2, they show

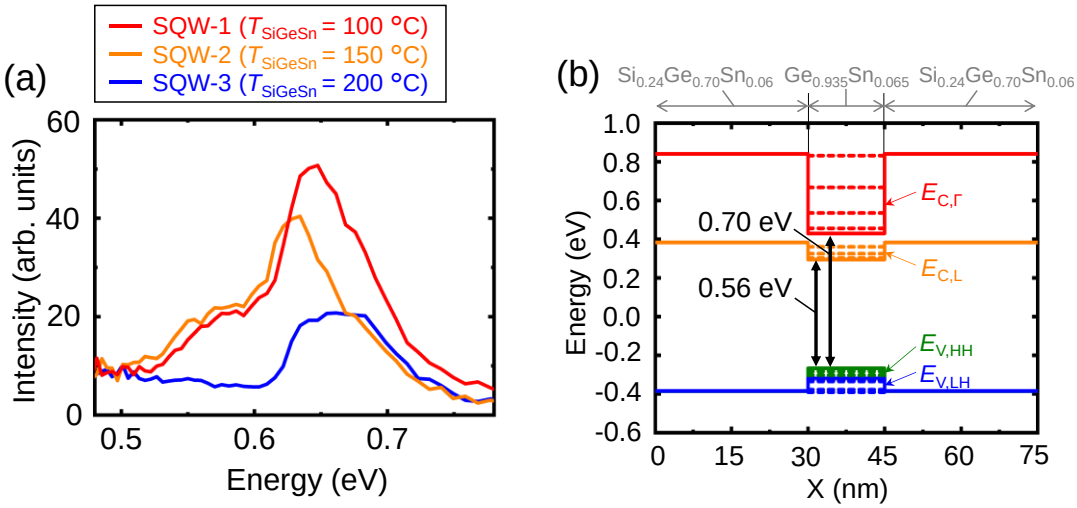

Figure 3.2 (a) PL spectra of the single-QW samples SQW-1, SQW-2, and SQW-3 with T_{SiGeSn} varied from 100–200 °C, (b) the theoretical calculation result of energy band alignment of $Si_{0.24}Ge_{0.70}Sn_{0.06}$(30 nm)/$Ge_{0.935}Sn_{0.065}$(15 nm)/$Si_{0.24}Ge_{0.70}Sn_{0.06}$(30 nm) structure.

the PL peaks around 0.57 and 0.65 eV, respectively. As for sample SQW-3, it shows a broadened PL peak with its center around 0.65 eV. In order to clarify the possible origins attributes to these PL peaks in each PL spectra, we conducted the theorical calculation of the energy band alignment for the designed $Ge_{0.935}Sn_{0.065}$/$Si_{0.24}Ge_{0.70}Sn_{0.06}$ single-QW structure. The calculation is based on model solid theory and is described in chapter 2.

Figure 3.2 (b) shows the calculated energy band alignment for the pseudomorphic grown $Si_{0.24}Ge_{0.70}Sn_{0.06}$ (30 nm)/$Ge_{0.935}Sn_{0.065}$ (15 nm)/$Si_{0.24}Ge_{0.70}Sn_{0.06}$ (30 nm) single-QW on Ge substrate. Parameters used for the calculation are extracted from Reference [43-45] in chapter 2. Energy band edges of the valence and conduction bands are depicted by solid lines in red, orange, green, and blue colors for $E_{C,\Gamma}$, $E_{C,L}$, $E_{V,HH}$, and $E_{V,LH}$, respectively. Also, the quantized energy levels of each energy band are denoted by dotted lines. Here, $E_{C,\Gamma}$ and $E_{C,L}$ are the conduction band edges for the Γ- and L-valleys, respectively, and $E_{V,HH}$ and $E_{V,LH}$ are the valence band edges for heavy and light holes, respectively. First of all, we confirmed that the type-I carrier confinement structure is formed as the energy bandgap of the $Ge_{0.935}Sn_{0.065}$ well is within that of the $Si_{0.24}Ge_{0.70}Sn_{0.06}$ barrier. According to the calculation result, the $Ge_{0.935}Sn_{0.065}$ well is an indirect bandgap semiconductor. The energy bandgap values of $Ge_{0.935}Sn_{0.065}$ from the conduction band edges at Γ- ($E_{C,\Gamma}$) and L-valleys ($E_{C,L}$) to the valence band edge ($E_{V,HH}$) were calculated to be 0.70 and 0.56 eV, respectively.

Based on this calculation result, we consider the peak components at 0.57 and 0.65 eV of the observed PL spectra in **Figure 3.1 (a)** are related to the indirect and direct optical transitions including their quantum levels of the $Ge_{0.935}Sn_{0.065}$ well layer. We also found that with the improvement of the crystallinity of the single-QW samples, the indirect transition related peak component (0.57 eV) are appeared and increased on the intensity.

Therefore, from the discussion in this section, we believe that a lower T_{SiGeSn} could benefit not only crystalline but also PL efficiency of the single-QW samples. With the understanding of this fact, we challenged the formation of $Ge_{1-x}Sn_x/Si_yGe_{1-x-y}Sn_x$ double-QW and examined the impact of low temperature growth on its crystallinity and PL performance in the next section.

3.3.2 Formation of low temperature grown $Ge_{1-x}Sn_x/Si_yGe_{1-x-y}Sn_x$ double-QWs and characterization of their crystalline and PL properties

In this section, we examined the formation of $Ge_{1-x}Sn_x/Si_yGe_{1-x-y}Sn_x$ double-QWs at low growth temperature and discussed the impact of growth temperature on its crystalline and PL properties. For the double-QWs growth, thickness of each $Ge_{1-x}Sn_x$ and $Si_yGe_{1-x-y}Sn_x$ layer is designed to be 15 nm, and the same growth temperature $T_{g,DQW}$ was used for the growth of $Ge_{1-x}Sn_x$ and $Si_yGe_{1-x-y}Sn_x$ layers, for the simplicity. Also, the Sn content of $Ge_{1-x}Sn_x$ was designed to be ~9%, as described in the experiment procedure section. In this study, two double-QWs samples are prepared, DQW-1 and DQW-2, where their growth temperature $T_{g,DQW}$ are 100 and 140 °C, respectively.

First, we will discuss the impact of $T_{g,DQW}$ on the crystallinity of double-QWs samples. **Figure 3.3** shows the XRD-2DRSM result of the prepared double-QWs samples; **(a)** DQW-1 and **(b)** DQW-2. In both XRD-2DRSM results, all the epitaxial diffraction peaks have the same Q_x value to the Ge peak, indicating that the $Ge_{1-x}Sn_x/Si_yGe_{1-x-y}Sn_x$ double-QWs structures of DQW-1 and DQW-2 were all pseudomorphically grown on Ge substrate. For sample DQW-1, we observed the separated $Ge_{1-x}Sn_x$ diffraction peak and

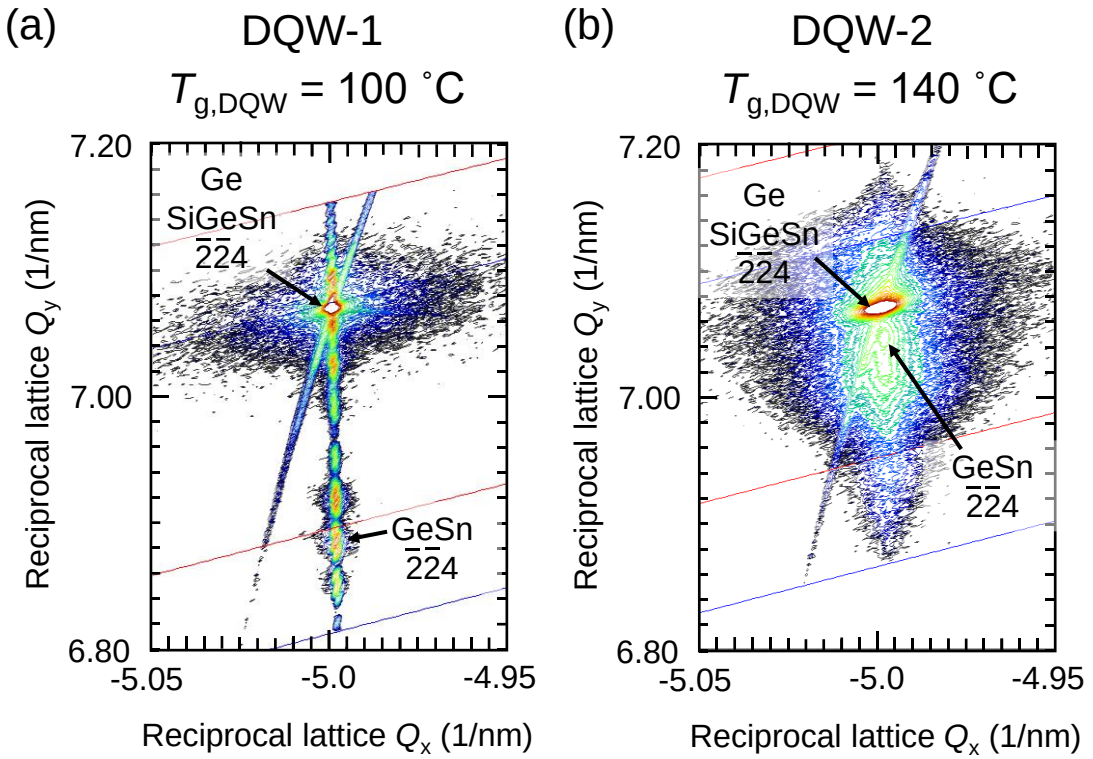

Figure 3.3 XRD-2DRSM measurement result of the double-QWs sample of (a) DQW-1 and (b) DQW-2.

the overlapped Ge and $Si_yGe_{1-x-y}Sn_x$ diffraction peaks, this is similar to the single-QW case. From the diffraction peak positions and the corresponding Raman result, the element contents of $Ge_{1-x}Sn_x$ and $Si_yGe_{1-x-y}Sn_x$ were estimated to be $Ge_{0.90}Sn_{0.10}$ and $Si_{0.25}Ge_{0.66}Sn_{0.09}$. This composition agrees well with our design. Since we also observed the thickness and super-lattice related fringes around the epitaxial diffraction peaks, the uniform and steep $Ge_{1-x}Sn_x$/$Si_yGe_{1-x-y}Sn_x$ interfaces should be also formed. Overall, this result suggests that the superior crystallinity double-QWs structure is formed in sample DQW-1 with the growth temperature $T_{g,DQW}$ of 100 °C.

On the other hand, for the sample DQW-2 as shown in **Figure 3.3(b)**, we observed the heavily broadened diffraction peaks related to Ge and $Ge_{1-x}Sn_x$ layers. The peak broadening around the Ge diffraction peak infers that the $Si_yGe_{1-x-y}Sn_x$ crystallinity is

degraded although the element contents in $Si_yGe_{1-x-y}Sn_x$ layers might be same as the designed values. In addition, from the $Ge_{1-x}Sn_x$ peak position, the Sn content in the $Ge_{1-x}Sn_x$ layers was estimated to approximately 1.5 %, which is much lower than the designed value. This result suggests that the Sn precipitation occurred in the $Ge_{1-x}Sn_x$ layers, resulting in the poor crystallinity of the DQW-2. Therefore, the growth temperature $T_{g,DQW}$ of 140 °C might by inappropriate for the epitaxial growth of high crystal quality $Ge_{1-x}Sn_x$/$Si_yGe_{1-x-y}Sn_x$ double-QWs structure.

Next, we investigated the surface morphology of the two double-QWs samples. **Figure 3.4** shows the AFM images of the double-QWs samples; **(a)** DQW-1 and **(b)** DQW-2. It can be seen that the sample DQW-1 has a flat surface with an RMS roughness at only 0.54 nm, and no evidence of Sn segregation or propagated threading dislocation has been observed. This suggests that the superior crystallinity of the 100 °C grown

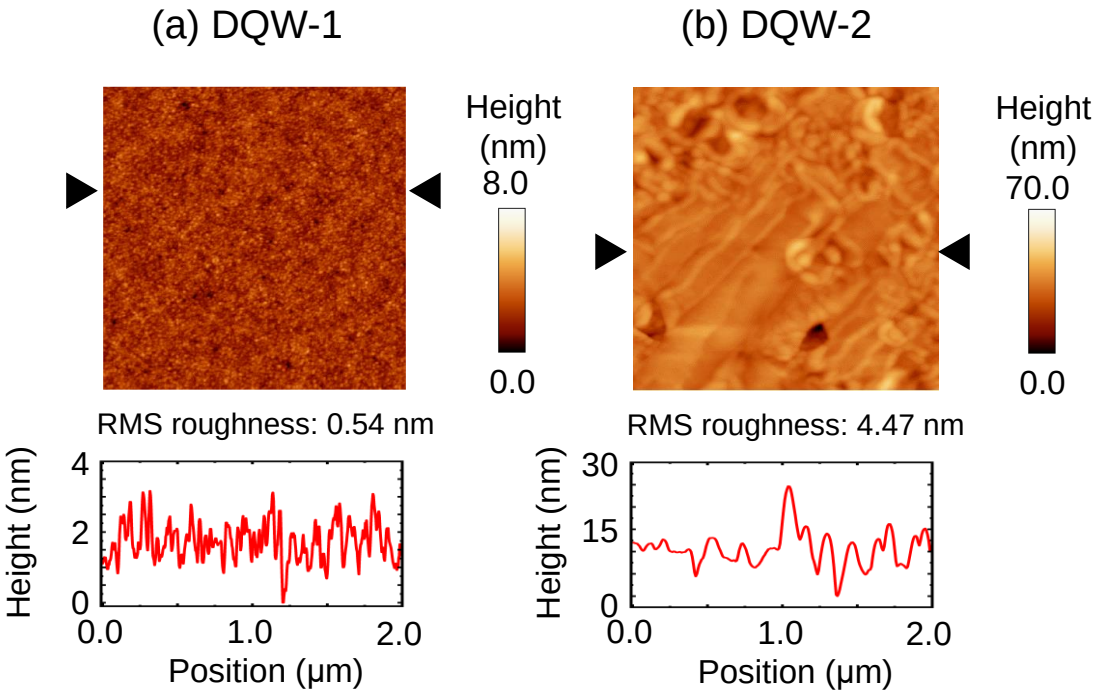

Figure 3.4 AFM image and line profiles for the double-QWs samples (a) DQW-1 and (b) DQW-2.

DQW-1 also provided it a substrate-comparable flat surface morphology. However, for the sample 140 °C grown DQW-2, surface roughening with RMS roughness at 4.47 nm, and numerous surface agglomerations has been observed. This surface morphology is similar to that of **Figure 3.1(f)**, suggesting that the Sn precipitation already occurred in the $Ge_{1-x}Sn_x$ layers, leading to the poor crystallinity. Regardless that the superior crystallinity was obtained for the single-QW samples at T_{SiGeSn} of 150 °C, this temperature is already high enough to cause the Sn precipitation during the growth of the $Ge_{1-x}Sn_x/Si_yGe_{1-x-y}Sn_x$ double-QWs. Therefore, for the growth of the $Ge_{1-x}Sn_x/Si_yGe_{1-x-y}Sn_x$ MQWs with superior crystallinity, the non-equilibrium growth condition to suppress the Sn precipitation is rather important than for the single-QWs. In that aim, the low temperature MBE growth is beneficial for realizing the $Ge_{1-x}Sn_x/Si_yGe_{1-x-y}Sn_x$ MQWs with superior crystallinity. Combining the observation from the XRD-2DRSM and AFM image results, we can conclude that the growth temperature $T_{g,DQW}$ of 100 °C is appropriate for the obtain of superior crystallinity double-QWs formation.

Moreover, to investigate more details of the uniformly grown and the steep interface formation of the double-QWs sample DQW-1 with $T_{g,DQW}$ of 100 °C, the interface structure was examined by the HAADF-STEM. The result is shown in **Figure 3.5**. The HAADF-STEM image reveals the clear contrast between the $Si_yGe_{1-x-y}Sn_x$ barrier layers and the $Ge_{1-x}Sn_x$ well layers by the dark and bright colors, respectively. We found that the smooth and abrupt interfaces between the barrier and well layers are formed. This is consistent with the XRD-2DRSM result. However, we also observed a slightly deviated thickness of the $Si_yGe_{1-x-y}Sn_x$ barrier layers (16 nm) and $Ge_{1-x}Sn_x$ well layers (12 nm) from the designed thickness (15 nm).

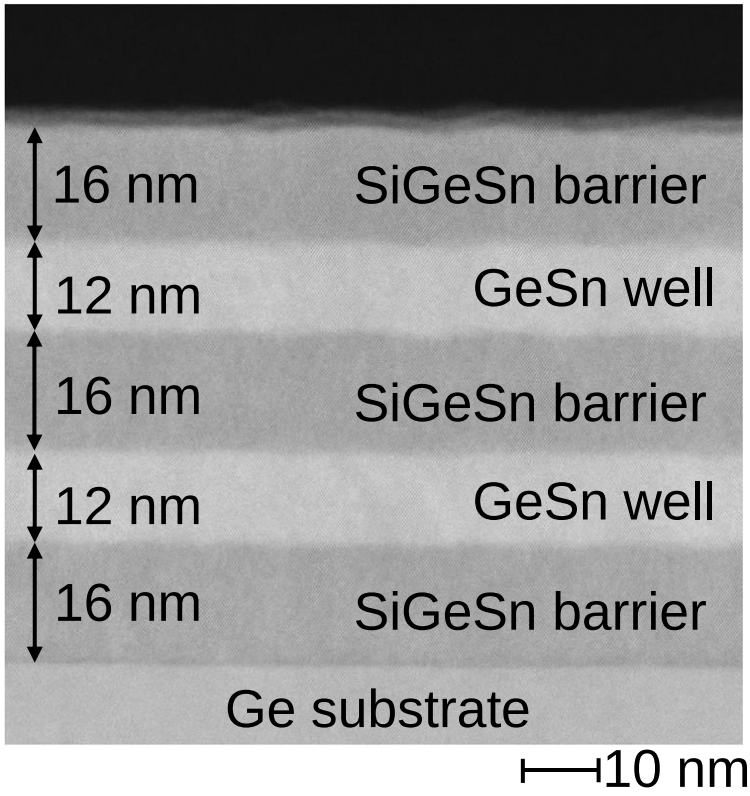

Figure 3.5 HAADF-STEM image of the double-QWs sample DQW-1.

We also performed the HR-RBS analysis to sample DQW-1 to investigate its element contents in each layer. The **Table 3.2** shows the average content ratio in each layer. In the analysis, we assumed that (1) Ge, Si, and Sn are uniformly distributed in each layer, and (2) the thicknesses of two $Ge_{1-x}Sn_x$ wells and three $Si_yGe_{1-x-y}Sn_x$ barriers are 12 nm and 16 nm, respectively, just as we observed from the HAADF-STEM image. We found that the Sn content in two $Ge_{1-x}Sn_x$ wells is the same at approximately 10 %. Although the contents of Ge, Si, and Sn in the three $Si_yGe_{1-x-y}Sn_x$ barriers are slightly different in each layer, the average values are approximately 66%, 26%, and 8%, respectively. These content values are well consistent with the estimated result from the XRD-2DRSM and Raman spectra, suggesting that the epitaxial growth of the desired double-QWs structure was achieved.

Table 3.1 Average content ratio in each layer of sample DQW-1estimated by HR-RBS.

	Contents in (Si)GeSn layers (%)		
	Ge	Si	Sn
Top Layer SiGeSn	64	28	8
GeSn	90	0	10
SiGeSn	67	25	9
GeSn	90	0	10
SiGeSn	69	25	7
Ge sub.	100	0	0

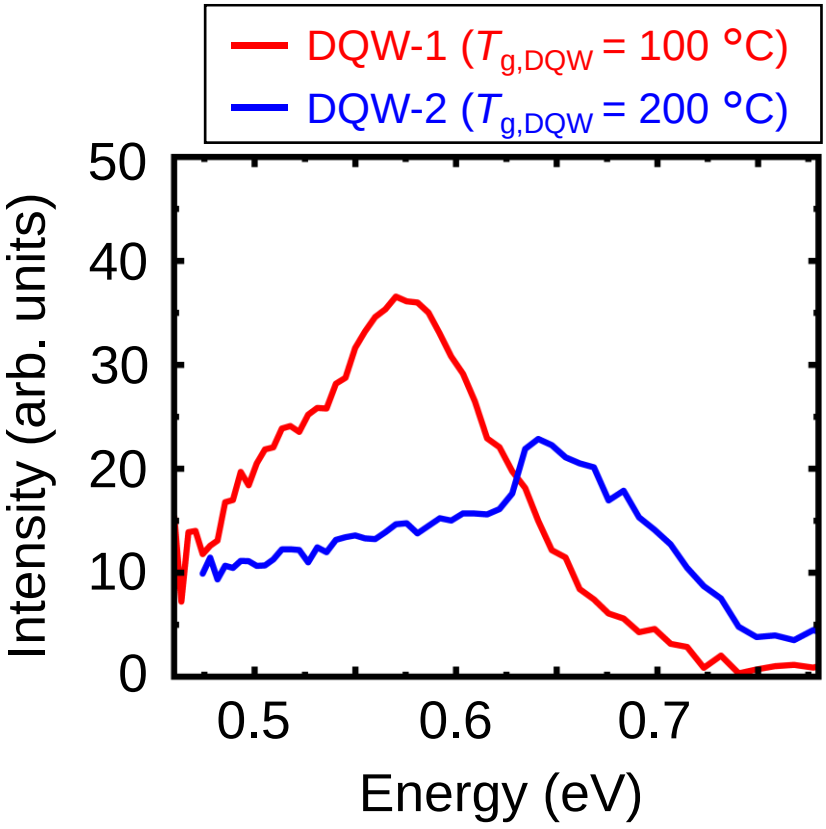

Figure 3.6 PL spectra of double-QWs samples DQW-1 and DQW-2 measured at RT.

Next, we discuss the luminescence properties of the double-QWs samples formed at different $T_{g,DQW}$. **Figure 3.6** shows the PL spectra measured at RT for DQW-1 and DQW-2 with $T_{g,DQW}$ of 100 and 140 °C, respectively. We observed the higher PL intensity for the sample DQW-1 than that of DQW-2. Just as our expectation, as DQW-1 has the better superior crystallinity. The PL spectra of DQW-1 showed two optical transition components in which the peak positions are around 0.51 and 0.57 eV, while the sample DQW-2 showed only one component having a peak around 0.66 eV. The difference 64energy position in the two samples PL spectra could be due to the Sn precipitation in DQW-2, in which caused the $Ge_{1-x}Sn_x$ well layers' composition change. To clarify these peak components, we examined the calculation of the energy band alignment for the double-QW samples.

Figures 3.7 (a) and **(b)** show the calculated energy band alignment for the double-QWs samples, DQW-1 and DQW-2, respectively. For sample DQW-1, the structure was assumed to be the $Si_{0.26}Ge_{0.66}Sn_{0.08}$(16 nm)/$Ge_{0.90}Sn_{0.10}$(12 nm)/$Si_{0.26}Ge_{0.66}Sn_{0.08}$(16 nm)

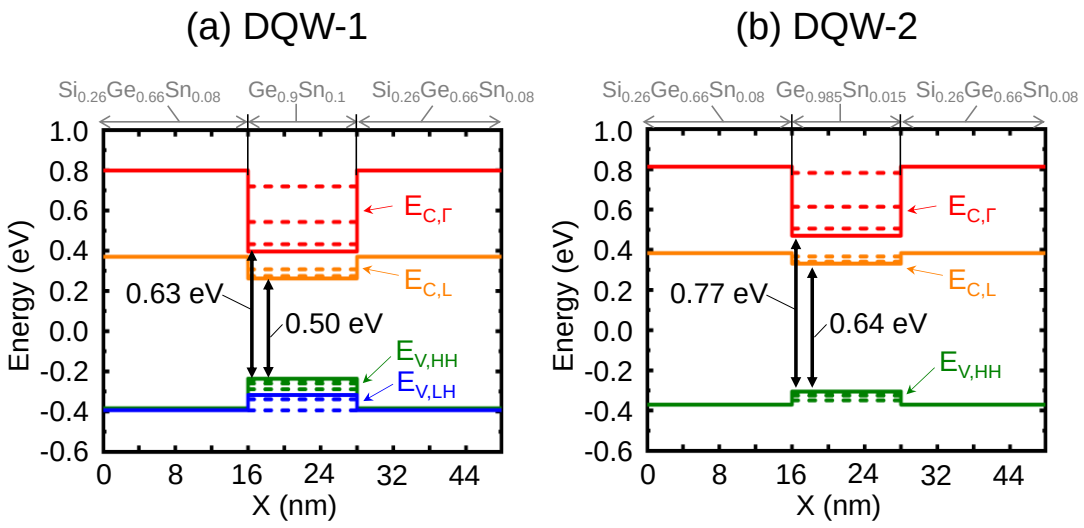

Figure 3.7 Calculation result of the energy band alignment for the double-QWs sample; (a) DQW-1 and (b) DQW-2.

heterostructure pseudomorphically grown on Ge substrate. As for sample DQW-2, the structure was similar to DQW-1 except the composition of $Ge_{1-x}Sn_x$ was assumed to be $Ge_{0.985}Sn_{0.015}$ from observation of its XRD-2DRSM result. In **Figure 3.7 (a)**, the energy bandgap values of the $Ge_{0.90}Sn_{0.10}$ in sample DQW-1 from $E_{C,L}$ and $E_{C,\Gamma}$ to $E_{V,HH}$ well were calculated to be 0.63 and 0.50 eV, respectively. Based on this calculation result, the peak components at 0.51 and 0.57 eV of the sample DQW-1 in **Figure 3.6** are possibly related to the indirect and direct optical transitions including their quantum levels of the $Ge_{0.90}Sn_{0.10}$ double well layers. On the other hand, for the sample DQW-2, the energy bandgap values of $Ge_{0.985}Sn_{0.015}$ from $E_{C,L}$ and $E_{C,\Gamma}$ to $E_{V,HH}$ were calculated to be 0.64 and 0.77 eV, respectively. Thus, the peak component around 0. 64 eV of the DQW-2's PL spectra in **Figure 3.6** would be the indirect transition of $Ge_{0.985}Sn_{0.015}$ well layers. For sample DQW-2, in addition to the crystallinity degradation, the carrier confinement would also become insufficient due to the large bandgap of $Ge_{0.985}Sn_{0.015}$ well compared to the $Ge_{0.9}Sn_{0.1}$ well in sample DQW-1. This also should cause the decreasing of sample DQW-2's PL intensity .

Therefore totally, in the case of the double-QWs structure, the even lower growth temperature $T_{g,DQW}$ of 100 °C is more beneficial for both crystalline and PL properties. It is also important to investigate that whether the $Ge_{1-x}Sn_x/Si_yGe_{1-x-y}Sn_x$ double-QWs grown at 100 °C can sustain the high temperature thermal treatment as the actual fabrication of semiconductor devices including inevitably annealing process. There're also reports referred that the appropriate PDA condition would benefit the crystal quality of the pseudomorphic $Ge_{1-x}Sn_x$ on Ge substrate as well as its PL efficiency,[5)] so the positive effect of PDA treatment on the double-QWs samples PL performance can be also expected. The detailed discussion will be carried out in the next section.

3.3.3 Impact of post deposition annealing treatment on the low-temperature grown $Ge_{1-x}Sn_x/Si_yGe_{1-x-y}Sn_x$ single- and double-quantum wells

In this section, we will discuss the impact of PDA on the crystallinity and PL properties of the $Ge_{1-x}Sn_x/Si_yGe_{1-x-y}Sn_x$ double-QWs. Main objective of this section is (1) to investigate that whether the PL performance of the double-QWs samples can be enhanced by the appropriate PDA recipe and (2) to examine the thermal stability of our double-QWs.

At the beginning, to investigate the PDA effect on the $Ge_{1-x}Sn_x/Si_yGe_{1-x-y}Sn_x$ heterostructure, we firstly conducted the rapid annealing on the as-grown single-QW sample SQW-1, because of the simple structure helps to understand the mechanism easier. The PDA treatment was carried out on both N_2 and H_2 atmosphere at 200-500 °C for 5 min. The PL spectra of sample SQW-1 subjected to treatment are shows in **Figure 3.8** for **(a)** N_2 atmosphere and **(b)** H_2 atmosphere. In both spectra, there is no significant change in the PL peak intensity and profiles after 200 and 300 °C PDA. However, after the 400 °C

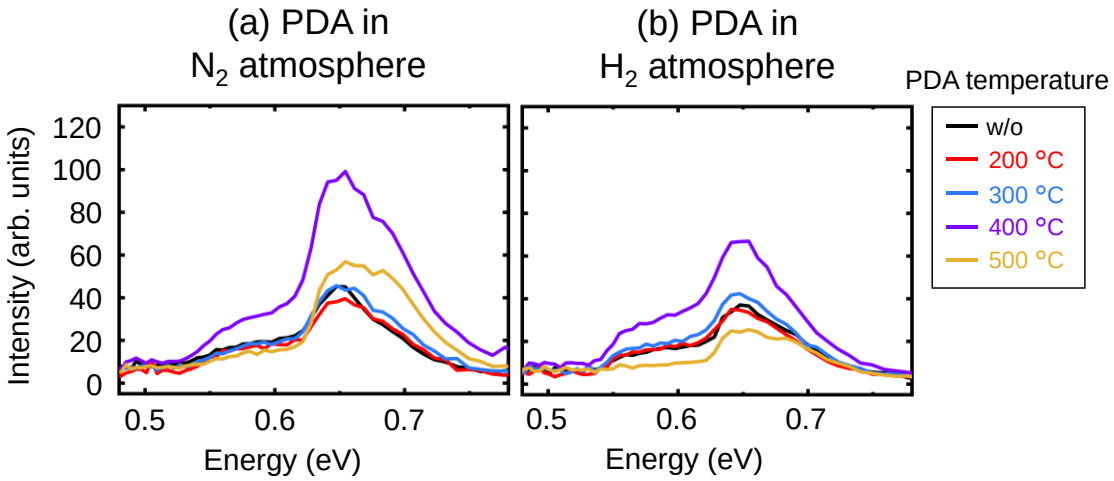

Figure 3.8 PL spectra of SQW-1 subjected to PDA treatment at 200-500 °C in (a) N_2 atmosphere and (b) H_2 atmosphere.

PDA treatment, both spectra show the great enhancement of the PL intensity on the. In the case of N_2 atmosphere annealing, the PL peak intensity at 0.65 eV are increased to the 220 % compared to that of the as-grown sample. While for the sample after H_2 atmosphere annealing, the PL intensity at 0.65 eV increased to the 180 % of the as-grown spectrum. Additionally, the increase on the peak component around 0.57 eV has also been observed. This suggests that despite the PDA atmosphere, the annealing under 400 °C can improve the PL efficiency originated from both direct (0.65 eV) and indirect (0.57 eV) optical transition of the $Ge_{1-x}Sn_x/Si_yGe_{1-x-y}Sn_x$ single-QW. On the other hand, for the samples subjected to the 500 °C PDA, the intensities of PL components located at 0.57 and 0.65 eV are both decreased, in the N_2 annealing condition, their intensities are slightly higher than the as-grown spectra, while those are even lower than the as-grown sample in the H_2 annealing condition. From this result, two conclusions can be extracted: (1) with the appropriate annealing temperature (400 °C), the PL efficiency of the $Ge_{1-x}Sn_x/Si_yGe_{1-x-y}Sn_x$ heterostructure can be enhanced, and (2) the N_2 atmosphere annealing is more beneficial in the enhancement effect of PL intensities compared to the H_2 atmosphere annealing. Based on these conclusions, we performed the thermal treatment for the 100 °C grown double-QWs sample DQW-1 against the PDA in N_2 atmosphere at 200-500 °C and discussed the impact of PDA on their crystalline and luminescence properties.

We first discuss the impact of PDA on the crystalline structure of the double-QWs sample. **Figure 3.9** shows the waterfall graph of the $2\theta/\omega$ XRD profiles around the 004 Ge reciprocal lattice point for sample DQW-1 not subjected to PDA and subjected to PDA in N_2 atmosphere at 200–500 °C. We can clearly observe the diffraction peaks corresponded to the Ge substrate and $Ge_{0.90}Sn_{0.10}$ layer as well as the neighbor fringes

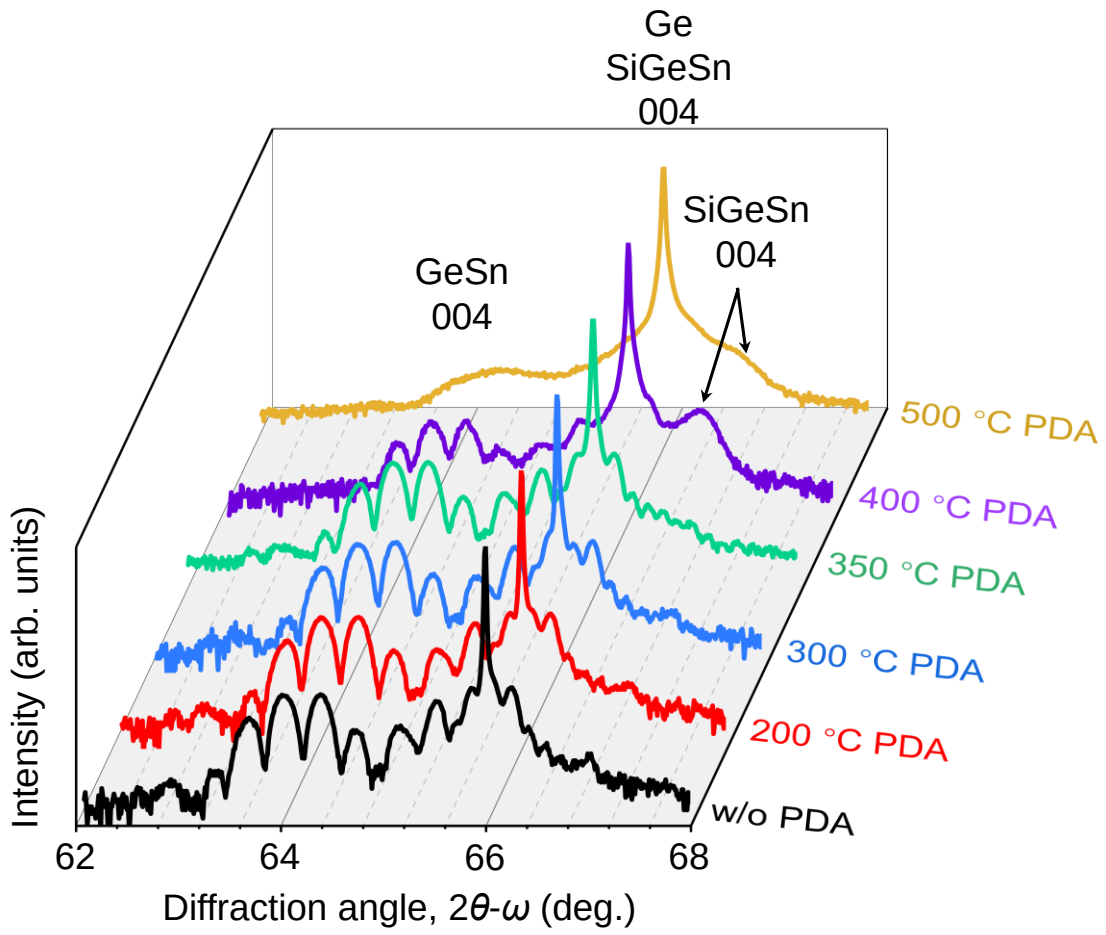

Figure 3.9 2θ-ω XRD profiles of double-QWs sample DQW-1 subjected to PDA from w/o to 500 °C around 004 Ge reciprocal lattice point.

from the profile of the sample not subjected to PDA. While the $Si_{0.26}Ge_{0.66}Sn_{0.08}$ layer is a lattice matched structure to Ge, and its diffraction peak is overlapped with Ge substrate. This observation is also consistent with the discussion of the XRD-2DRSM result in **Figure 3.3 (a)**. We found that the XRD 2θ/ω profiles for the DQW-1 samples subjected to PDA at 200, 300, and 350 °C share the same line profile with that of the sample not subjected to PDA. The agreement of these XRD profiles suggests that the crystalline structure of the $Ge_{1-x}Sn_x$/$Si_yGe_{1-x-y}Sn_x$ double-QWs even grown at 100 °C can be sustained after the 350 °C PDA.

On the other hand, the XRD $2\theta/\omega$ profile for the sample subjected to PDA at 400 °C showed the larger angular position of 2θ of the diffraction peak related to $Si_yGe_{1-x-y}Sn_x$ compared to that of Ge substrate. The separate of $Si_yGe_{1-x-y}Sn_x$ and Ge diffraction peaks indicates the reduction of the Sn content due to the Sn segregation from the as-grown $Si_{0.26}Ge_{0.66}Sn_{0.08}$ layer. On the contrary, the $Ge_{0.90}Sn_{0.10}$ peak and the neighbor fringes still exist although those intensities are slightly decreased, infaring that the steep and abrupt $Ge_{1-x}Sn_x/Si_yGe_{1-x-y}Sn_x$ interfaces are slightly degraded.

Furthermore, for the sample subjected to PDA at 500 °C, the position of $Ge_{0.90}Sn_{0.10}$ diffraction peak moves slightly to the larger angle direction compared to the samples subjected to PDA from w/o to 400 °C, while the neighboring fringes are all disappeared. This suggests the strain relaxation of the $Ge_{0.90}Sn_{0.10}$ layer with a possibility of Sn segregation. We investigated its XRD-2DRSM result (not shown in this paper), the Sn content and the degree of strain relaxation in the $Ge_{1-x}Sn_x$ layer were estimated to be 8.5 % and 2.7 %, respectively. According to some previous reports, thermal treatment to $Ge_{1-x}Sn_x$ causes the strain relaxation first, and then the Sn segregation.[6),7)] We predicted that our result is also the case with the previous reports.

Overall, the $Ge_{0.90}Sn_{0.10}$ and $Si_{0.26}Ge_{0.66}Sn_{0.08}$ layers of the double-QWs in this study show the good thermal stability against the 350 °C PDA. The crystalline degradation of $Si_{0.26}Ge_{0.66}Sn_{0.08}$ layers, caused by Sn segregation and strain relaxation occurred after 400 °C PDA, while the crystalline degradation of the $Ge_{0.90}Sn_{0.10}$ layers are observed after 500 °C PDA. Therefore, from the discussion of the PDA results on the crystal structure of the $Ge_{0.90}Sn_{0.10}/Si_{0.26}Ge_{0.66}Sn_{0.08}$ double-QWs structure, improving the thermal stability of the $Si_yGe_{1-x-y}Sn_x$ layers is an important mission to achieve the thermally robust $Ge_{1-x}Sn_x/Si_yGe_{1-x-y}Sn_x$ MQWs in the future work.

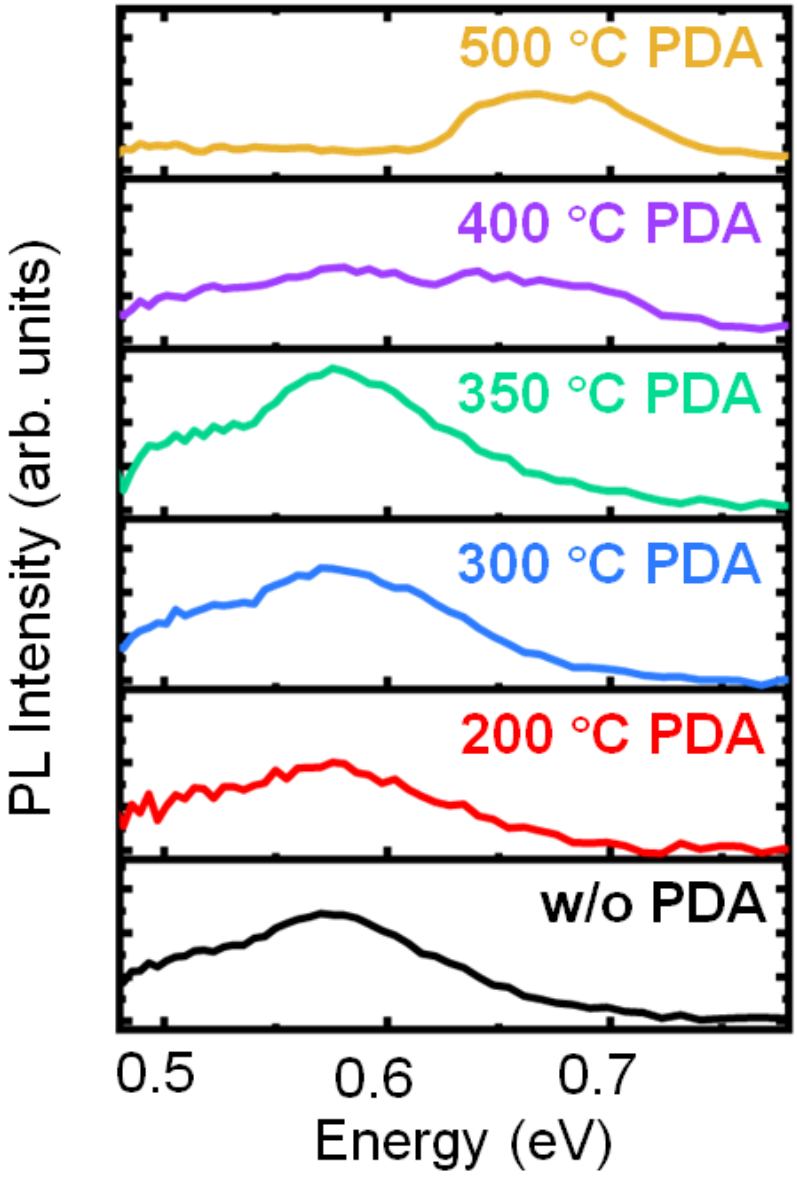

Figure 3.10 PL spectra of double-QWs sample DQW-1 subjected to PDA from w/o to 500 °C measured at RT.

Finally, we discuss the luminescence properties of the double-QWs sample, DQW-1 after the PDA treatment. **Figure 3.10** shows the PL spectra of DQW-1 not subjected to PDA and subjected to PDA in N_2 atmosphere at 200–500 °C. For the spectrum of the sample without PDA, two PL peak components including the major PL component around

0.57 eV and the minor PL component around 0.51 eV can be recognized, which is consistent with the former discussed PL profile in **Figure 3.6**. Here, the spectra of DQW-1 subjected to PDA at 200, 300, and 350 °C show the same PL components to those without PDA treatment while their peak intensities are different. Detail discussion of the PL peak intensities will be carried out in the latter part. For the samples subjected to the 400 and 500 °C PDA, the intensities of PL components located at 0.51 and 0.57 eV are decreased and absent. In contrast, a new PL component near 0.67 eV is observed. According to our discussion in **Figures 3.6 and 3.7(a)**, the 0.51 and 0.57 eV peak components are likely related to the indirect and direct optical transitions including the quantum levels of the $Ge_{0.90}Sn_{0.10}$ double well layers.

Next, to further discuss the origins and the reason for the absent and intensities change of the peak components, the deconvolution of the peak components are performed using the Voigt function. **Figures 3.11 (a)-(f)** show the deconvolution results for PL spectra of DQW-1 that are **(a)** without PDA, and subjected to PDA at **(b)** 200, **(c)** 300, **(d)** 350, **(d)** 400, and **(f)** 500 °C, respectively. Here, the raw PL data and the fitting result of each spectrum are shown by the black circle symbol and colored solid lines, respectively. The black solid line indicates the sum of the fitting curves. For the spectra of sample not subjected to PDA and the samples subjected to the 200, 300, and 350 °C PDA, three peak components can be deconvoluted, P1–P3 whose peak positions are 0.51, 0.57, and 0.61 eV, respectively. Considering the calculated energy band alignment result shown in **Figure 3.7(a)**, we concluded that P1, P2, and P3 are originated from the indirect transition of the bandgap, the indirect transition of the quantized energy levels, and the direct transition of the bandgap for the $Ge_{0.90}Sn_{0.10}$ well layer, respectively.

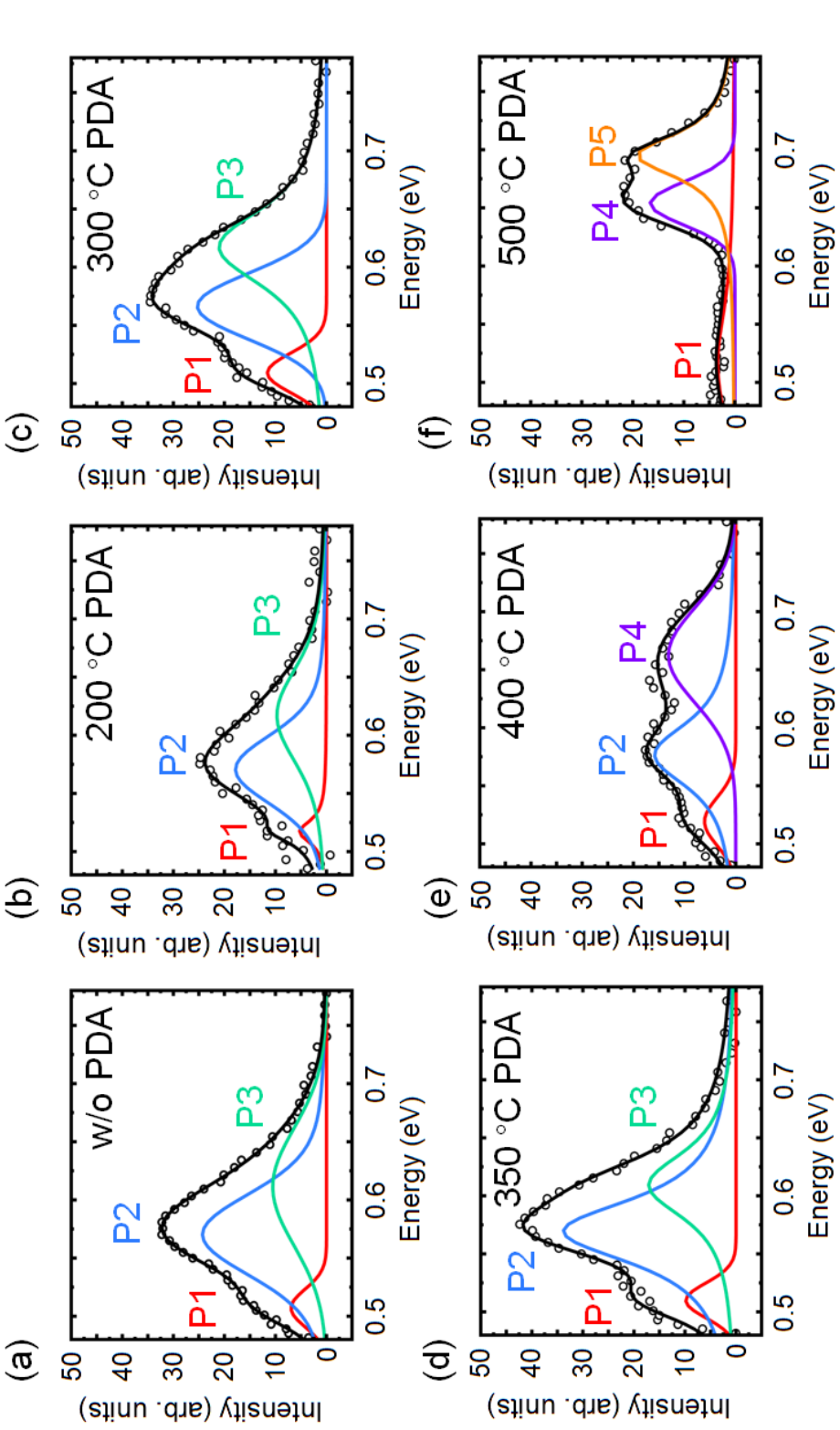

Figure 3.11 Deconvolution result of PL spectra of double-QWs sample DQW-1 subjected to PDA from w/o to 500 °C measured at RT; multiple peak components P1-P5 are deconvoluted from the raw PL spectra using voigt fitting.

As for the spectrum of the sample after 400 °C PDA, P1, P2, and P4 (0.66 eV) can be extracted as shown in **Figure 3.11 (d)**. And for the 500 °C PDA sample in **Figure 3.11 (f)**, the peak components P1, P4 and P5 (0.69 eV) are included. From the discussion result of the $2\theta/\omega$ XRD profiles of double-QWs sample DQW-1 (**Figure 3.9**), the high temperature PDA at 500 °C has caused the Sn segregation from the $Ge_{1-x}Sn_x$ and $Si_yGe_{1-x-y}Sn_x$ layers, resulting in the severe damage to the abrupt interfaces and crystalline quality of the $Ge_{1-x}Sn_x/Si_yGe_{1-x-y}Sn_x$ double-QWs structure. However, even considering the energy bandgap increase by the Sn content lowering, the peak origins of P4 and P5 cannot be well explained. For now, the peak origins of P4 and P5 have not been clarified yet, and further structural investigation is demanded to elucidate the peak origins. In the latter discussion, we will focus on the peak components of P1, P2, and P3 because these peaks origins are clarified.

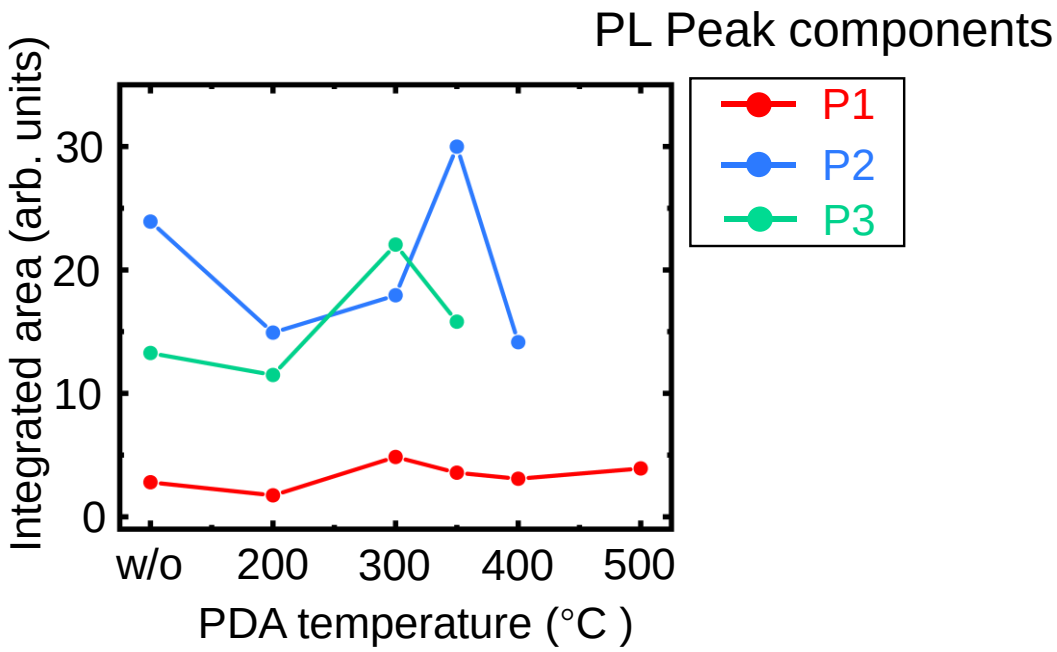

Figure 3.12 Integrated area intensity of the PL peak components P1-P3 as a function of PDA temperature.

Figure 3.12 shows the integrated area intensity of peak components P1, P2 and P3 as a function of the PDA temperature. There is no significant change in the area intensity of P1 against the PDA temperature observed. The area intensities of P2 and P3 are once decreased by the 200 °C PDA, and then increased. However, the area intensity of P2 increased until the PDA temperature of 350 °C, while that of P3 increased until 300 °C. The reason of the decrease of the area intensity by the 200 °C PDA has not been clarified yet, although the improvement of the PL intensity by PDA agrees with the other report.[5)] In this study, in our $Ge_{1-x}Sn_x$/$Si_yGe_{1-x-y}Sn_x$ double-QWs formation, the PDA temperature preferable to the PL intensity increase was around 350 °C, which could be mainly contributed by the area intensity increase of P2 at 350 °C. Moreover, we consider that the area intensity increase by the 300 °C and 350 °C PDA would be understood as the improvement of the crystallinity that hardly detected by XRD. According to the previous report,[8)] the strain relaxation and Sn segregation were observed from the pseudomorphic $Ge_{0.90}Sn_{0.10}$ layer after 350 and 400 °C annealing, respectively. Taking this fact into account, the slight move of Ge, Sn, and Si atoms in the $Ge_{1-x}Sn_x$ and $Si_yGe_{1-x-y}Sn_x$ layers should be possible around the 350~400 °C temperature range. As a result, some point defects which work as the non-radiative recombination center could be possibly decreased after the 350 °C PDA, leading to the increase of the PL intensity.

In total, after the discussion of the PDA impact on the crystalline and the PL efficiency of 100 °C grown $Ge_{1-x}Sn_x$/$Si_yGe_{1-x-y}Sn_x$ double-QWs. We found out that it has not only the thermal stability up to 350 °C, but also the potential for improving the PL performance by the PDA at an appropriate temperature where should be around 350 °C.

Considering the actual ULSI manufacture process, the further improvement of the thermal stability is still preferable. Currently, the bottleneck of the thermal stability lies

within the $Si_yGe_{1-x-y}Sn_x$ layer. Therefore, the engineering of the $Si_yGe_{1-x-y}Sn_x$ layer in terms of the thermal robustness in addition to the energy band alignment design will still the priority objective in the future works.

3.4 Summary

The impact of growth temperature on the crystalline and photoluminescence properties of the $Ge_{1-x}Sn_x$/$Si_yGe_{1-x-y}Sn_x$ single- and double-QWs formations has been examined. We found that lowering the growth temperature of the $Ge_{1-x}Sn_x$ and $Si_yGe_{1-x-y}Sn_x$ layers is beneficial to realize both $Ge_{1-x}Sn_x$/high-Si-content-$Si_yGe_{1-x-y}Sn_x$ single- and double-QWs with superior crystallinity. We also found that the PL efficiency of the single- and double-QWs structure can be enhanced by the crystallinity improvement.

Subsequently, we investigated the thermal stability as well as the PDA impact on the $Ge_{1-x}Sn_x$/high-Si-content-$Si_yGe_{1-x-y}Sn_x$ single- and double-QWs. We found that the PDA in N_2 atmosphere is more beneficial than in H_2 atmosphere for the PL efficiency increase in the case of the $Ge_{1-x}Sn_x$/$Si_yGe_{1-x-y}Sn_x$ single-QW structure. And we found that the appropriate PDA temperature at 400 and 350 °C can greatly improve both crystallinity and PL intensity of the $Ge_{1-x}Sn_x$/$Si_yGe_{1-x-y}Sn_x$ single- and double-QWs formation. However, PDA temperature over the appropriated value leads to the decrease of PL efficiency as well as the crystalline degradation due to Sn segregation in $Ge_{1-x}Sn_x$ and $Si_yGe_{1-x-y}Sn_x$ layers.

The research result from this chapter reveals that lowering the growth temperature of the $Ge_{1-x}Sn_x$/high-Si-content-$Si_yGe_{1-x-y}Sn_x$ single- and double-QWs formations in the using MBE epitaxial method is practically beneficial to achieve superior crystallinity and sufficient carrier confinement for the future optoelectronic device applications. The

appropriate thermal treatment can also play an important role to improve their light emission performance. Furthermore, since the overly high temperature PDA can easily cause the structural degradation in the high-Si-content-$Si_yGe_{1-x-y}Sn_x$ layer, the improvement of its thermal stability is an important perspective in the future works.

References

1) S. Zaima, O. Nakatsuka, N. Taoka, M. Kurosawa, W. Takeuchi and M. Sakashita, Sci. Technol. Adv. Mater. **16** (4), 043502 (2015).

2) M. Fukuda, D. Rainko, M. Sakashita, M. Kurosawa, D. Buca, O. Nakatsuka and S. Zaima, Semicond. Sci. Technol. **33** (12), 124018 (2018).

3) S. Zhang, S. Shibayama and O. Nakatsuka, Semicond. Sci. Technol. **38** (1), 015018 (2022).

4) J. Jeon, A. Suzuki, K. Takahashi, O. Nakatsuka and S. Zaima, Jpn. J. Appl. Phys. **57** (12), 121303 (2018).

5) G. Lin, K. Qian, H. Cai, H. Zhao, J. Xu, S. Chen, C. Li, R. Hickey, J. Kolodzey and Y. Zeng, J. Alloys and Compounds **915**, 165453 (2022).

6) H. Li, Y. X. Cui, K. Y. Wu, W. K. Tseng, H. H. Cheng and H. Chen, Appl. Phys. Lett. **102** (25), 251907 (2013).

7) H. Cai, K. Qian, Y. An, G. Lin, S. Wu, H. Ding, W. Huang, S. Chen, J. Wang and C. Li, J. Alloys and Compounds **904**, 164068 (2022).

8) L. Wang, Y. Zhang, Y. Wu, T. Liu, Y. Miao, L. Meng, Z. Jiang and H. Hu, IEEE Trans. Electron Dev. **67** (8), 3229 (2020).

Chapter 4 Formation and PL properties of pseudo-direct transition of heavily Sb doped n^+-$Ge_{1-x}Sn_x$ and the favorable heterostructure

4.1 Overview

As we discussed in the previous parts, to realize the RT operation $Ge_{1-x}Sn_x$ laser, the appropriate heterostructure with sufficient energy band offset and direct transition active layer are both critical. In chapter 3, we already demonstrated that the low temperature growth MBE technique and the appropriate PDA treatment play important roles to achieve the superior crystallinity of $Ge_{1-x}Sn_x$/high-Si-content-$Si_yGe_{1-x-y}Sn_x$ heterostructures for good light emission efficiency. However, due to the pseudomorphic growth condition, the $Ge_{1-x}Sn_x$ layer in chapter 3 is still in an indirect transition nature. Thus, we expect the direct transition $Ge_{1-x}Sn_x$ layer could provide more potential emission properties.

The direct transition method for $Ge_{1-x}Sn_x$ has been studied by many groups very recently.[1)–3)] To counteract the negative effect of compressive strain that enlarge the direct energy bandgap at the Γ-valley, either strain relaxation technique or high-Sn incorporation is required. In our research group, Fukuda has reported his efforts on the direct transition of $Ge_{1-x}Sn_x$ using strain-relaxation technique on an ion implanted substrate.[4)] He also demonstrated the photoluminescence performance of a heterostructure based on the high-Sn-content $Ge_{0.84}Sn_{0.16}$ active layer in his doctor thesis paper.[5)] However, according to these studies, either strain relaxation or high Sn incorporation will increase the crystal

defects densities in the $Ge_{1-x}Sn_x$ layer and cause structural degradation, which impede the radiative recombination and resulting in a reduced light emission efficiency. Therefore, the other technique that can provide direct energy bandgap transition and high crystal quality simultaneously is needed.

Recently, the pseudo-direct bandgap transition mechanism has been reported for the Ge.[6,7] The pseudo-direct bandgap is achieved by the heavy doping technique; the increased electron concentration will not only the indirect L-valley but also the direct Γ-valley in the conduction band. This makes the recombination of the electrons and holes located at the L-point possible without kinetic energy involving. **Figure 4.1** shows the concept and simplified energy band structure of pseudo-direct bandgap transition Ge. However, there're few reports on the psudo-direct bandgap transition $Ge_{1-x}Sn_x$, and the formation of heavy doped $Ge_{1-x}Sn_x$ and corresponded optical property is still unclear.

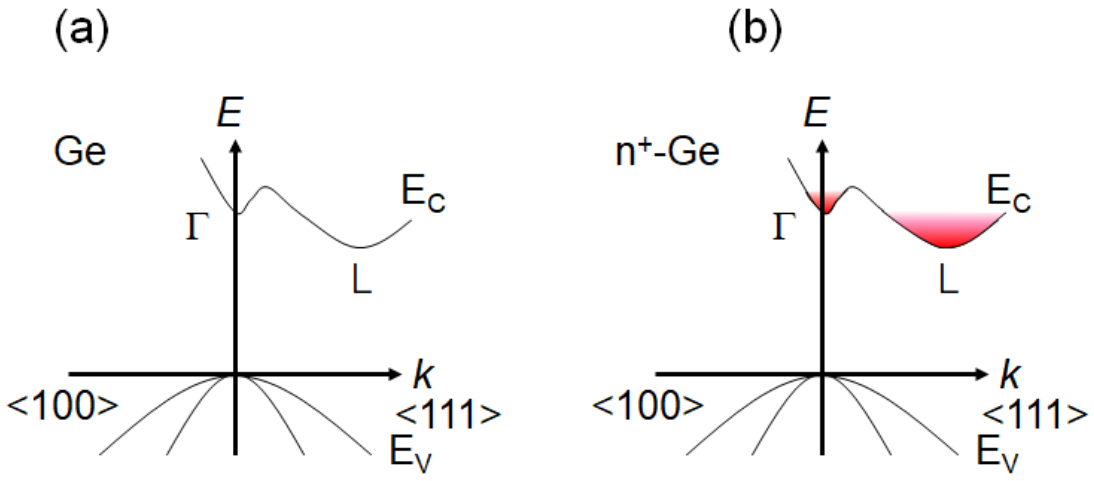

Figure 4.1 Concept of pseudo-direct transition mechanism; (a) intrinsic Ge and (b) heavily doped n^+-Ge.

In Nakatsuka's group, we have conducted related researchs on the MBE growth of Sb doped n^+-$Ge_{1-x}Sn_x$ in terms of its electrical property[8] and optical property.[5] We found that using MBE insitu doping techniquem, the n^+-$Ge_{1-x}Sn_x$ with doping concentration over 10^{20} cm^{-3} can be achived, which is higher than most doping limitation in the CVD method (~ 10^{19} cm^{-3}).[9,10] It is also found that even with such high doping concentration, the superior crystallinity n^+-$Ge_{1-x}Sn_x$ can be still obatined with the appropriate epitaxial growth condition. **Figure 4.2** shows a XRD-2DRSM result of a 80-nm-thick n^+-$Ge_{1-x}Sn_x$ layer (doping concentration: 1.18×10^{20} cm^{-3}) grown on a Ge (001) substrate. The two diffraction peaks related to the Ge substrate and n^+-$Ge_{1-x}Sn_x$ layers as well as the neighbor fringes are clearly observed, suggeting the superior crystallinity with the formation of uniform and steep interface.The n^+-$Ge_{1-x}Sn_x$ layer was estimated pseudomorpicaly grown

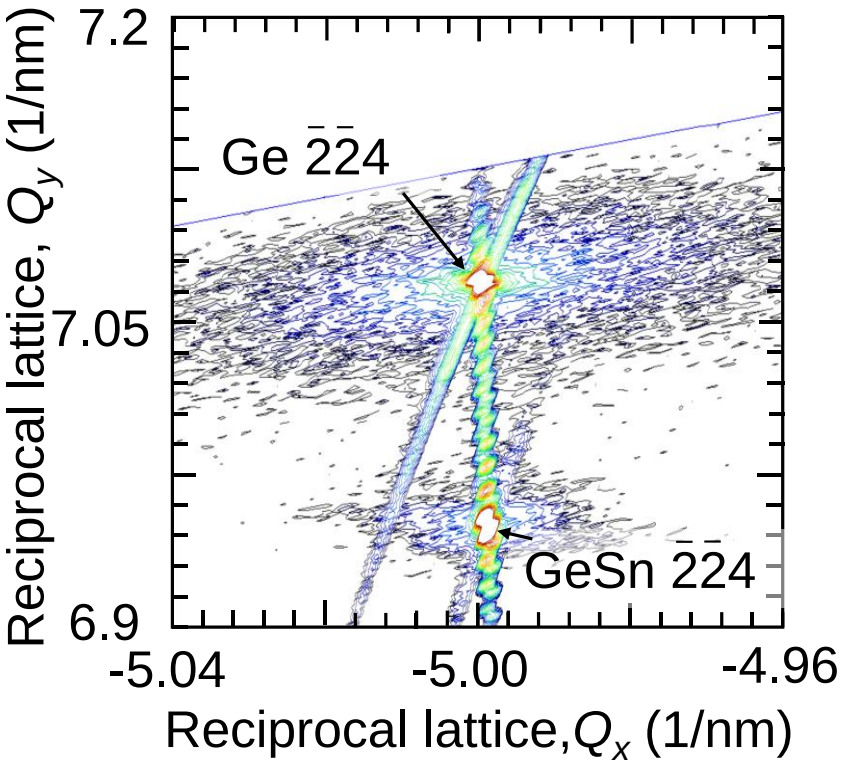

Figure 4.2 XRD-2DRSM result of heavily Sb doped n^+-$Ge_{1-x}Sn_x$ layer on Ge (001) substratre.

on the Ge with the substitutional Sn content around 6.5 % from the reciprocal space coordinates Q_x and Q_y. This result demonstrated that aehieving the excellent crystal quality heavy doping n^+-$Ge_{1-x}Sn_x$ layer is totally possible.

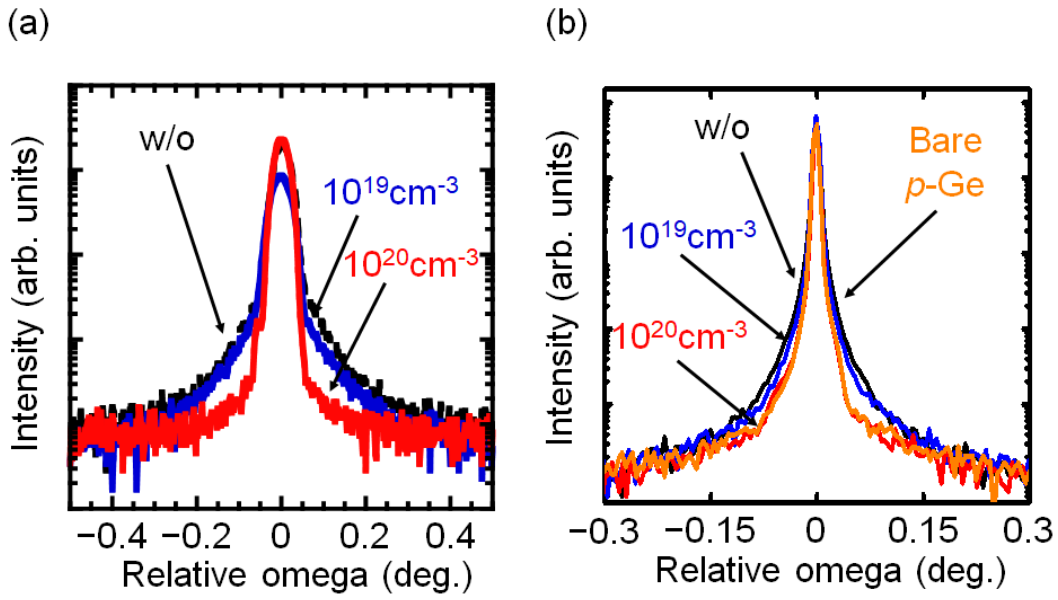

Figure 4.3 ω-rocking curves around 004 Bragg reflection of of (a) $Ge_{1-x}Sn_x$ and (b) Ge for the 100 nm n^+-$Ge_{1-x}Sn_x$ layer grown on Ge without doping and with electron concentrtaion of 10^{19} and 10^{20} cm^{-3}, respectively.

Moreover, because Sb has the surfactant effect in $Ge_{1-x}Sn_x$ matrix, the crystallinity improvement can be also expected by heavy Sb doping. Our previous report has studied the impact of Sb doping concentration on the crystallne of the $Ge_{1-x}Sn_x$ layer. **Figure 4.3 (a)** shows the $Ge_{1-x}Sn_x$ ω-rocking curves of 100 nm n^+-$Ge_{1-x}Sn_x$ layer grown on Ge without doping and with electron concentrtaion of 10^{19} and 10^{20} cm^{-3}, respectively. Sn content in all samples are around 6%. The tail broadening was observed for the the sample without doping and the sample with 10^{19} electron concentration, where as the broadening was greatly suppressed for the 10^{20} cm^{-3} doped sample. A prevous report has concluded that the tail broadening in the ω-rocking curve is usually due to the diffuse scattering

originating from point defects.[11] Therefore, this result suggests that the crystallinity of the $Ge_{1-x}Sn_x$ layer can be significantly improved by the heavy Sb doping over a carrier concentration of 10^{20} cm^{-3}. We consider that this improvement is manly due to the surfactant efect of Sb.[12]

In addition, similar investigation has been performed for the Ge substratre. the Ge ω-rocking curves in the 100 nm n^+-$Ge_{1-x}Sn_x$ layer samples without dopoing and with 10^{19} and 10^{20} cm^{-3} carrier concentrtaion are shown in **Figure 4.3 (b)**. The trail broadedning of the 10^{20} cm^{-3} doped sample was reduced to a level comparable to that of the bare Ge substrae. This result suggets that the diffuse scattering of Ge can be also suppressed by high Sb doping concentration, and the heavily doped Sb will provide high crystallinity not only in the $Ge_{1-x}Sn_x$ layer but also in the Ge substrate.

Carrying on with these knowledge, we move on to investigate the optical property of the heavy Sn doped n^+-$Ge_{1-x}Sn_x$ formation with superior crystallinity, the details of the its luminescence mechanism as well as a favorable heterostructure design for the n^+-$Ge_{1-x}Sn_x$ will be discussed in this chapter.

The part of the contents in this chaper includes some results and discussion on our previously publised paper.[13]

4.2 Experimental procedure

The samples are epitaxially grown on the well cleaned p-Ge (001) substrate, the cleaning of substrate and the epitaxial growth methods are described in **sections 2.11 and 2.12**. In this study, the in-situ Sb doped n^+-$Ge_{1-x}Sn_x$ single layer and heterostructures composed of n^+-$Ge_{1-x}Sn_x$ and n-Si_yGe_{1-y} layers are prepared. **Table 4.1** summarizes the characteristics of the prepared samples. The samples S1-S7 are the n^+-$Ge_{1-x}Sn_x$/p-Ge

structure, the samples SHS1-SHS4 and DHS1-DHS2 are the n^+-$Ge_{1-x}Sn_x$/n-Si_yGe_{1-y}/p-Ge and n-Si_yGe_{1-y}/n^+-$Ge_{1-x}Sn_x$/n-Si_yGe_{1-y}/p-Ge structures, respectively. The growth temperature of the n^+-$Ge_{1-x}Sn_x$ and layers n-Si_yGe_{1-y} ,T_{GeSn} and T_{SiGe} were 150 and 200-300 °C, respectively. Sn content in all n^+-$Ge_{1-x}Sn_x$ layers were designed to be 6%, while the Si content in layers n-Si_yGe_{1-y} are varied to control to control the energy band alignment offset.

The XRD and PL measurements used to characterize the crystallinity and optical properties of the samples are the same to the description in chapter 2. Notably, the power of 532 nm excitation laser used in the PL measurement was adjusted to 0.85 and 1.5 W for different PL spectra, the specific power number was identified for each PL spectra.

Table 4.1 Summary of sample structure, element contents, thickness, and growth temperatures of each layer in the prepared n^+-$Ge_{1-x}Sn_x$ single layer, the n^+-$Ge_{1-x}Sn_x$/n-Si_yGe_{1-y}/p-Ge SHSs and n-Si_yGe_{1-y}/n^+-$Ge_{1-x}Sn_x$/n-Si_yGe_{1-y}/p-Ge DHSs samples.

Sample ID	Sample structure	n^+-$Ge_{1-x}Sn_x$ layer					n-Si_yGe_{1-y} layer				
		Content (%)		Thickness (nm)	T_{GeSn} (°C)	Carrier concentration (cm^{-3})	Content (%)		Thickness (nm)	T_{SiGe} (°C)	Carrier concentration (cm^{-3})
		Sn	Ge				Si	Ge			
S1	n^+-$Ge_{1-x}Sn_x$/p-Ge	5.7	94.3	100	150	w/o					
S2		5.5	94.5			10^{18}					
S3		6.5	93.5			10^{19}					
S4		5.6	94.4			10^{20}					
S5		6.5	93.5	80	150	10^{20}					
S6		6.5	93.5	50							
S7		6.5	93.5	15							
SHS1	n^+-$Ge_{1-x}Sn_x$/n-Si_yGe_{1-y}	7.5	92.5	15	150	10^{20}	12	88	15	300	10^{18}
SHS2		7	93				18	82		250	
SHS3		6.5	93.5				23.5	76.5		250	
SHS4		6.5	93.5				27	73	30	300	
DHS1	n-Si_yGe_{1-y}/n^+-$Ge_{1-x}Sn_x$/ n-Si_yGe_{1-y}	6	94	15	150	10^{20}	20	80	15	250	10^{18}
DHS2		6.5	93.5				24.5	75.5		200	

4.3 Result and discussion

4.3.1 Impact of heavily Sb doping to the $Ge_{1-x}Sn_x$ on its crystallinity and optical properties

Firstly, we will discuss impact of Sb doping concentration on the optical property of the 100 nm n^+-$Ge_{1-x}Sn_x$ layer. Note that the **Figures 4.4 (a) and (b)** in this section are included in both Fukuda's doctor thesie and our previous journal paper.[5),13)]

Figure 4.4 (a) shows the PL spectra measured at RT for the 100 nm thick n^+-$Ge_{0.94}Sn_{0.06}$ layer without doping and with electron concentration of 10^{18}, 10^{19}, and 10^{20} cm^{-3} (corresponding to sample S1-S4, respectievly). For the sample S1 and S2, no PL peak was observed. On the other hand, for sample S3 with electron concentration of 10^{19} cm^{-3}, a single PL peak profile can be recongnized. With the increase of electron concentration from 10^{19} to 10^{20} cm^{-3}, a great improvement of the PL intensity has been

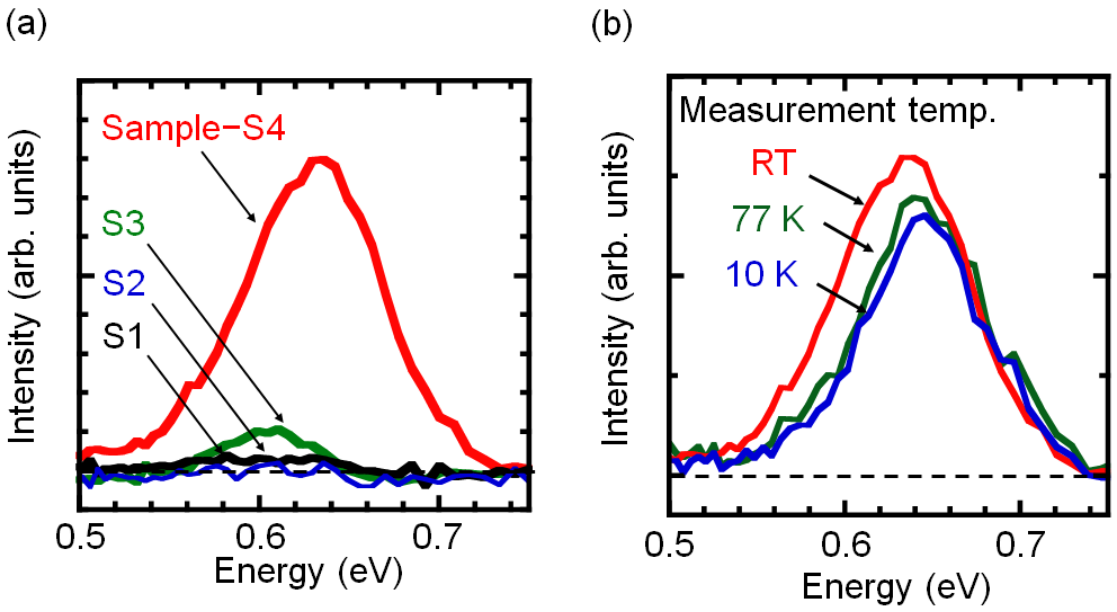

Figure 4.4 (a) PL spectra measured at RT for the 100 nm thick n^+-$Ge_{0.94}Sn_{0.06}$ layer without doping and with electron concentration of 10^{18}, 10^{19} and 10^{20} cm^{-3} (sample S1-S4, respectievly); (b) PL spectra of sample S4 measured at 10, 77 K and RT. Power of the excitation laser was 0.85 W.

observed for sample S4 (approximately seven times). This result infarring that heavy Sb doping, which contributing to the crystallinity improvement and electron population increase in $Ge_{1-x}Sn_x$, will lead to the enhancement of the luminescence efficiency.

Additionally, the PL peak position of 10^{20} cm^{-3} Sb doped n^+-$Ge_{0.94}Sn_{0.06}$ (sample S4) is located around 0.64 eV. According to our theoritical calculation result of energy bandgap for $Ge_{0.94}Sn_{0.06}$ in **Table 2.3**, where its energy bandgaps at L and Γ points are estimated to be 0.57 and 0.70 eV, respectively. The PL peak observed from the 10^{20} cm^{-3} Sb doped n^+-$Ge_{0.94}Sn_{0.06}$ is not consistent with the optical transition from conduction band edge to the valence band edge at either L- or Γ- valley. Since we cannot give conclusion of the n^+-$Ge_{0.94}Sn_{0.06}$'s PL peak origin from its PL spectra and theoretical calculation result. The temperature dependence of the PL intensity for sample S4 was measured for further investigation. The PL spectra of sample S4 measured at 10, 77 K and RT are shown in **Figure 4.4 (b)**. It can be seen that the PL peak intensity decreases with the reducing of the measurement temperature. This trend is a unique phenomenon of the direct transition process because the electron population contributing to the direct transition process will be reduced due to the carrier freeze-out effect at cryogenic temperature. Thus, the observation from **Figure 4.4 (b)** suggests that the PL peak of n^+-$Ge_{0.94}Sn_{0.06}$ is likely related to the radiative recombination process from the pseudo-direct bandgap transition. As for the reason of PL peak position shifted to the lower energy direction, a previous report has concluded that the band tailing effect can be caused by the heavy doping process, leads to the narrowing of the energy bandgap,[14] and we consider it might be the same case for the n^+-$Ge_{0.94}Sn_{0.06}$. However, the specific energy levels of the pseudo-direct bandgap transition have not been clarified, this will be the task in the future study.

After the discussion of the PL mechanism of the n^+-$Ge_{1-x}Sn_x$ single layer, we

conctinue to discuss the heterostructuer formation of based on the pseudo-direct bandgap n^+-$Ge_{1-x}Sn_x$. Since the heav y doping in $Ge_{1-x}Sn_x$ will arise its Fermi energy level, which requeires more effeort on the design for the sufficient-carrier-confinement heterostructure for the n^+-$Ge_{1-x}Sn_x$. To batain the guideline for the structual design, the thickness dependency on the PL property of n^+-$Ge_{1-x}Sn_x$ layer has been investigated. **Figrue 4.5 (a)** shows PL spectra of 15, 50 and 80-nm-thick n^+-$Ge_{0.94}Sn_{0.06}$ single layers on *p*-Ge (sample S5-S7, respectively), the carrier concentration for all samples are fixed at 10^{20} cm^{-3}. It can be clealy seen that the PL peak ientensity of the n^+-$Ge_{0.94}Sn_{0.06}$ layer decreased and absent after resuding its thickness from 80 nm to 15 nm. We considered three possible reasons that might cause the decrease of the PL intensity: (i) nonradiative recombination caused by point defects contained in the n^+-$Ge_{0.94}Sn_{0.06}$ layer, (ii) surface recombination at the

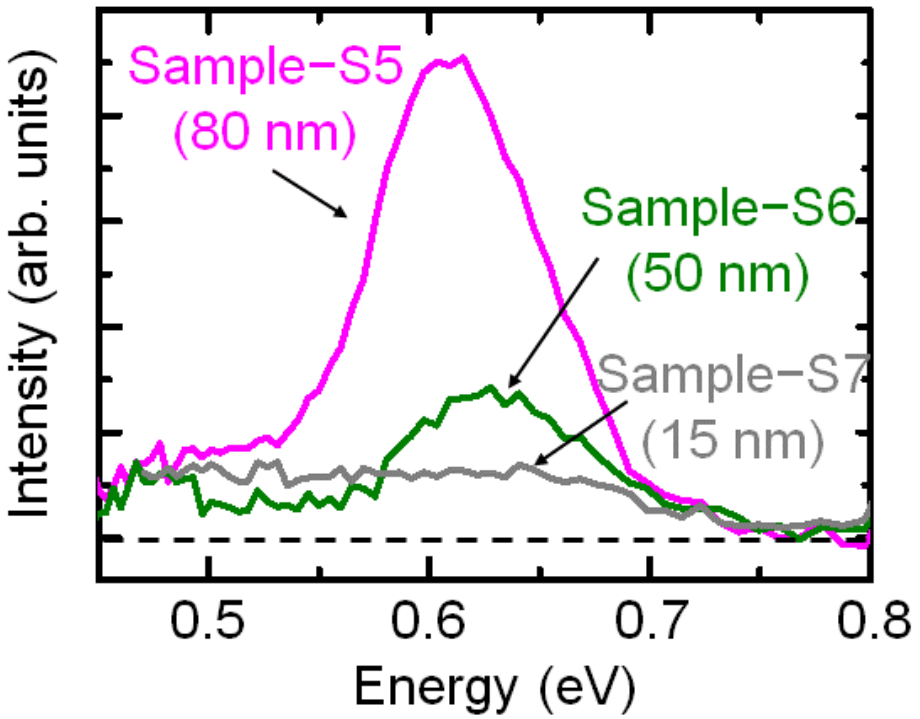

Figure 4.5 PL spectra measured at RT for the 15, 50 and 80 nm thick n^+-$Ge_{0.94}Sn_{0.06}$ single layer on *p*-Ge (sample S5-S7, respectively). Dashed line indicates the zero-level of PL intensity axis. Power of the excitation laser was 0.85 W.

surface region of the n^+-$Ge_{0.94}Sn_{0.06}$ layer and (iii) insufficient carrier confinement at the n^+-$Ge_{0.94}Sn_{0.06}$/p-Ge interface. Since the samples S5-S7 are prepared under the same growth condition, and we found no significant differences in their XRD measurement results (not shown), we though the point defect densities in samples S5-S7 were comparable to each other. Therefore, the possibility of reason (i) was rather low in this case. On the other hand, although we have no obvious evidence to directly role out the possibility of reason (ii), based on a previous report on the absorption coefficient of 532 nm laser in $Ge_{0.93}Sn_{0.07}$, where the the penetrtaion depeth was estimated to be 20 nm,[15] the behavior of carriers excited by the laser at the n^+-$Ge_{0.94}Sn_{0.06}$/p-Ge interface must have an impact on the radiative reconbination rate in the rather thinner sample S6 and S7 that reduced their PL efficiency. In this case, more discussion is required to analyze the possibility of reason (iii).

To better dunderstanding the energy band alignment of the n^+-$Ge_{0.94}Sn_{0.06}$/p-Ge interface, we performed the therotical calculation based on model solid approximation, calculation parameters are extraced from related reports.[16–19] Here, **Figure 4.6** shows the calculation result for the 15-nm-thick n^+-$Ge_{0.94}Sn_{0.06}$ on p-Ge structure. In the calculation, the carrier concentration of the n^+-$Ge_{0.94}Sn_{0.06}$ layer and p-Ge substratre was assumed to be 10^{20} and 10^{15} cm^{-3}, respectively. We also considered the energy band bending effect by the unmacted Fermi energy levels at two sides of the inerface.

According to this calculation result, the energy band offset for the condcution band at the L point ($\Delta E_{C,L}$) is approximately 0.05 eV. Although this offset value is not sufficient for the carrier confinement at the conduction band, the additional buit-in potential determined by the Fermi energy level differnces at the n^+-$Ge_{0.94}Sn_{0.06}$/p-Ge interface is

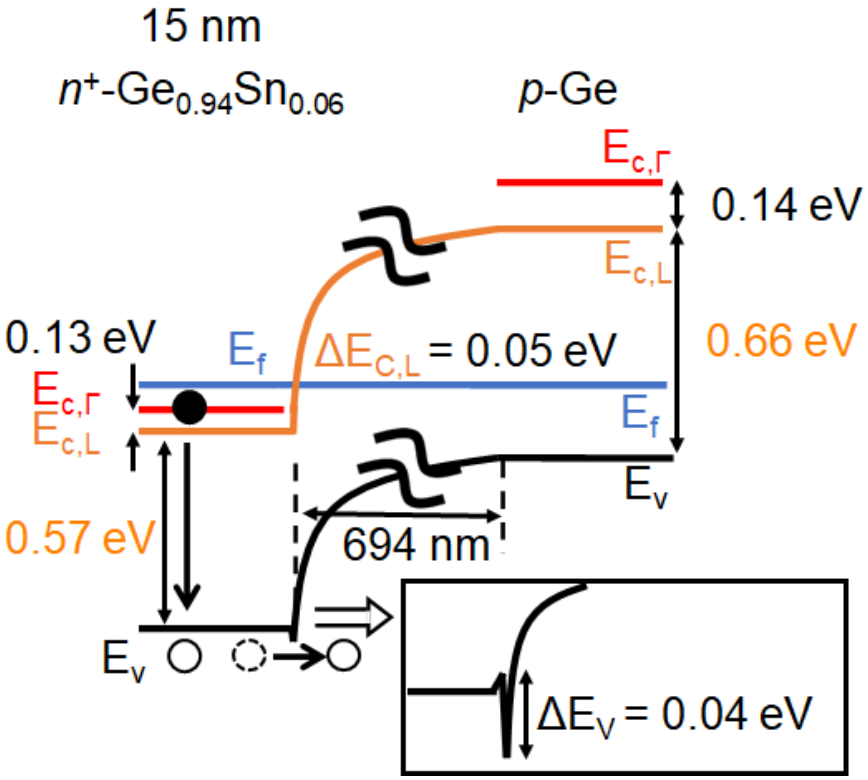

Figure 4.6 Energy band alignment for the 15-nm-thick n^+-$Ge_{0.94}Sn_{0.06}$/p-Ge structure.

large enough to bend the energy band alignment. This will prevent the excited electrons in the n^+-$Ge_{0.94}Sn_{0.06}$ layer from escaping into the Ge substreate, ensuring the carrier confinment effect at the conduction band. As for the valence band, the energy band offset (ΔE_V) is about 0.04 eV, consider that the energy band bending will furtherly arise the valence band egdde at the Ge side of the interface, the carrier confinemnt at the valence band is completely insufficient. As a result, the escape of holes from the n^+-$Ge_{0.94}Sn_{0.06}$ into Ge substrate cannot be ingnored, leading to the reduction of the radiative electron/hole-pair recommbination rate.

Therefore, it is necessary to design a favorable heterostructure wich can provide sufificient carrier confinement in both conduction and valence bands for elctrons and

holes. From this perspective, the increase of valence band offset, ΔE_V is a priory objective. In this term, we consider the n-Si_yGe_{1-y} is a promisng canditate for the clad layer for the n^+-$Ge_{1-x}Sn_x$ active layer based heterostructure.

4.3.2 Formation and luminescence properties of the n^+-$Ge_{1-x}Sn_x$/n-Si_yGe_{1-y} heterostructures

In this section, we will demonstrate the epitaxial growth of the n^+-$Ge_{1-x}Sn_x$/n-Si_yGe_{1-y} single heterostructure (SHS) and n-Si_yGe_{1-y}/n^+-$Ge_{1-x}Sn_x$/n-Si_yGe_{1-y} DHS with superior crystallinity and discuss their luminescence properties.

At first, all the prepared samples: SHS1-SHS4, DHS1 and DHS2 exhibited the superior crystallinity and flat surface morphology, verified by the in-situ RHEED observation, XRD-2DRSM and AFM measurements. To give an image of the crystal structure of these prepared samples, we take sample DHS1 as an example and its measurement results are shown in the **Figures 4.7 (a)-(c)**.((a) in-situ RHEED patterns of each layer after the epitaxial growth, (b) AFM image and corresponding line profiles, (c) XRD-2DRSM result around Ge $\overline{2}\overline{2}4$ reciprocal space point). Note that all samples that will be discussed in this section have the crystallinity and surface morphology that are comparable to the following discussed sample DHS1.

In the RHEED result, the streak diffraction pattern related to the 2×1 surface reconstruction structure of the Si_yGe_{1-y} surface was observed after the growth of the bottom n-Si_yGe_{1-y} layer, indicating that the epitaxial growth of the atomically flat surface n-Si_yGe_{1-y} layer on the Ge substrate was achieved. In addition, a spotted line pattern appeared after the growth of the n^+-$Ge_{1-x}Sn_x$ layer, and the 1/2-period streaky pattern were observed once again after growth of the upper n-Si_yGe_{1-y} layer, infaring that the same 2×1

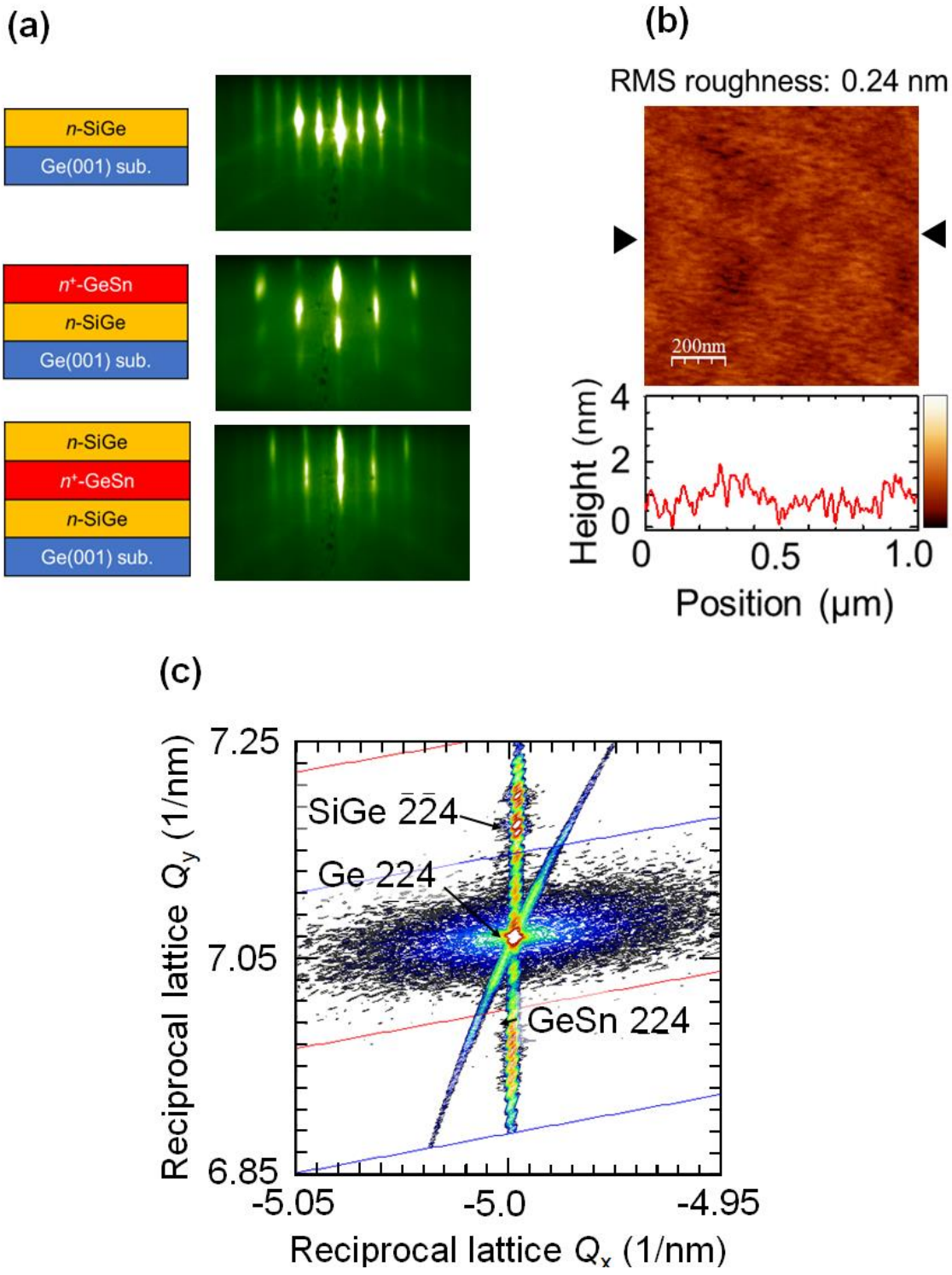

Figure 4.7 in-situ RHEED, AFM measurement, and XRD-2DRSM result of sample DHS1; (a) in-situ RHEED patterns of each layer after the epitaxial growth, (b) AFM image and corresponding line profiles, (c) XRD-2DRSM result around Ge $\overline{2}\overline{2}4$ reciprocal space point.

structure was also achieved in the upper n^+-$Ge_{1-x}Sn_x$ layer. The RHEED observation result suggests that the epitaxial growth of the n-Si_yGe_{1-y}/n^+-$Ge_{1-x}Sn_x$/n-Si_yGe_{1-y} DHS structure was successfully achieved with a flat surface morphology. This is also consistent with the AFM measurement result as shown in **Figure 4.7 (b)**. The root mean square (RMS) roughness of sample was estimated to be as well as 0.24 nm, which is even comparable to the bare Ge substrate.

According to the XRD-2DRSM result shown in **Figure 4.7(c)**, three diffraction peaks related to the n-Si_yGe_{1-y}, Ge substrate and n^+-$Ge_{1-x}Sn_x$ layer with the same reciprocal space coordinate Q_x can be observed. This means that the n-Si_yGe_{1-y} and the n^+-$Ge_{1-x}Sn_x$ layers are pseudomorphically grown on the Ge (001) substrate. Since the diffraction peaks related to both n-Si_yGe_{1-y} the n^+-$Ge_{1-x}Sn_x$ have the sharp shapes and high intensities despite that the thickness of only 15 nm for each layer, we expect the superior crystallinity for the epitaxial grown n-Si_yGe_{1-y}/n^+-$Ge_{1-x}Sn_x$/n-Si_yGe_{1-y} DHS structure. In addition, the contents of the n-Si_yGe_{1-y} and the n^+-$Ge_{1-x}Sn_x$ layers were estimated from their coordinates Q_x and Q_y assuming the Vegrad's law, and for sample DHS1 in the **Figure 4.7(c)**, the n-$Si_{0.8}Ge_{0.2}$/n^+-$Ge_{0.94}Sn_{0.06}$/n-$Si_{0.80}Ge_{0.20}$ structure was determined. We also observed the thickness fringes around the $Ge_{0.94}Sn_{0.06}$ and $Si_{0.8}Ge_{0.2}$ diffraction peaks, indicating the uniform and abrupt interfaces were also formed in the DHS structure.

To determine the thickness of each layer in sample DHS1, we performed XRD line profile simulation for DHS-1 structure. **Figure 4.8 (a)** shows the projection and simulation profile of the XRD-2DRSM measurement result in the reciprocal lattice Q_y direction for sample DHS1. The blue line profile is the measurement result, and the red line is the simulation result (PANalytical, Epitaxy and Smoothfit Ver. 4.3a). In the measurement result profile, all diffraction peaks related to $Ge_{1-x}Sn_x$, Si_yGe_{1-y} layers, and

p-Ge substrate are clearly observed, and a period of thickness fringes around the Si_yGe_{1-y} diffraction peak are also observed. In addition, two adjacent peaks can be seen around the diffraction peak of the Si_yGe_{1-y} layer, which might be the super lattice reflection. To determine the structure of sample DHS1 (including content and thickness), we plotted a simulation profile of the assumed double heterostructure shows in **Figure 4.8 (b)** and compared it with the measurement result. The diffraction peaks related to $Ge_{1-x}Sn_x$, Si_yGe_{1-y} layer and *p*-Ge substrate in the simulation result are located at the angular position close to the measurement result. Moreover, a period of thickness fringes around the Si_yGe_{1-y} diffraction peak were also observed. Since the number and angular position of these thickness fringes fitted well to the original measurement result, we then estimated the thickness of each layer of sample DHS1 to be approximately 15~16 nm, which agrees well with the designed thickness in this study.

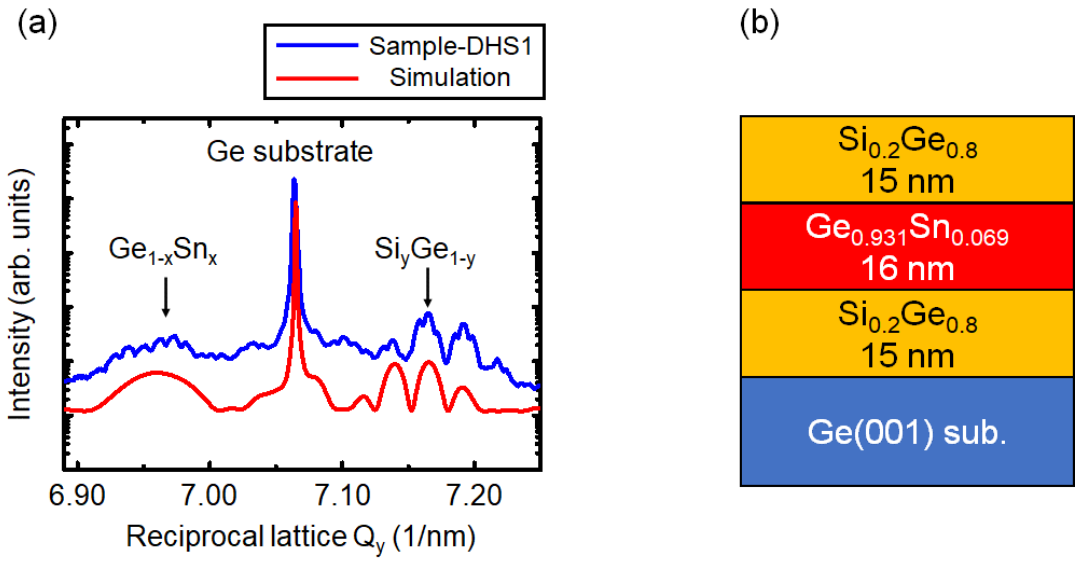

Figure 4.8 (a) Projection and simulation result of the XRD-2DRSM result in the direction for sample DHS-1. (b) Schematic diagram of the cross-section sample structure used to construct the simulation result.

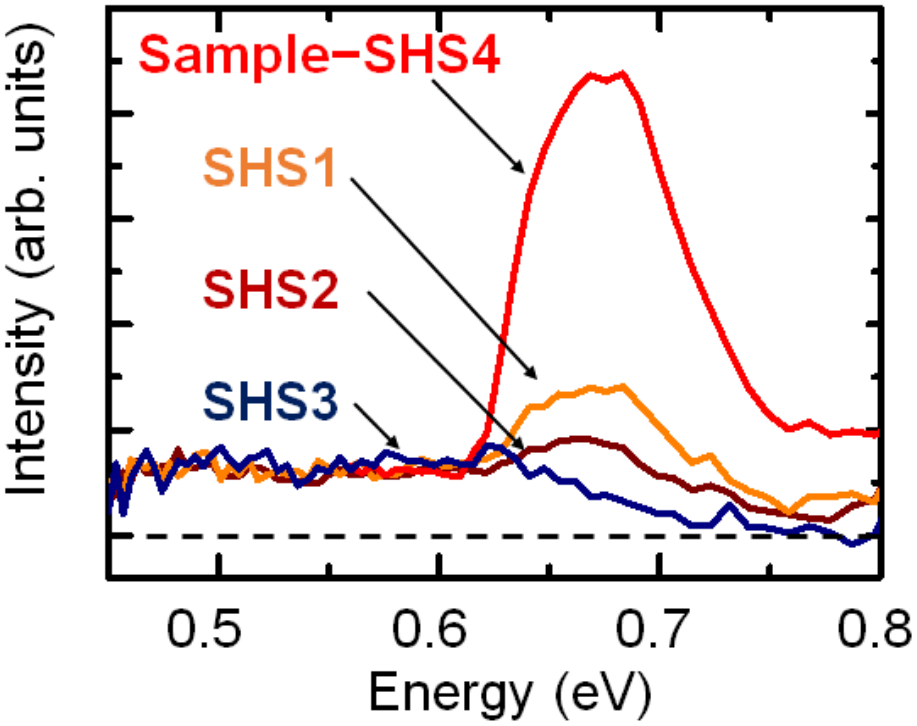

Figure 4.9 PL spectra of SHS1-SHS4 measured at RT. Dashed line indicates the zero-level of PL intensity axis. Power of the excitation laser was 0.85 W.

Next, we will discuss the PL properties of samples SHS1-SHS4, DHS1, and DHS2. **Figure 4.9** shows the PL spectra of the n^+-$Ge_{1-x}Sn_x$/n-Si_yGe_{1-y} SHS samples SHS1-SHS4 measured at RT. The Sn contents in all the n^+-$Ge_{1-x}Sn_x$ layers were designed and fixed at 6% for all samples and the Si contents in the n-Si_yGe_{1-y} layers varied from 12% to 27%. The corresponding valence band offset ΔE_V in sample SHS1 to SHS4 are 100, 130, 150 and 170 meV, respectively. From the PL spectra we can observe the PL peak for sample SHS3 and SHS4, which have the ΔE_V of 150 and 170 meV, respectively. Here, sample SHS4 exhibits the highest PL peak intensity in contrast to the lower PL peak intensity of sample SHS1 to SHS3. The increase of PL peak intensity in SHS4 is considered by the contribution of its high energy offset ΔE_V at 170 meV, which leads to the sufficient confinement for the holes in the valence band of the n^+-$Ge_{1-x}Sn_x$ active layer. Moreover,

the peak position of SHS4 was approximately located at 0.67 eV, which shifted toward the higher energy side compared to sample S4. Although we think the PL peak of the n^+-$Ge_{1-x}Sn_x$ layer might be originated from the radiative transition from the direct Γ-valley, the reason why it shifted to upon the insertion of n-Si_yGe_{1-y} layer is not understood yet.

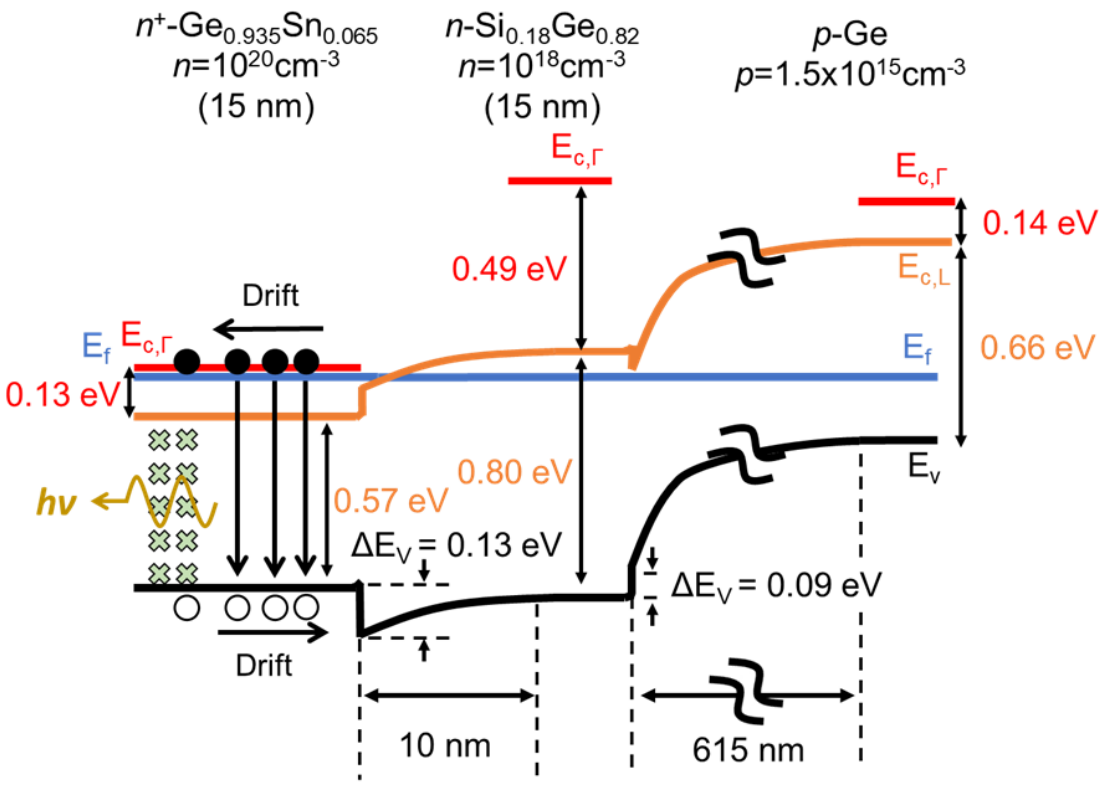

Figure 4.10 Energy band alignment for the n^+-$Ge_{0.935}Sn_{0.065}$/n-$Si_{0.18}Ge_{0.82}$/p-Ge structure.

In addition, the PL peak of sample SHS2 and SHS3 was weakened and absent comparing to the more stronger PL peak intensity of SHS1, regardless of the higher ΔE_V value of SHS2 and SHS3 than SHS1. The detail discussion will be carried out upon the energy band alignment of SHS2, as shown in **Figure 4.10**. First of all, the carriers in the conduction band at the n^+-$Ge_{0.935}Sn_{0.065}$/n-$Si_{0.18}Ge_{0.82}$ interface are drifted toward the n^+-$Ge_{0.935}Sn_{0.065}$ side by an electrical field generated by the built-in potential, just as the same in **Figure 4.6**. This mechanism will prevent electrons from escaping and ensuring the

sufficient confinement at the conduction band. For the valence band, although the electrical field will drift the holes toward the n-$Si_{0.18}Ge_{0.82}$ side, the valence band offset ΔE_V will stop the holes from passing through the interface. As a result, the carrier confinement for both electrons and holes are sufficient for the n^+-$Ge_{0.935}Sn_{0.065}$ active layer, thanks to the formation of n^+-$Ge_{0.935}Sn_{0.065}$/n-$Si_{0.18}Ge_{0.82}$ interface. The reason why SHS1 exhibits a higher PL peak intensity than those of SHS2 and SHS3 was attribution to the unintentionally controlled surface recombination, that the radiative recombination efficiency in SHS2 and SHS3 were possibly decreased by the surface defects. Therefore, we continue to investigate the DHS formation with ΔE_V around 150 meV and discuss their PL properties.

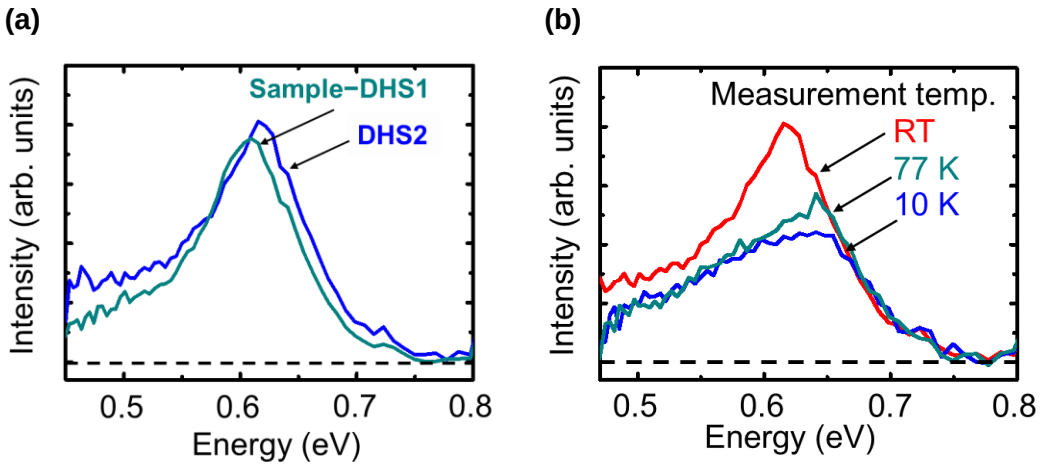

Figure 4.11 (a) PL spectra of DHS1 and DHS2 measured at RT. (b) PL spectra of DHS1 measured for various temperature. Power of the excitation laser was 0.85 W.

Figure 4.11(a) shows the PL spectra of two n^+-$Ge_{1-x}Sn_x$/n-Si_yGe_{1-y} DHS samples measured at RT. The Si contents in the clad n-Si_yGe_{1-y} layers for sample DHS1 and DHS2 are 20.0% and 24.5%, which corresponding to the ΔE_V values of 140 and 160 meV, respectively. Both DHS1 and DHS2 exhibited clear single PL peak with the comparable intensity at the peak position of approximately 0.6 eV. We furtherly investigated the

temperature dependence of the PL spectrum for sample DHS1, the result is shown in **Figure 4.11 (b)**. The decrease of the PL intensity with the reducing of temperature was observed, indicating that the n^+-$Ge_{1-x}Sn_x$/n-Si_yGe_{1-y} DHS sample has the direct-transition nature, and the PL peak should be originated from the pseudo-direct bandgap transition. In addition, we also observed the PL peak shift toward the higher energy side upon the increase of ΔE_V in **Figure 4.11 (a)**, the peak shift should be qualitatively understood as the shift of quantized level at the valence band side toward a deeper position with an increasing potential barrier corresponding to ΔE_V.

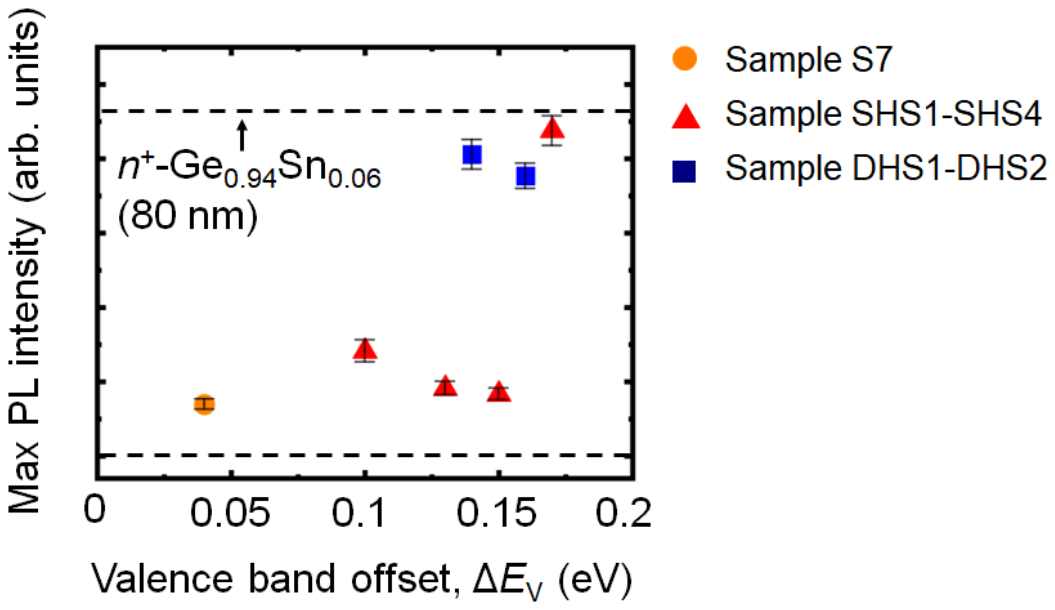

Figure 4.12 Summary of max PL intensities of the n^+-$Ge_{1-x}Sn_x$ layer as a function of ΔE_V, for sample S7, SHS1-SH4 and DHS1-DHS2.

Next, we will summarize the max intensities of the PL peaks for samples S7, SHS1-SHS4, and DHS-DHS2 as a function of the valence band offset ΔE_V, as shown in **Figure 4.12**. The orange circle, red triangle, and blue square symbols corresponding to sample S7, SHS samples SHS1-SH4 and DHS samples DHS1 and DHS2, respectively. The upper dashed line indicates the max PL intensity for the 80-nm-thick n^+-$Ge_{0.94}Sn_{0.06}$ layer

(sample S5). Notably, the results of the SHS samples (S7, SHS1-SH4) suggests that the formation of n^+-$Ge_{1-x}Sn_x$/n-Si_yGe_{1-y} interface could provide the sufficient energy band offset for the carrier confinement, which is an important design factor for the PL efficiency enhancement of the pseudo direct bandgap n^+-$Ge_{1-x}Sn_x$ layer. However, the surface recombination will reduce the emission efficiency of the surface n^+-$Ge_{1-x}Sn_x$ layer in the single-heterostructure formation. On the other hand, it is obvious that the max PL intensities of the 15-nm-thick n^+-$Ge_{0.94}Sn_{0.06}$ layer in the two DHS samples DHS1 and DHS2 are increased and comparable to that of sample S5, regardless of their equivalent ΔE_V with SHS2 and SHS3. Combining the discussion before, this result suggests that the DHS formation is beneficial for the improvement of the PL efficiency for the thin n^+-$Ge_{0.94}Sn_{0.06}$ layer in terms of carrier confinement and surface passivation.

At last, we have also investigated the PDA impact on the n^+-$Ge_{1-x}Sn_x$/n-Si_yGe_{1-y} DHS formation. We performed the PDA treatment on sample DHS1 at N_2 atmosphere for 5

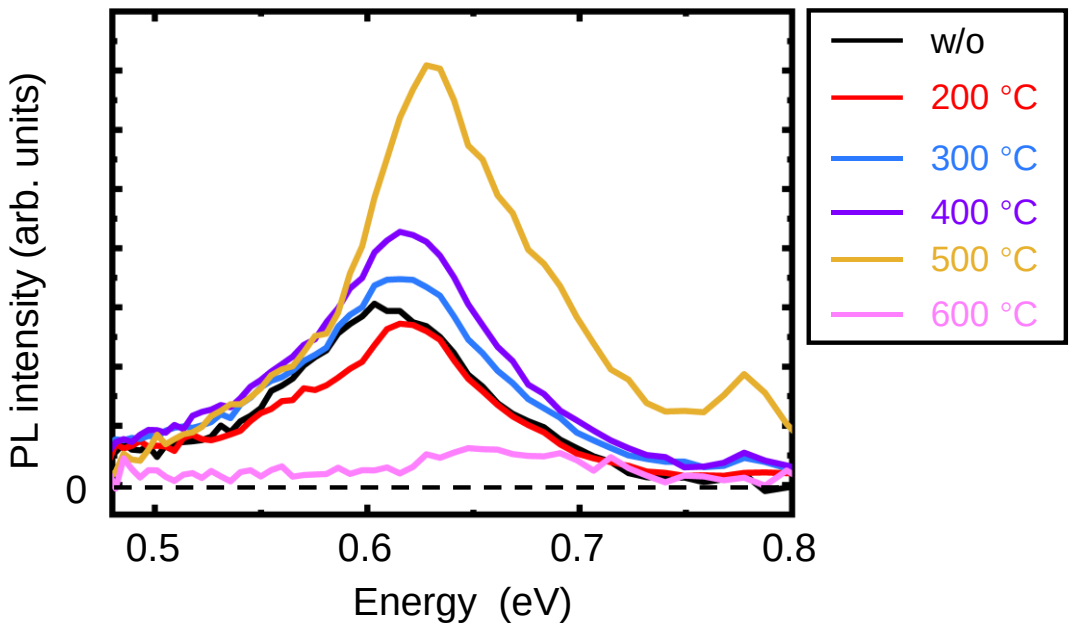

Figure 4.13 PL spectra of sample DHS1 subjected to PDA from w/o to 600 measured at RT. Power of the excitation laser was 1.5 W.

minutes with the temperature of 200-600 °C. **Figure 4.13** shows the PL spectra of the samples after the PDA treatment. For the sample without PDA, a single PL peak located around 0.6 eV is observed. The spectra of the samples subjected to PDA at 200-500 °C also show the single PL peak with different peak intensities where their energy position are slightly shifted to the higher energy side. Despite of the sample that subjected to PDA at 200 °C show a lower peak intensity, the peak intensities of samples after 300-500 °C are totally higher than the as-grown spectrum. It is worth mention that we observed an approximately 2.5 times maximum improvement of the peak intensity for the 500 °C PDA sample compared to that of the as-grown sample. Furthermore, for the spectrum of 600 °C PDA sample, the PL peak is absent, suggesting a decreased PL efficiency for the DHS1 safter 600 °C PDA.

According to the discussion in **section 3.3.3**, the appropriate and over temperature thermal treatment will benefit and reduce the PL efficiency of the $Ge_{1-x}Sn_x$ layer. Since we have concluded that the reduce of the PL efficiency is mainly due to the crystalline degradation, we will also investigate the crystallinity of the sample DHS1 subjected to PDA treatment to discuss the impact of annealing on the emission efficiency of the n^+-$Ge_{1-x}Sn_x$/n-Si_yGe_{1-y} formation. Here, we focus on the XRD measurement results for as-grown DHS1 and those of subjected to PDA at 500 and 600 °C. **Figure 4.14 (a)** shows the measured 004 $Ge_{1-x}Sn_x$ ω-rocking curves. It can be seen that, the as-grown sample and the 500 °C annealed sample have the similar line profile and their broadedning at the tail region are approximatly the same, indicating that there is no significant crystallinity change for n^+-$Ge_{1-x}Sn_x$ layer of the 500 °C annealed sample. However, for the 600 °C annealed sample, its tail region is slightly broadedned, suggesting a crystaline degregation for the n^+-$Ge_{1-x}Sn_x$ layer.

Figures 4.14 (b) and (c) show the XRD-2DRSM results for the DHS1 with 500 and 600 °C PDA treatment. Notably, the Si_yGe_{1-y} and $Ge_{1-x}Sn_x$ diffraction peaks in the two measurement results have the same reciprocal space corditates Q_x to the Ge substrate, indicating the pseudocmorpihc n^+-$Ge_{1-x}Sn_x$/n-Si_yGe_{1-y} formation are maintained after both 500 and 600 °C PDA. Furthermore, the elemental contents of the Si_yGe_{1-y} and $Ge_{1-x}Sn_x$ layers of 500 °C PDA sample were estimated to be 20% Si and 6% Sn, respectively, which is just the same to that of the as-grown DHS1 (see **Figure 4.7 (c)**), suggesting no segregation occurred after the 500 °C PDA. However, for the sample subjected to 600 °C PDA, although its Si content was still estimated the same as 20%, the $Ge_{1-x}Sn_x$ diffraction peak position has shifted on the Q_y axis. The $Ge_{1-x}Sn_x$ diffraction peak was estimated corresponding to the pseudomorphic $Ge_{0.965}Sn_{0.035}$, which suggesting the Sn segregation occurred after the 600 °C PDA. We suggest that the change of the Sn content in the n^+-$Ge_{1-x}Sn_x$ may have disrupted the designed energy band alignment at the n^+-$Ge_{1-x}Sn_x$/n-Si_yGe_{1-y} interface, leads to the weakened carrier confinement. Therefore, the absent of PL peak for the sample subjected to 600 °C PDA should be considered as the combination of the crystalline degradation and Sn segregation in the n^+-$Ge_{1-x}Sn_x$ layer. In total, we consider the n^+-$Ge_{1-x}Sn_x$/n-Si_yGe_{1-y} DHS formation has not only the thermal stability against thermal treatment up to 500 °C, but also the improvement of the PL efficiency can be obtained by the appropriate temperature annealing, which is also around 500 °C. With the understanding of this, we believe the better optoelectronic property of the n^+-$Ge_{1-x}Sn_x$ based heterostructures (DHS, MQW, etc) can also be expected by the favorable thermal treatment.

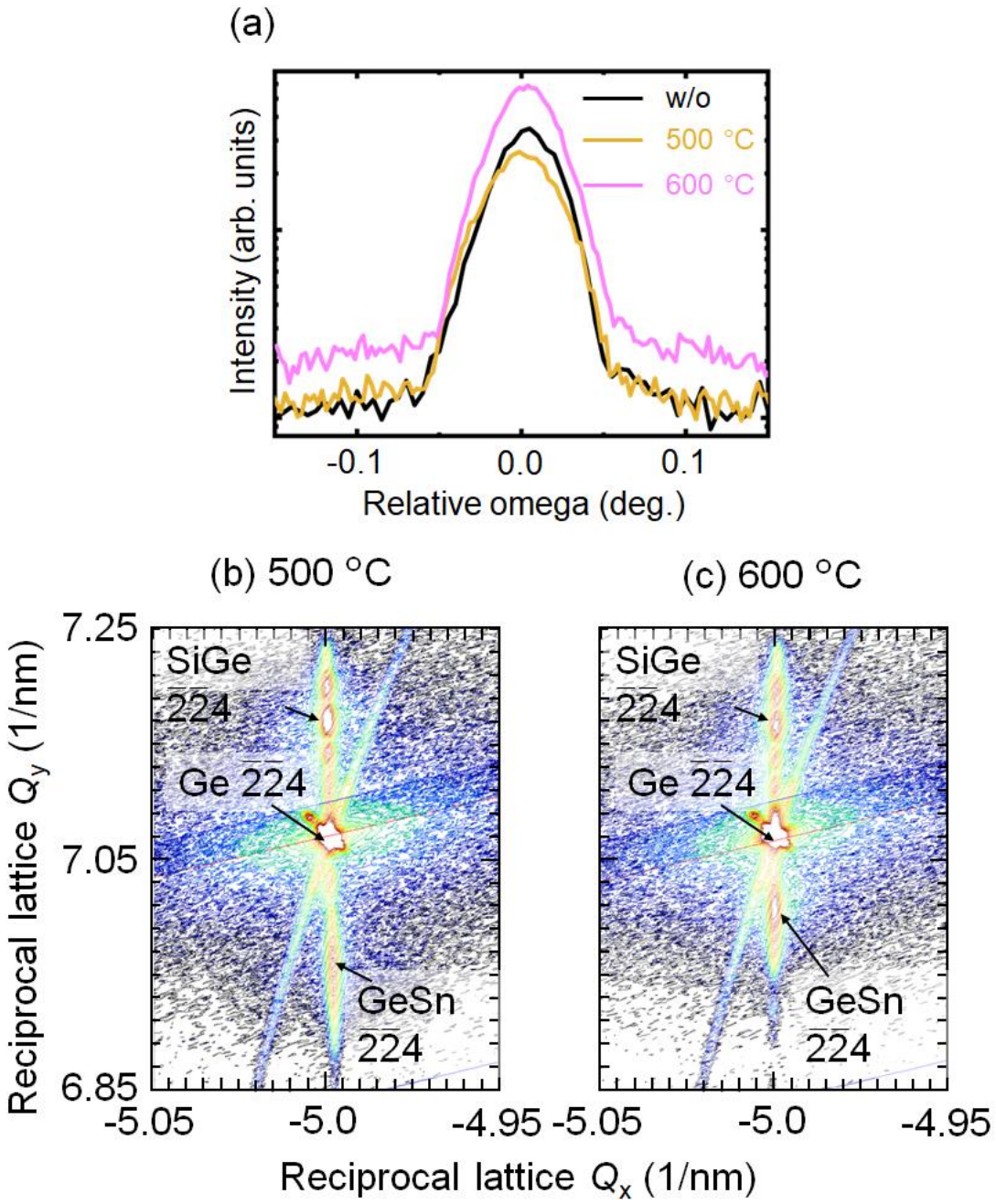

Figure 4.14 (a) ω-rocking curves around the 004 $Ge_{1-x}Sn_x$ for the DHS1 witouth PDA and subjected to 500 and 600 °C PDA; XRD-2DRSM measurement result for the DHS1 sample subjected to (b) 500 and (c) 600°C PDA.

4.4 Summary

We have investigated PL properties of the heavily the Sb doped n^+-$Ge_{0.935}Sn_{0.065}$ epitaxial layers pseudomorphically grown on the *p*-Ge substrate. It is known that the 80-nm-thick n^+-$Ge_{0.935}Sn_{0.065}$ layer with a carrier concentration over 10^{20} cm^{-3} can provide both superior crystallinity and high PL efficiency. However, the PL intensity of the 15-nm-thick n^+-$Ge_{0.935}Sn_{0.065}$ layer is decreased and absent compared to the one with 80 nm thickness. The discussion on the n^+-$Ge_{1-x}Sn_x$/*p*-Ge interface concluded that the increase of valence band offset ΔE_V is essential to establish the sufficient carrier confinement for the thin n^+-$Ge_{1-x}Sn_x$ layer. From the perspective of increasing ΔE_V, we demonstrated the formation of the n^+-$Ge_{1-x}Sn_x$/*n*-Si_yGe_{1-y} SHS and DHS on the *p*-Ge substrate with superior crystallinity and steep uniform interfaces. Additionally, we discussed the PL properties of the SHS and DHS samples in terms of the valence band offset ΔE_V and surface recombination mechanism. We found that the DHS samples with the sufficiently large ΔE_V and the surface passivation effect exhibited PL intensities comparable to that of the 80-nm-thick n^+-$Ge_{0.94}Sn_{0.06}$ layer with a pseudo-direct bandgap transition mechanism. Thus, the ΔE_V control as well as the suppression of the surface recombination by DHS formation is important to improve the emission efficiency of the think n^+-$Ge_{1-x}Sn_x$ layer.

We also investigated the impact of PDA treatment on the n^+-$Ge_{1-x}Sn_x$/*n*-Si_yGe_{1-y} DHS formation and found that appropriate annealing temperature around 500 °C could greatly improve the PL efficiency of the n^+-$Ge_{1-x}Sn_x$/*n*-Si_yGe_{1-y} DHS, and the over temperature annealing at 600 °C will cause the crystalline degradation and Sn segregation in the n^+-$Ge_{1-x}Sn_x$ layer, which leads to the disruption of the energy band alignment and cause the absent of the PL peak.

References

1) S. Wirths, R. Geiger, N. von den Driesch, G. Mussler, T. Stoica, S. Mantl, Z. Ikonic, M. Luysberg, S. Chiussi, J. M. Hartmann, H. Sigg, J. Faist, D. Buca and D. Grützmacher, Nature Photon **9** (2), 88 (2015).

2) P. C. Grant, J. Margetis, Y. Zhou, W. Dou, G. Abernathy, A. Kuchuk, W. Du, B. Li, J. Tolle, J. Liu, G. Sun, R. A. Soref, M. Mortazavi and S.-Q. Yu, AIP Advances **8** (2), 025104 (2018).

3) D. Stange, S. Wirths, R. Geiger, C. Schulte-Braucks, B. Marzban, N. von den Driesch, G. Mussler, T. Zabel, T. Stoica, J.-M. Hartmann, S. Mantl, Z. Ikonic, D. Grützmacher, H. Sigg, J. Witzens and D. Buca, ACS Photonics **3** (7), 1279 (2016).

4) M. Fukuda, D. Rainko, M. Sakashita, M. Kurosawa, D. Buca, O. Nakatsuka and S. Zaima, Jpn. J. Appl. Phys. **58** (SI), SIIB23 (2019).

5) 福田雅大, 博士論文, "GeSn/GeSiSn ヘテロ構造の形成および光電特性の制御に関する研究", 名古屋大学, (2020).

6) M. Schmid, M. Oehme, M. Gollhofer, R. Körner, M. Kaschel, E. Kasper and J. Schulze, Thin Solid Films **557**, 351 (2014).

7) R. E. Camacho-Aguilera, Y. Cai, N. Patel, J. T. Bessette, M. Romagnoli, L. C. Kimerling and J. Michel, Opt. Express, OE **20** (10), 11316 (2012).

8) J. Jeon, T. Asano, Y. Shimura, W. Takeuchi, M. Kurosawa, M. Sakashita, O. Nakatsuka and S. Zaima, Jpn. J. Appl. Phys. **55** (4S), 04EB13 (2016).

9) S. Brotzmann and H. Bracht, J. Appl. Phys. **103** (3), 033508 (2008).

10) X. Sun, J. Liu, L. Kimerling and J. Michel, ECS Trans. **16** (10), 881 (2008).

11) A. Pillukat, K. Karsten and P. Ehrhart, Phys. Rev. B **53** (12), 7823 (1996).

12) A. A. Tonkikh and P. Werner, physica status solidi (b) **250** (9), 1795 (2013).

13) S. Zhang, M. Fukuda, J. Jeon, M. Sakashita, S. Shibayama and O. Nakatsuka, Jpn. J. Appl. Phys. **61** (SA), SA1004 (2021).

14) P. Van Mieghem, Rev. Mod. Phys. **64** (3), 755 (1992).

15) A. Mosleh, S. A. Ghetmiri, B. R. Conley, M. Hawkridge, M. Benamara, A. Nazzal, J. Tolle, S.-Q. Yu and H. A. Naseem, Journal of Elec Materi **43** (4), 938 (2014).

16) R. Ranjan and M. K. Das, Opt Quant Electron **48** (3), 201 (2016).

17) G. Sun, R. A. Soref and H. H. Cheng, Opt. Express, OE **18** (19), 19957 (2010).

18) G. Chang, S. Chang and S. L. Chuang, IEEE Journal of Quantum Electronics **46** (12), 1813 (2010).

19) C. G. Van de Walle, Phys. Rev. B **39** (3), 1871 (1989).

Chapter 5 Conclusions

5.1 Summary of this study

Nowadays, the limitation of metallic interconnect has already become a bottle neck for developing the high-performance, energy-efficiency Si ULSI structure for the future information society. Introducing optical interconnect to replace metallic interconnect has been considered a promising route to solve this issue. Currently, all group-IV material optical interconnect structure has attracted lots of attentions because of the high affinity on the Si ULSI. Many researchers have conducted studies and achieved progression on the development for the group-IV optical interconnect components such as detector, waveguide, and modulator. For the most important component, the light source, $Ge_{1-x}Sn_x$ has been proposed as the most competitive candidate.

To realize the RT operation of the $Ge_{1-x}Sn_x$ light source, the appropriate heterostructure as well as the direct transition for the $Ge_{1-x}Sn_x$ active layer is essential. Recent reports have revealed that the energy band alignment tunable $Ge_{1-x}Sn_x/Si_yGe_{1-x-y}Sn_x$ heterostructure and the multi quantum well formation are both sufficient to increase the light emission efficiency. In this study, we aim to expand the knowledge of the $Ge_{1-x}Sn_x/Si_yGe_{1-x-y}Sn_x$ heterostructures and challenged the $Ge_{1-x}Sn_x/Si_yGe_{1-x-y}Sn_x$ MQW formation by the non-equilibrium MBE growth method that are not well reported. We also investigated the formation and luminescence mechanism of the alternative direct transition of heavy doped $Ge_{1-x}Sn_x$ layer based heterostructures. The results and progressions of this study will be summarized in the following part.

5.1.1 Formation and luminescence properties of $Ge_{1-x}Sn_x$/high-Si-content-$Si_yGe_{1-x-y}Sn_x$ double-quantum wells

We realized the $Ge_{1-x}Sn_x/Si_yGe_{1-x-y}Sn_x$ SQW and DQW structures over 20 % Si content using the non-equilibrium MBE growth method. We firstly investigated the impact of the growth temperatures on the crystalline and PL efficiency of the $Ge_{1-x}Sn_x/Si_yGe_{1-x-y}Sn_x$ SQW and DQW formation. It is found that lowering the growth temperature of the $Si_yGe_{1-x-y}Sn_x$ layer and the $Ge_{1-x}Sn_x$ layer down to 100 °C is beneficial for achieving the superior crystallinity and high PL efficiency at RT, which is mainly contributed by the suppression of Sn atom segregation and the formation of sufficient energy band offset by high-Si-content incorporation.

Considering the practical ULSI manufacture process where numbers of thermal treatment process are involved, the impact of annealing on $Ge_{1-x}Sn_x/Si_yGe_{1-x-y}Sn_x$ SQW and DQW formation and their thermal stability need to be investigated to provide more insight for future application. We also investigated the PDA treatment effect on the crystalline and PL properties of the prepared $Ge_{1-x}Sn_x/Si_yGe_{1-x-y}Sn_x$ SQW and DQW samples. It is found that appropriate annealing condition could benefit the PL performance of both SQW and DQW samples thanks to the crystalline improvement. And the $Ge_{1-x}Sn_x/Si_yGe_{1-x-y}Sn_x$ DQW grown at 100 °C can sustain its crystal structure and PL efficiency up to 350 °C.

This study result has demonstrated a path to achieve high-Si-content $Ge_{1-x}Sn_x/Si_yGe_{1-x-y}Sn_x$ multi quantum well formation using MBE technique and provided an insight to improve their light emission performance by preferable thermal treatment condition.

5.1.2 Formation and PL properties of pseudo-direct transition of heavily Sb doped n^+-$Ge_{1-x}Sn_x$ and the favorable heterostructure

In this part, we investigated the formation and PL properties of heavily Sb doped n^+-$Ge_{1-x}Sn_x$ layer grown by MBE method. The high PL peak intensity has been observed for the 80-nm-thick n^+-$Ge_{0.935}Sn_{0.065}$ layer with carrier concentration over 10^{20} cm^{-3}. It is also found that the favorable energy band alignment design is critical for the 15-nm-thick n^+-$Ge_{1-x}Sn_x$ active layer based heterostructure from the perspective of sufficient carrier confinement. Therefore, we proposed the n^+-$Ge_{1-x}Sn_x$/n-Si_yGe_{1-y} SHS and DHS formation from the aspect of increasing valence band offset ΔE_V. As a result of the favorable n^+-$Ge_{1-x}Sn_x$/n-Si_yGe_{1-y} DHS formation, PL efficiency of the 15-nm-thick n^+-$Ge_{1-x}Sn_x$ active layer has been greatly improved thanks to the sufficient carrier confinement and surface passivation effect.

The PDA treatment on the n^+-$Ge_{1-x}Sn_x$/n-Si_yGe_{1-y} DHS has been also performed to investigate the impact of annealing on its crystalline and PL property. The PL efficiency of the n^+-$Ge_{1-x}Sn_x$/n-Si_yGe_{1-y} DHS has been improved to 2.5 times after the 500 °C PDA treatment. This result suggests that even with the heavy doping condition, the n^+-$Ge_{1-x}Sn_x$/n-Si_yGe_{1-y} DHS still have a good thermal stability and the improving of its emission efficiency can be expected by appropriate annealing condition.

5.2 Remaining issues and future tasks

One of the remaining issues in this study is that we have not completely clarified the origin of several PL components of the PL spectra for the analyzed samples. For the $Ge_{1-x}Sn_x$/$Si_yGe_{1-x-y}Sn_x$ double-quantum wells subjected to PDA of temperature over 400 °C, the degradation of PL efficiency and shift of emission wavelength has been observed.

Currently, we have no reliable theory to explain this phenomenon, it is necessary to conduct future study to expand understanding on the mechanism of over-temperature PDA impact on the emission property of the $Ge_{1-x}Sn_x/Si_yGe_{1-x-y}Sn_x$ heterostructures. Furthermore, improve the thermal stability of the $Si_yGe_{1-x-y}Sn_x$ as well as $Ge_{1-x}Sn$ layers is also improved considering the practical ULSI manufacture process contains manly complex thermal treatment processes.

Other one is that we have not study the multi quantum well formation based on the pseudo-direct bandgap n^+-$Ge_{1-x}Sn_x$ layer. We are expecting that further improvement on the optoelectronic property can be achieved by combine these concepts together. And we are looking forward to study the impact of factors on the formation and performance of the multi quantum well structures such as the layer thickness, number of quantum well periods as well as energy band alignment designs.

Acknowledgements

The thesis entitled “Study on formation and optoelectronic property of the group-IV $Ge_{1-x}Sn_x$ based heterostructures” is the author’s research achievements in his Ph. D program in Department of Materials Physics, Graduate School of Engineering, Nagoya University, Japan.

First of all, I would like to express my sincere appreciate to Prof. Osamu Nakatsuka for offering me an excellent chance to study and research the acknowledge of the semiconductors. Prof. Osamu Nakatsuka has provided me many constructive guidance for conducting efficient experimental procedure and helped me to learn more insight on the group-IV semiconductor materials.

I would like to appreciate Prof. Noritaka Usami and Prof. Kenji Shiraishi for providing valuable advice and comments on my PhD dissertation. I also would like to thank Associate Prof. Masashi Kurosawa, Assistant Prof. Shigehisa Shibayama, and Assistant Prof. Mitsuo Sakashita for fruitful discussion and experimental supports.

During my Ph. D. program stage, I have faced many difficult challenges and I would like to give my gratitude to all those people who have helped me to face the challenges and solve the issues. I appreciate Dr. Masahiro Fukuda, Dr. Jihee Jeon, Mr. Hidetaka Sofue and Mr. Masaya Nakata for helping me to master the MBE technique and material characterization measurements. I would like to thank Dr. Ying Peng, Dr. Huajun Lai, Dr. Takuma Doi, and Mr. An Huang for discussing with me to come up with new research ideas. Also, I appreciate Prof. Inga Fisher and Dr. Jon Benedikt Schlipf for providing me acknowledge to conduct the theory calculation for the energy band alignment of samples.

My gratitude also goes to all the members in Nakatsuka laboratory not only for their help in my daily work but also for communicate and growth together during the four years in the laboratory.

I would like to thank my family members especially my parents for providing me financial and spiritual supports, the Ph. D. life within the Covid-19 pandemic is not easy, without their support I cannot complete my study in time.

Finally, I want to memorize my grandfather who passed away in the last year, as his proud grandson, I've always regretted for not being able to attend his funeral. But I will remember his expecting on me and be a man of honor in my future days.

Shiyu Zhang

December 17, 2022

Publication lists

Journal papers

1) **Shiyu Zhang**, Masahiro Fukuda, Jihee Jeon, Mitsuo Sakashita, Shigehisa Shibayama, and Osamu Nakatsuka "Photoluminescence properties of heavily Sb doped $Ge_{1-x}Sn_x$ and heterostructure design favorable for n^+-$Ge_{1-x}Sn_x$ active layer", Jpn. J. Appl. Phys. **61**, SA1004 (2022).
2) **Shiyu Zhang,** Shigehisa Shibayama and Osamu Nakatsuka "Crystalline and optoelectronic properties of $Ge_{1-x}Sn_x$/high-Si-content-$Si_yGe_{1-x-y}Sn_x$ double-quantum wells grown with low-temperature molecular beam epitaxy", Semicond. Sci. Technol. **38**, 015018 (2023).

International conferences

1) **Shiyu Zhang**, Masahiro Fukuda, Shigehisa Shibayama, and Osamu Nakatsuka "Heterostructure design favorable for n^+-$Ge_{1-x}Sn_x$ pseudo-direct transition layer for optoelectronic application", 13th International Symposium on Advanced Plasma Science and its Applications for Nitrides and Nanomaterials / 14th International Conference on Plasma-Nano Technology & Science, (ISPlasma2021/IC-PLANTS2021), Virtual symposium, March 2021, Japan.
2) **Shiyu Zhang**, and Osamu Nakatsuka "Optoelectronic properties of heterostructures based on pseudo-direct-bandgap transition n^+-$Ge_{1-x}Sn_x$ active layer" ,The 2nd International Workshop on Advanced Nanomaterials for Future Electron Devices 2021 (IWAN2021), ALL-VIRTUAL conference, September 2021, Japan.

3) **Shiyu Zhang**, Mitsuo Sakashita, Shigehisa Shibayama, and Osamu Nakatsuka "Optoelectronic properties of pseudo-direct transition n^+-GeSn and heterostructures composed of n^+-GeSn and n-SiGe thin layers", International Conference on Materials and Systems for Sustainability 2021 (ICMaSS2021), Online, November 2021, Japan
4) **Shiyu Zhang**, Shigehisa Shibayama, and Osamu Nakatsuka, "Formation of non-equilibrium $Ge_{1-x}Sn_x/Si_xGe_{1-x-y}Sn_y$ double-quantum wells and its photoluminescence property", 14th International Symposium on Advanced Plasma Science and its Applications for Nitrides and Nanomaterials / 15th International Conference on Plasma-Nano Technology & Science, (ISPlasma2022/IC-PLANTS2022), Online, March 2022, Japan.

Domestic conferences

1) **Shiyu Zhang**, Shigehisa Shibayama and Osamu Nakatsuka "Formation of $Ge_{1-x}Sn_x/Si_xGe_{1-x-y}Sn_y$ double-quantum wells structure and its photoluminescence mechanism", 第 69 回応用物理学会春季学術講演会, 26a-E301-7, Online, March 2022, Japan.

Awards

1) **Shiyu Zhang**, Masahiro Fukuda, Shigehisa Shibayama, and Osamu Nakatsuka, The Best Oral Presentation Awards of 13th International Symposium on Advanced Plasma Science and its Applications for Nitrides and Nanomaterials / 14th International Conference on Plasma-Nano Technology & Science, (ISPlasma2021/IC-PLANTS2021), March 2021.